12-2010

Energetics and Kinetics of Dislocation Initiation in the Stressed Volume at Small Scales

Tianlei Li
University of Tennessee at Knoxville, tianleilee@gmail.com

To the Graduate Council:

I am submitting herewith a dissertation written by Tianlei Li entitled "Energetics and Kinetics of Dislocation Initiation in the Stressed Volume at Small Scales." I have examined the final electronic copy of this dissertation for form and content and recommend that it be accepted in partial fulfillment of the requirements for the degree of Doctor of Philosophy, with a major in Materials Science and Engineering.

Yanfei Gao, Major Professor

We have read this dissertation and recommend its acceptance:

Easo P. George, George M. Pharr, Hongbin Bei, Xiaopeng Zhao

Accepted for the Council:
Carolyn R. Hodges

Vice Provost and Dean of the Graduate School

(Original signatures are on file with official student records.)

To the Graduate Council:

I am submitting herewith a dissertation written by Tianlei Li entitled “Energetics and Kinetics of Dislocation Initiation in the Stressed Volume at Small Scales”. I have examined the final electronic copy of this dissertation for form and content and recommend that it be accepted in partial fulfillment of the requirements for the degree of Doctor of Philosophy, with a major in Materials Science and Engineering.

Yanfei Gao
Major Professor

We have read this dissertation and recommend its acceptance:

George M. Pharr

Easo P. George

Hongbin Bei

Xiaopeng Zhao

Accepted for the Council:

Carolyn R. Hodges
Vice Provost and Dean of the Graduate School

(Original signatures are on file with official student records.)

Energetics and Kinetics of Dislocation Initiation in the Stressed Volume at Small Scales

A Thesis Presented for the

Doctor of Philosophy Degree

The University of Tennessee, Knoxville

Tianlei Li

December 2010

Acknowledgements

This dissertation would not have been possible without the help and support of many kind people around me. Foremost among them is my adviser, Professor Yanfei Gao, who has given me invaluable wisdom and constructive advices, guided me throughout my Ph.D. study, and devoted countless time and effort that leads me to the success of my doctoral research fruitfully and timely. He is the best adviser I could ever ask for.

I would like to give my thanks to my committee members, Drs. George M. Pharr, Easo P. George, Hongbin Bei, and Xiaopeng Zhao. Profs. George M. Pharr and Easo P. George partly supported my research and shared their profound knowledge and visions with me. Dr. Hongbin Bei provided invaluable experimental data on which this thesis is based. I have learned a lot from his carefulness and my fruitful discussions with him. I am also indebted to Prof. James R. Morris for the important help on model development in the last part of this thesis work.

My friends and colleagues have been constantly supported me and believed in me, including Jinhaeng Lee, Jianyong Meng, Lili Zheng, Shunfang Li, Chi-Hua Yu, Lin Li, Weidong Li, Jun Xu, Caijun Su, Weichao Ye, Ning Wang, Mankun Cai, Haitao Xu, and Kaiyuan Zhang.

Finally, I give my great appreciation to Ms. Sha Ouyang and my parents. No words can express my gratitude to them. This dissertation is dedicated to them.

This work is partly supported by the Materials Sciences and Engineering Division, Office of Basic Sciences, U.S. Department of Energy, and by the Joint Institute for Advanced Materials at the University of Tennessee.

ABSTRACT

Instrumented nanoindentation techniques have been widely used in characterizing mechanical behavior of materials in small length scales. For defect-free single crystals under nanoindentation, the onset of elastic-plastic transition is often shown by a sudden displacement burst in the measured load-displacement curve. It is believed to result from the homogeneous dislocation nucleation because the maximum shear stress at the pop-in load approaches the theoretical strength of the material and because statistical measurements agree with a thermally activated process of homogeneous dislocation nucleation. For single crystals with defects, the pop-in is believed to result from the sudden motion of pre-existing dislocations or heterogeneous dislocation nucleation. If the sample is prestrained before nanoindentation tests, a monotonic decrease of the measured pop-in load with respect to the increase of prestrain on Ni and Mo single crystals is observed. A similar trend is also observed that the pop-in load will gradually decrease if the size of indenter tip radius increases.

This dissertation presents a systematic modeling endeavor of energetics and kinetics of defect initiation in the stressed volume at small scales. For homogeneous dislocation nucleation, an indentation Schmid factor is determined as the ratio of maximum resolved shear stress to the maximum contact pressure. The orientation-depended nanoindentation pop-in loads are predicted based on the indentation Schmid factor, theoretical strength of the material, indenter radius, and the effective indentation modulus. A good agreement has been reached when comparing the experimental data of nanoindentation tests on NiAl, Mo, and Ni, with different loading orientations to theoretical predictions. Statistical measurements generally confirm the thermal activation model of homogeneous dislocation nucleation, because the extracted dependence of activation energy on resolved shear stress is almost unique for all the indentation directions. For pop-in due to pre-existing defects, the pop-in load is predicted to be dependent on the defect density and the critical strength for heterogeneous dislocation nucleation. The cumulative probability of pop-in loads contains convoluted information from the homogenous dislocation nucleation, which is sensitive to temperature and loading rate, and heterogeneous dislocation nucleation due to the unstable change of existing defect network, which is sensitive to the initial defect distribution.

TABLE OF CONTENTS

LIST OF TABLES

LIST OF FIGURES

CHAPTER I

Introduction

The instrumented indentation, also known as depth-sensing indentation or nanoindentation, is increasingly being used to probe the mechanical response of materials. In contrast to the traditional hardness testing methods, instrumented indentation systems allow the force, P, and the displacement, h, to be controlled and/or measured simultaneously and continuously over a complete loading cycle. The extremely small force and displacement resolutions, often as low as ≈1 μN and ≈0.2 nm, respectively, or lower for some systems, are combined with very large ranges of applied forces and displacements (tens of μN to hundreds of mN or larger in force and tens of nm to tens of μm or larger in displacement) to allow a single instrument to be used to characterize nearly all types of material systems. In fact, the instrumented nanoindentation technique has become a key component of materials research at small scales with applications in a wide variety of disciplines [1-3]. Methodologies have been established on how to extract material properties such as modulus and hardness from the measured load and displacement curves.

In addition to the characterization of material properties, there has been increasing research activities by using instrumented indentation to probe microscopic deformation processes such as defect nucleation. For example, nanoindentation of metallic materials has shown that defect nucleation could possibly be associated with the onset of the indenter tip suddenly jumping into the specimen with negligible load increase (or denoted as "pop-in"), which leads to a displacement discontinuity on the otherwise continuous load-displacement curve [4-17]. While the pop-in event may be associated with fracture of surface oxide layer for some materials [18], it is believed that for a defect-free crystalline material, the first displacement burst is a result of homogeneous dislocation nucleation underneath the indenter [6, 7,9 -17,19-21]. Moreover, if there is existing defect underneath the indenter, pop-in could also be observed as a result of heterogeneous dislocation event (such as a sudden instability of existing defect network) in single crystals. Defect nucleation due to materials geometric effect is also important. For example, in nano-electronic devices, stress concentrations near sharp geometric features such as edges and corners may lead to the nucleation of dislocations, which can act as electrical leakage paths and eventually lead to failure of the devices [22, 23, 24]. The development of immortal, strained nano-electronics requires knowledge of the

defect nucleation process and its dependence on the layout structure, materials processing, and surface treatment, among many others.

This thesis aims to present a systematic study of energetics and kinetics of defect initiation in the stressed volume at small scales. The primary interests will be placed on the nanoindentation pop-in behavior in single crystals due to homogeneous or heterogeneous dislocation nucleation activities.

In Chapter II, the stress fields of elastically anisotropic film-on-substrate systems under spherical indentation are derived from the superposition of the Green's function. The surface-displacement Green's function for elastically anisotropic film-on-substrate system is derived in closed-form by using the Stroh formalism and the two-dimensional Fourier transform. When the film and substrate has the same materials constants, the solution degenerates to the case of single crystals under spherical indentation. This solution allows us to calculate the indentation Schmid factor which is defined as the ratio of the maximum resolved shear stress of all possible slip systems to the maximum contact pressure. This result will be used in predicting nanoindentation pop-in loads in Chapter V. The predicted dependence of the effective modulus on the ratio of film thickness to contact radius agrees well with detailed finite element simulations. Implications in evaluating film modulus by nanoindentation technique are also discussed.

In Chapter III, we describe how to calculate the activation energy for homogeneous or heterogeneous dislocation nucleation with finite element method by adopting the Rice-Peierls concept of dislocation. This method is realized by a dissipative cohesive interface model which treats the dislocation core as a continuous, inhomogeneous lattice slip field. We also apply this method to model trailing/twinning partial dislocation nucleation after a leading partial dislocation is nucleated from a crack tip.

In Chapter IV, using the tool in Chapter III, we investigate the dislocation nucleation behavior due to materials geometric effect. Dislocation loops may be nucleated from sharp geometric features. As a representative example, we calculate the critical external stress for dislocation nucleation from the edges/corners of a rectangular Si_3N_4 pad on a Si substrate as a function of geometric parameters such as the length-to-height ratio and the three-dimensional shape of the pad. The shapes of the nucleated dislocation loops are also simulated.

In Chapter V, assuming that a dislocation nucleates when the maximum resolved shear stress reaches the theoretical strength, the pop-in load is predicted to be a function of indenter radius, effective indentation modulus, indentation Schmid factor, crystallographic orientation of the specimen, and the theoretical strength. Comparisons to experimental measurements on

NiAl single crystals will test the validity of the above relationship and fit the theoretical strength of the specimen. The homogeneous dislocation nucleation process is also a stress-assisted, thermally activated process. When the applied load is less than but close to the critical load for homogeneous dislocation nucleation, the thermal energy can activate dislocation to nucleate. The statistical measurements generally confirm our thermal activation model of homogeneous dislocation nucleation. That is, for defect-free single crystals, the extracted dependence of activation energy on resolved shear stress is almost the same for all the indentation directions.

In Chapter VI, the cumulative probability of pop-in loads contains convoluted information from the homogenous dislocation nucleation and possible heterogeneous dislocation nucleation due to the unstable change of existing defect network. A unified model of the homogeneous and heterogeneous dislocation nucleation behavior has been developed and successfully explained several interesting experiments, including (1) pop-in tests on NiAl single crystals with surface normal close to <001>, (2) indenter-radius effects on Mo <001> single crystals, and (3) pre-strain effects on Mo <001> single crystals. The transition from thermally activated dislocation nucleation process to spatial-probability-governed behavior has been identified.

Future work and perspectives will be discussed in Chapter VII.

CHAPTER II

Elastic Contact Analysis of Anisotropic Solids

2.1 Introduction

Many experimental techniques for measuring thin film mechanical properties are based on bending, stretching, or other simple mechanical means for testing free-standing or constrained films [25]. Tedious sample preparation procedures are clearly a disadvantage that hinders wide-spread engineering applications of these methods. The instrumented nanoindentation technique, based on the information of load (denoted as P)-displacement (denoted as h) curves, has become a key component of materials research at small scales with applications in a wide variety of disciplines [1-3, 26]. In this method, an indenter with known geometry is pushed into the surface of a material under a set of prescribed loading conditions. The resulting displacement of the indenter into the material is recorded, and the load and displacement data are analyzed via analytical and/or numerical models to extract mechanical properties of the indented specimen such as modulus and hardness from the measured P~h curves. Besides the measurement of the hardness and modulus, the P~h curves can be used to examine the onset of elastic-plastic transition in various crystalline and amorphous materials [4-17]. The onset of plasticity is often associated with a displacement discontinuity on the otherwise continuous load-displacement curve, or denoted as "pop-in", as the indenter tip suddenly jumps into the specimen with negligible load increase. As will be discussed in Chapter V, for a defect-free crystalline material, the first displacement burst is a result of homogeneous dislocation nucleation underneath the indenter. Most of previous theoretical studies assume that the homogeneous dislocation nucleation occurs when the resolved shear stress reaches the theoretical strength, which is similar to the Schmid law that describes the plastic flow in single crystals.

Moreover, the nanoindentation technique has difficulties of uniquely determining material properties [27,28] and decoupling the film deformation behavior from substrate effects [29-34]. It is empirically recommended that the indentation depth should be smaller than 10% of the film thickness in order to minimize the influence of substrate deformation. However, many film materials used in micro- and nano-electronics are so thin that 10% of the film thickness cannot be accurately probed. The indentation behavior at depths comparable to

the film thickness contains a great deal of information that should not be intentionally excluded.

In this Chapter, we first derive the stress fields in an anisotropic film-on-substrate system under spherical indentation. And then, by degenerating this stress fields to an anisotropic solid under spherical indentation, we calculate the indentation Schmid factor which is defined as the ratio of the maximum resolved shear stress of all possible slip systems to the maximum contact pressure. Assuming that dislocation nucleates when the maximum resolved shear stress reaches the theoretical strength, the pop-in load will be predicted in Chapter V to be a function of indenter radius, effective indentation modulus, indentation Schmid factor, crystallographic orientation, and the theoretical strength. A central relationship in the nanoindentation technique is the proportionality between the elastic contact stiffness and an effective indentation modulus. Extensive studies have been conducted for homogeneous half-spaces [35-38] and elastically isotropic film-on-substrate systems [39,40]. This work extends this line of research to the response of an elastically anisotropic film-on-substrate system indented by an arbitrarily-shaped rigid indenter. From stress fields of anisotropic film-on-substrate system, we derive a closed-form representation of the contact stiffness which involves the evaluation of a triple integral. The validity of these assumptions is theoretically discussed by using the cumulative superposition method [41], and the predicted dependency of the effective modulus on the ratio of film thickness to contact radius is numerically compared to detailed finite element simulations. Finally, we discuss the important roles played by the indentation pileup/sink-in, contact shape, friction, and modulus mismatch in the relationship between the contact stiffness and effective elastic modulus.

2.2 Closed-Form Green's Tensor for Anisotropic Multilayered Half-Space

For a multilayered half-space, the indentation response from an assumed pressure distribution can be conveniently evaluated from the surface-displacement Green's function. As shown in Fig. 2.1, we consider a circular contact on a layered substrate with the elastic constants being c_{ijkl}^{I} and c_{ijkl}^{II} for film and substrate, respectively.

The Stroh formalism [42-47] and two-dimensional Fourier transform are combined to solve the stress/strain fields in a multilayed half-space subjected to arbitrary surface tractions. The elastic field is a superposition of many Fourier components, each being a plane field in the plane spanned by $h_\alpha x_\alpha = h_1 x_1 + h_2 x_2$ and x_3, where (h_1, h_2) is a unit vector in the (x_1, x_2)

plane (Fig. 2.1). Greek indices run from 1 to 2. Summation convention on repeated subscripts is implied. Because of the homogeneous nature of the governing equations, for each Fourier component, we look for a general solution of the displacement u_l of the form $u_l = A_l f(z)$, where $z = h_1 x_1 + h_2 x_2 + p x_3$, p is a scalar, A_l is a vector and f is a one-variable function to be determined from boundary conditions. Latin indices run from 1 to 3. For convenience, we write $p = h_3$ and substitute this general solution into the governing equations $c_{ijkl} u_{k,lj} = 0$. Eliminating the factor $d^2 f / dz^2$ leads to a generalized algebraic eigenvalue problem, $c_{ijkl} h_j h_m A_l = 0$, with p being the eigenvalue and A_l the eigenvector. The six roots of the sixth-order polynomial, $\det(c_{ijkl} h_j h_m) = 0$, form three pairs of complex conjugates. The three roots with positive imaginary parts are denoted by p_a, a=1,2,3, and thus the corresponding three complex variables are $z_a = h_1 x_1 + h_2 x_2 + p_a x_3$ and the corresponding eigenvectors A_{ka}. The displacement field is a linear superposition of three arbitrary analytical functions $f_1(z_1)$, $f_2(z_2)$, and $f_3(z_3)$:

$$u_l = \sum_a A_{la} f_a(z_a) + \sum_a \overline{A}_{la} \overline{f}_a(\overline{z}_a), \tag{2.1}$$

where a bar on the top of a quantity denotes its complex-conjugate. The traction on the plane normal to the x_3 axis, $\mathbf{t} = (\sigma_{13}, \sigma_{23}, \sigma_{33})^{\mathrm{T}}$, is given by

$$\sigma_{i3} = \sum_a L_{ia} f_a'(z_a) + \sum_a \overline{L}_{ia} \overline{f}_a'(\overline{z}_a), \tag{2.2}$$

where L_{ia} in expanded form are given by

$$\begin{pmatrix} L_{1a} \\ L_{2a} \\ L_{3a} \end{pmatrix} = \begin{pmatrix} c_{51}h_1 + c_{56}h_2 + c_{55}p_a & c_{56}h_1 + c_{52}h_2 + c_{54}p_a & c_{55}h_1 + c_{54}h_2 + c_{53}p_a \\ c_{41}h_1 + c_{46}h_2 + c_{45}p_a & c_{46}h_1 + c_{42}h_2 + c_{44}p_a & c_{45}h_1 + c_{44}h_2 + c_{43}p_a \\ c_{31}h_1 + c_{36}h_2 + c_{35}p_a & c_{36}h_1 + c_{32}h_2 + c_{34}p_a & c_{35}h_1 + c_{34}h_2 + c_{33}p_a \end{pmatrix} \begin{pmatrix} A_{1a} \\ A_{2a} \\ A_{3a} \end{pmatrix}.$$

Summation convention over underscored repeated indices is not implied. The Stroh matrix is defined by $\mathbf{B} = i\mathbf{A}\mathbf{L}^{-1}$, which is a positive-definite Hermitian. Isotropic elasticity is a degenerate case, since the sixth-order polynomial, $\det(c_{ijkl} h_j h_m) = 0$, will have three pairs of repeat roots, $\pm i$. In this case, one can either use the well-established complex-variable method in isotropic elasticity [48-50], or add a small perturbation to the elastic constants so that the eigenvalues will be distinct.

Since the matrices $\mathbf{A}$, $\mathbf{L}$, and $\mathbf{B}$ are determined from c_{ijkl} and h_α, the elastic stress and strain fields in each layer are determined from the corresponding three functions, $f_1(z_1)$, $f_2(z_2)$, and $f_3(z_3)$. By the principle of linear superposition, we only need to find the solution of one Fourier component,

$$\mathbf{t} = \mathbf{a}\exp\left(i\xi_1 x_1 + i\xi_2 x_2\right) + \overline{\mathbf{a}}\exp\left(-i\xi_1 x_1 - i\xi_2 x_2\right). \tag{2.3}$$

Let ζ be a complex variable of the form $\zeta = h_1 x_1 + h_2 x_2 + q x_3$, where q is an arbitrary complex number with a positive imaginary part. Using the analytic continuation technique, the solution in the film is written as

$$\mathbf{L}_{\mathrm{I}}\mathbf{f}_{\mathrm{I}}'(\zeta) = \mathbf{P}\exp\left(-i\xi\zeta\right) + \mathbf{Q}\exp\left(i\xi\zeta\right), \tag{2.4}$$

$$\mathbf{A}_{\mathrm{I}}\mathbf{f}_{\mathrm{I}}(\zeta) = \frac{\mathbf{B}_{\mathrm{I}}\mathbf{P}}{\xi}\exp\left(-i\xi\zeta\right) - \frac{\mathbf{B}_{\mathrm{I}}\mathbf{Q}}{\xi}\exp\left(i\xi\zeta\right), \tag{2.5}$$

where $\mathbf{P}$ and $\mathbf{Q}$ are two unknown vectors to be determined from boundary conditions. After $f_{\mathrm{I}1}(\zeta), f_{\mathrm{I}2}(\zeta), f_{\mathrm{I}3}(\zeta)$ and $f_{\mathrm{I}1}'(\zeta), f_{\mathrm{I}2}'(\zeta), f_{\mathrm{I}3}'(\zeta)$ are obtained, we then replace the variable to $f_{\mathrm{I}1}(z_1), f_{\mathrm{I}2}(z_2), f_{\mathrm{I}3}(z_3)$ and $f_{\mathrm{I}1}'(z_1), f_{\mathrm{I}2}'(z_2), f_{\mathrm{I}3}'(z_3)$. The displacement and traction fields can be evaluated from Eqs. (2.1) and (2.2), giving

$$\mathbf{u}_{\mathrm{I}} = \frac{\overline{\mathbf{B}}_{\mathrm{I}}\overline{\mathbf{T}}_{\mathrm{I}}^{-}\overline{\mathbf{P}} - \mathbf{B}_{\mathrm{I}}\mathbf{T}_{\mathrm{I}}^{+}\mathbf{Q}}{\xi}\exp\left(i\xi_1 x_1 + i\xi_2 x_2\right) + \frac{\mathbf{B}_{\mathrm{I}}\mathbf{T}_{\mathrm{I}}^{-}\mathbf{P} - \overline{\mathbf{B}}_{\mathrm{I}}\overline{\mathbf{T}}_{\mathrm{I}}^{+}\overline{\mathbf{Q}}}{\xi}\exp\left(-i\xi_1 x_1 - i\xi_2 x_2\right), \tag{2.6}$$

$$\mathbf{t}_{\mathrm{I}} = \left(\overline{\mathbf{T}}_{\mathrm{I}}^{-}\overline{\mathbf{P}} + \mathbf{T}_{\mathrm{I}}^{+}\mathbf{Q}\right)\exp\left(i\xi_1 x_1 + i\xi_2 x_2\right) + \left(\mathbf{T}_{\mathrm{I}}^{-}\mathbf{P} + \overline{\mathbf{T}}_{\mathrm{I}}^{+}\overline{\mathbf{Q}}\right)\exp\left(-i\xi_1 x_1 - i\xi_2 x_2\right), \tag{2.7}$$

where the dimensionless matrices $\mathbf{T}_{\mathrm{I}}^{\pm}$ are $T_{\mathrm{I}lj}^{\pm} = \sum_{a=1}^{3} L_{1la} L_{1aj}^{-1} \exp\left(\pm i\xi p_{1a} x_3\right)$. The unknown vectors $\mathbf{P}$ and $\mathbf{Q}$ are obtained from the boundary condition in Eq. (2.3),

$$\mathbf{P} + \overline{\mathbf{Q}} = \overline{\mathbf{a}}, \tag{2.8}$$

and the continuity condition at the film-substrate interface ($x_3 = -d$),

$$\mathbf{B}_{\mathrm{I}}\mathbf{C}_{\mathrm{I}}^{-}\mathbf{P} - \overline{\mathbf{B}}_{\mathrm{I}}\overline{\mathbf{C}}_{\mathrm{I}}^{+}\overline{\mathbf{Q}} = \mathbf{B}_{\mathrm{II}}\left(\mathbf{C}_{\mathrm{I}}^{-}\mathbf{P} + \overline{\mathbf{C}}_{\mathrm{I}}^{-}\overline{\mathbf{Q}}\right). \tag{2.9}$$

where $\mathbf{C}_{\mathrm{I}}^{\pm} = \mathbf{T}_{\mathrm{I}}^{\pm}\big|_{x_3=-d}$. Consequently,

$$\begin{pmatrix}\mathbf{P}\\ \overline{\mathbf{Q}}\end{pmatrix} = \begin{pmatrix}\left[\left(\mathbf{B}_{\mathrm{I}} - \mathbf{B}_{\mathrm{II}}\right)\mathbf{C}_{\mathrm{I}}^{-} + \left(\overline{\mathbf{B}}_{\mathrm{I}} + \mathbf{B}_{\mathrm{II}}\right)\overline{\mathbf{C}}_{\mathrm{I}}^{+}\right]^{-1}\left(\overline{\mathbf{B}}_{\mathrm{I}} + \mathbf{B}_{\mathrm{II}}\right)\overline{\mathbf{C}}_{\mathrm{I}}^{+}\overline{\mathbf{a}}\\ \left\{\mathbf{I} - \left[\left(\mathbf{B}_{\mathrm{I}} - \mathbf{B}_{\mathrm{II}}\right)\mathbf{C}_{\mathrm{I}}^{-} + \left(\overline{\mathbf{B}}_{\mathrm{I}} + \mathbf{B}_{\mathrm{II}}\right)\overline{\mathbf{C}}_{\mathrm{I}}^{+}\right]^{-1}\left(\overline{\mathbf{B}}_{\mathrm{I}} + \mathbf{B}_{\mathrm{II}}\right)\overline{\mathbf{C}}_{\mathrm{I}}^{+}\right\}\overline{\mathbf{a}}\end{pmatrix}. \tag{2.10}$$

The surface-displacement Green's function in the Fourier's space is therefore given by

$$\hat{\mathbf{w}}\left(\xi_1,\xi_2;d\right)=\frac{-\bar{\mathbf{B}}_{\mathrm{I}}+\left(\bar{\mathbf{B}}_{\mathrm{I}}+\mathbf{B}_{\mathrm{I}}\right)\left[(\mathbf{B}_{\mathrm{I}}-\mathbf{B}_{\mathrm{II}})\mathbf{C}_{\mathrm{I}}^{-}+(\bar{\mathbf{B}}_{\mathrm{I}}+\mathbf{B}_{\mathrm{II}})\bar{\mathbf{C}}_{\mathrm{I}}^{+}\right]^{-1}(\bar{\mathbf{B}}_{\mathrm{I}}+\mathbf{B}_{\mathrm{II}})\bar{\mathbf{C}}_{\mathrm{I}}^{+}}{2\pi\xi}. \quad (2.11)$$

We can also define

$$\hat{\mathbf{W}}\left(h_\alpha,\xi d\right)=\xi\hat{\mathbf{w}}\left(\xi_1,\xi_2;d\right). \quad (2.12)$$

If the film and substrate are the same, then Eq. (2.6) degenerates into

$$u_i=\frac{1}{\xi}E_{ij}a_j\exp\left(-i\xi_1x_1-i\xi_2x_2\right), \quad (2.13)$$

where

$$E_{ij}=\sum_{a=1}^{3}iA_{ia}L_{aj}^{-1}\exp\left(-i\xi p_a x_3\right). \quad (2.14)$$

The displacement Green tensor in the Fourier's space is therefore given by

$$\hat{\mathbf{w}}\left(\xi_1,\xi_2,x_3\right)=\frac{1}{2\pi\xi}\mathbf{E}\left(h_1,h_2,\xi x_3\right). \quad (2.15)$$

It can be shown that the surface deflection Green tensor is

$$\hat{\mathbf{w}}\left(\xi_1,\xi_2,x_3=0\right)=\frac{\mathbf{1}}{2\pi\xi}\mathbf{B}\left(h_1,h_2\right). \quad (2.16)$$

2.3 Indentation Schmid Factor for Anisotropic Hertzian Contact

When an elastically anisotropic half-space is under Hertzian contact (i.e., the spherical indenter can be approximated by a paraboloid of revolution), it has been shown that the contact area is elliptical and the contact pressure distribution $p\left(x_1,x_2\right)$ is given by

$$p\left(x_1,x_2\right)=p_0\sqrt{1-\left(x_1/a_1\right)^2-\left(x_2/a_2\right)^2}, \quad (2.17)$$

where p_0 is the maximum contact pressure in the contact area, and a_1 and a_2 are half axes of the ellipse [36,37,51,52]. For typical materials, it has been found that the degree of ellipticity is negligible, so the contact shape can be assumed to be circular. The total load is calculated from integrating Eq. (2.17), giving $P=\frac{2}{3}\pi a^2p_0$. The contact analysis gives

$$p_0=\left(\frac{6PE_r^2}{\pi^3R^2}\right)^{1/3}, \quad (2.18)$$

where the reduced indentation modulus $E_r = \left[\left(1-v_s^2\right)/E_s + \left(1-v_i^2\right)/E_i\right]^{-1}$ for isotropic solids or $E_r = \left[1/E_{eff} + \left(1-v_i^2\right)/E_i\right]^{-1}$ for anisotropic solids. E_s and v_s are the Young's modulus and Poisson's ratio of the isotropic specimen and E_{eff} is the effective indentation modulus of the anisotropic specimen which will be determined later. E_i and v_i are the Young's modulus and Poisson's ratio of the diamond indenter, respectively, i.e., 1141 GPa and 0.07.

The Hertzian stress fields can be determined from the pressure distribution in Eq. (2.17) and the Green tensor. Consider surface tractions on the surface of a half-space:

$$\mathbf{t} = \mathbf{t}_0\sqrt{1-\left(x_1/a_1\right)^2-\left(x_2/a_2\right)^2}\,, \tag{2.19}$$

with $\mathbf{t}_0 = \left(t_{01}, t_{02}, t_{03}\right)^{\mathrm{T}}$, so that the displacement field in the substrate is

$$\mathbf{u}\left(x_1,x_2,x_3\right) = \iint_S \mathbf{w}\left(x_1-x_1', x_2-x_2', x_3\right)\mathbf{t}_0\sqrt{1-\left(x_1'/a_1\right)^2-\left(x_2'/a_2\right)^2}\,dx_1'dx_2'\,, \tag{2.20}$$

where the Green tensor $\mathbf{w}\left(x_1,x_2,x_3\right)$ is given in the previous section.

Substituting Eq. (2.15) into Eq. (2.20) and only considering the normal surface traction, i.e., $\mathbf{t}_0 = \left(0,0,p_0\right)^{\mathrm{T}}$, we get

$$\begin{aligned} u_l &= \frac{p_0}{2\pi}\iint_S \sqrt{1-\left(x_1'^2+x_2'^2\right)/a^2}\,dx_1'dx_2' \iint \frac{1}{2\pi\xi} E_{l3}\left(h_1,h_2,\xi x_3\right) e^{-i\xi_\beta\left(x_\beta-x_\beta'\right)} d\xi_1 d\xi_2 \\ &= \frac{p_0}{2\pi}\sum_{a=1}^{3}\iint_S \sqrt{1-\left(x_1'^2+x_2'^2\right)/a^2}\,dx_1'dx_2' \int_0^{2\pi} f_{la}\left(h_1,h_2\right)d\theta \int_0^{\infty} e^{-i\xi_\beta\left(x_\beta-x_\beta'\right)-i\xi p_a x_3}\,d\xi \\ &= ip_0\sum_{a=1}^{3}\int_0^{2\pi} f_{la}\left(h_1,h_2\right)\left\{\frac{g_a}{2}-\frac{g_a^2-1}{4}\ln\left(\frac{g_a+1}{g_a-1}\right)\right\}d\theta \end{aligned} \tag{2.21}$$

where $g_a = -p_a x_3 - h_1 x_1 - h_2 x_2$. As pointed out by Willis [51], an appropriate domain of definition of $\ln(z)$ in the above is the z-plane cut along the negative real axis. Since g_a always has a positive imaginary part, we get $-\pi \le \arg\left(\frac{g_a+1}{g_a-1}\right) < 0$. In the calculation of stress fields from $\sigma_{ij} = c_{ijkl}u_{k,l}$ with elastic stiffness tensor c_{ijkl}, we need the displacement gradients:

$$\begin{aligned} \frac{\partial u_i}{\partial x_\beta} &= \frac{1}{2\pi}\sum_{a=1}^{3}\int_0^{\pi} h_\beta A_{ia} L_{a3}^{-1}\left\{1-\frac{g_a}{2}\ln\left(\frac{g_a+1}{g_a-1}\right)\right\}d\theta \\ \frac{\partial u_i}{\partial x_3} &= \frac{1}{2\pi}\sum_{a=1}^{3}\int_0^{\pi} p_a A_{ia} L_{a3}^{-1}\left\{1-\frac{g_a}{2}\ln\left(\frac{g_a+1}{g_a-1}\right)\right\}d\theta \end{aligned} \tag{2.22}$$

We have validated the above approach by comparing to the available Hertzian stress fields for elastically isotropic solids. In this case, the eigen-problem in determining p_a becomes degenerated and gives rise to repeated roots. A small perturbation to the elastic constants will add a slight anisotropy to regularize this problem.

The resolved shear stress, $\tau_{rss}^{(\alpha)}$, on the α-th slip system of the substrate is computed from the indentation stress fields, σ_{ij}, by

$$\tau_{rss}^{(\alpha)} = \sigma_{ij} s_i^{*(\alpha)} m_j^{*(\alpha)}, \tag{2.23}$$

where s_i^* and m_i^* are the slip direction and slip normal, respectively. Thus we define the indentation Schmid factor, *S*, under Hertzian contact as the ratio of the maximum resolved shear stress to the maximum contact pressure, namely,

$$S = \frac{\tau_{rss}^{\max}}{p_0} = \frac{1}{p_0} \max_{(\alpha)} \left\{ \tau_{rss}^{(\alpha)} \left(x_i \right) \right\}. \tag{2.24}$$

As long as the stress fields, $\sigma_{ij}\left(x_k\right)$, are known, we can determine the slip system and the location that reach $\tau_{rss}^{\max}$.

In calculating the indentation Schmid factor from the contact stress fields and Eq. (2.24), we use the Nelder-Mead simplex algorithm [53] to search for the maximum of the resolved shear stress. Since the stress fields vary slowly near their extrema, we found that a variation of $\pm 0.05a$ near the maximum location will not lead to noticeable change of the resolved shear stress. Figure 2.2 plots the S contours for Ni (FCC structure) and NiAl (B2 structure) single crystals. Elastic constants used are c_{11}=244 GPa, c_{12}=158 GPa, and c_{44}=102 GPa for Ni, and c_{11}=199 GPa, c_{12}=137 GPa, and c_{44}=116 GPa for NiAl. We confirm that if the indentation direction is located inside the standard $[001]$ triangle in the inverse pole figure, the maximum resolved shear stress is always reached at the primary slip system, being $(1\bar{1}1)[011]$ for Ni and $(110)[001]$ for NiAl. If the indentation direction is located on the vertices or boundaries of the standard $[001]$ triangle, at least two slip systems will have the same indentation Schmid factor. Similar to the uniaxial test for Ni, if the indentation direction is on the $[001]$–$[111]$ boundary, we get the $(\bar{1}11)[101]$ conjugate slip system; on the $[001]$–$[101]$ boundary, we get the $(111)[0\bar{1}1]$ critical slip system; and on $[101]$–$[111]$ boundary,

we get the $(1\bar{1}1)[110]$ coplanar slip system. The three vertices at $[101]$, $[111]$, and $[001]$ have 4, 6 and 8 active slip systems, respectively.

As shown in Fig. 2.2, contours of the indentation Schmid factor form a set of concentric circles, as opposed to ellipses for uniaxial tests, in the inverse pole figure. Within calculation accuracy, the location where the indentation Schmid factor reaches maximum on the <001> standard triangle is the same as that where the uniaxial Schmid factor reaches maximum. For Ni, S varies by about 20% from minimum to maximum value. For NiAl, the variation of S is about 40%.

Most pop-in analyses used the Hertzian isotropic contact results and found the maximum shear stress (as opposed to maximum resolved shear stress) along the symmetry axis. The consideration of elastic anisotropy and slip systems will lead to different results. Figure 2.3 plots the location where the resolved shear stress fields of all possible slip systems reach maximum for NiAl single crystal under spherical indentation as a function of the indentation direction. Since these locations do not vary significantly along the depth direction, i.e., $x_3 = -(0.43 \pm 0.03)a$, we thus plot the location trajectory on the (x_1, x_2) plane when the indentation direction varies along $[mm1]$, $[m\frac{m}{2}1]$, and $[m01]$ with m varying from 0 to 1. These locations can be very far from the contact center, especially when the surface normal is close to $\langle 110 \rangle$.

2.4 Effective Indentation Modulus of Elastically Anisotropic Solids

For an elastically isotropic half-space indented by an axisymmetric, frictionless indenter, the classic Sneddon solution gives the contact stiffness, $S_n = 2aE_r$ [54], where the reduced indentation modulus is $E_r = \left[\left(1-\nu_s^2\right)/E_s + \left(1-\nu_i^2\right)/E_i\right]^{-1}$. Using the cumulative superposition method [41], with an increment of the indentation penetration, the contact problem can be regarded as being superposed with a flat-ended circular punch contact with radius equal to the current contact size. The relationship between contact size and indentation depth is not needed for the interest of contact stiffness. Consequently, the relationship, $S_n = 2aE_r$, is valid for any axisymmetric contact, irrespective of the actual indenter shape. However, a correction factor needs to be introduced when the contact is frictional, or the contact shape is non-circular, or the two solids cannot be approximated by elastic half-spaces.

For an elastically anisotropic half-space indented by a flat-ended circular/elliptical indenter or a paraboloid of revolution (i.e., Hertzian contact), the deformation fields have been solved using the surface-displacement Green's function [36,37,51]. For arbitrary indenters, according to the cumulative superposition method, the contact stiffness is still given by a flat-ended punch contact problem with the end shape given by the current contact shape. During indentation, the shape of the contact area, however, does not necessarily remain the same even for an axisymmetric indenter. For example, the contact shape for Hertzian contact is elliptical, but the elliptical contact area is only an approximation for a conical indentation. For a conical indenter with a dull spherical tip, the contact shape thus varies during the indentation. From a practical standpoint, we can determine the indentation modulus from the circular contact on an elastically anisotropic half-space, and the result does not differ noticeably from an arbitrary axisymmetric indentation problem [36,37].

The effective indentation modulus E_{eff} is determined from the Green tensor in Eq. (2.16), giving rise to

$$E_{eff} = \left\{ \frac{1}{2} \int_0^{2\pi} B_{33}\left(h_1, h_2\right) d\theta \right\}^{-1}. \tag{2.25}$$

Figure 2.4 plots the contours of E_{eff} for Ni and NiAl single crystals. Both crystals have the elastic anisotropy parameter, $\left(c_{12} + 2c_{44}\right)/c_{11} > 1$, so that $E_{eff}^{111} > E_{eff}^{101} > E_{eff}^{001}$.

2.5 An Approximate Formulation of the Effective Indentation Modulus of Elastically Anisotropic Film-on-Substrate Systems

For a film-on-substrate system, the contact stiffness is again given by a flat-ended punch contact, while the contact size and shape are determined by the indenter shape, indentation depth (or applied load), and elastic properties of film and substrate materials. For a flat-ended punch contact, the contact pressure distribution has to be determined by solving a set of integral equations. This difficulty can be avoided by assuming a circular contact with pressure of the form of $\left[1-\left(r/a\right)^2\right]^{-1/2}$, which allows us to derive an approximate representation of the effective modulus. Such a pressure distribution is the analytical solution for flat-ended circular punch contact on an elastic (either isotropic or anisotropic) half-space. As shown in [40], this assumption agrees extremely well with the finite element simulations for both normal and tangential contacts on elastically isotropic film-on-substrate systems.

The contact pressure is assumed to be

$$\sigma_{33} = \frac{t_0}{\sqrt{1-r^2/a^2}}, \tag{2.26}$$

with $r^2 = x_1^2 + x_2^2$, so that the total normal force is $F_n = 2\pi a^2 t_0$. The surface deflection in the normal direction is

$$u_3\left(x_1, x_2, 0\right) = \iint_A \frac{t_0}{\sqrt{1-\left(x_1^2 + x_2^2\right)/a^2}} w_{33}\left(x_1 - x_1', x_2 - x_2'\right) dx_1' dx_2', \tag{2.27}$$

where w_{33} is a component of the Green tensor in Eq. (2.11), i.e., the normal surface deflection at $\left(x_1, x_2\right)$ due to a point force applied in x_3 direction at $\left(x_1', x_2'\right)$. Substituting the two-dimensional Fourier transform of w_{33} (i.e., transforming x_α to ξ_α) into Eq. (2.27) gives

$$u_3\left(x_1, x_2, 0\right) = \frac{t_0}{2\pi} \iint \hat{w}_{33}\left(\eta_\alpha / a; d\right) e^{-i\boldsymbol{\eta}\cdot\mathbf{y}} d\eta_1 d\eta_2 \iint_{y' \le 1} \frac{1}{\sqrt{1-y'^2}} e^{i\boldsymbol{\eta}\cdot\mathbf{y}'} dy_1' dy_2', \tag{2.28}$$

where $\eta_\alpha = a\xi_\alpha$, $y_\alpha = x_\alpha / a$, and $y = \sqrt{y_1^2 + y_2^2}$. Using the relationship,

$$\frac{1}{2\pi} \iint_{y' \le 1} \frac{1}{\sqrt{1-y'^2}} e^{i\boldsymbol{\eta}\cdot\mathbf{y}'} dy_1' dy_2' = \int_0^1 \frac{y'}{\sqrt{1-y'^2}} J_0\left(\eta y'\right) dy', \tag{2.29}$$

and the definition in Eq. (2.12) gives

$$u_3\left(x_1, x_2, 0\right) = a t_0 \int_0^1 \frac{y'}{\sqrt{1-y'^2}} dy' \int_0^{2\pi} d\theta \int_0^\infty \hat{W}_{33}\left(\theta, \eta \frac{d}{a}\right) \cos\left[\eta y \cos\left(\theta - \phi\right)\right] J_0\left(\eta y'\right) d\eta, \tag{2.30}$$

with $\phi = \tan^{-1}\left(y_2 / y_1\right)$. Consequently, we define the effective indentation modulus of film-on-substrate system as

$$E^* = \frac{F_n}{2a u_3^*} = \frac{\pi a t_0}{u_3^*}, \tag{2.31}$$

with $u_3^* = \frac{1}{\pi a^2} \iint_A u_3\left(x_1, x_2, 0\right) dx_1 dx_2$.

Now consider some degenerate cases. For a homogeneous and elastically isotropic half-space, $\hat{W}_{33} = \left(1-\nu^2\right)/\pi E$, and Eq. (2.30) becomes a constant, namely,

$$u_3 = \pi^2 a t_0 \hat{W}_{33} = F_n\left(1-\nu^2\right)/2aE, \tag{2.32}$$

which recovers the Sneddon's solution. For a homogeneous and elastically anisotropic half-space, $\hat{W}_{33} = \hat{W}_{33}\left(\theta\right)$, and Eq. (2.30) is again a constant, given by

$$u_3 = \frac{\pi a t_0}{2}\int_0^{2\pi} \hat{W}_{33}(\theta)\,d\theta = \frac{F_n}{4a}\int_0^{2\pi} \hat{W}_{33}(\theta)\,d\theta\,. \tag{2.33}$$

Therefore, the effective modulus is defined by $E^* = \left[\frac{1}{2}\int_0^{2\pi} \hat{W}_{33}(\theta)\,d\theta\right]^{-1}$, which agrees with the literature results [36,37]. This is the same representation as Eq. (2.25). For an elastically isotropic film-on-substrate system, $\hat{W}_{33} = \hat{W}_{33}(\eta d/a)$, and Eqs. (2.30) and (2.31) have been evaluated in the earlier work [40].

We choose fused silica as the substrate material (isotropic, E=71GPa and ν=0.17), and copper and nickel single crystals as the film material with surface normal in the (001) or (111) direction. For copper, the elastic constants in contracted form are c_{11}=168.4GPa, c_{12}=121.4GPa, and c_{44}=75.4GPa. For nickel, they are c_{11}=244GPa, c_{12}=158GPa, and c_{44}=102GPa. It should be noted that the degrees of anisotropy, as defined by $(c_{12}+2c_{44})/c_{11}$, for both copper and nickel single crystals are larger than unity. For a generally anisotropic film-on-substrate system, the Green's function in Eq. (2.11) can be easily calculated from an algebraic eigenvalue problem, while the time-consuming part is the evaluation of the triple integral in Eq. (2.30). An efficient method for the evaluation of integrals with highly oscillatory integrand, e.g., the Bessel function in our case, is discussed below.

The method in [55-57] is adopted to efficiently evaluate integrals with highly oscillatory integrands. The integral of our interest, Eq. (2.30), is the Bessel-trigonometric transformation:

$$I = \int_a^b g(x)\,e^{ir_1 x} J_0(r_2 x)\,dx\,, \tag{2.34}$$

where $g(x)$ is a non-rapidly oscillatory function. Define an auxiliary function $\mathbf{w}(x) = e^{ir_1 x}\left(J_0(r_2 x),\, J_1(r_2 x)\right)^{\mathrm{T}}$. The properties of Bessel functions lead to $\mathbf{w}'(x) = \mathbf{A}(x)\mathbf{w}(x)$,

$$\mathbf{A}(x) = \begin{pmatrix} ir_1 & -r_2 \\ r_2 & ir_1 - 1/x \end{pmatrix}. \tag{2.35}$$

Our goal is to find a vector, $\mathbf{p}(x) = \left(p_1(x), p_2(x)\right)$, which satisfies

$$\mathbf{p}'(x) + \mathbf{p}(x)\,\mathbf{A}(x) = \left(g(x), 0\right)^{\mathrm{T}}, \tag{2.36}$$

so that

$$\left(\mathbf{p}(x)\,\mathbf{w}(x)\right)' = \mathbf{p}'(x)\,\mathbf{w}(x) + \mathbf{p}(x)\,\mathbf{w}'(x) = g(x)\,e^{ir_1 x} J_0(r_2 x)\,. \tag{2.37}$$

Consequently, the integral in Eq. (2.34) is given by

$$I = \int_a^b g(x) e^{ir_1 x} J_0(r_2 x)\, dx = \mathbf{p}(b)\mathbf{w}(b) - \mathbf{p}(a)\mathbf{w}(a). \tag{2.38}$$

The problem of evaluating Eq. (2.34) is thus transformed into the problem of finding a non-rapidly-oscillatory particular solution of $\mathbf{p}(x)$ from Eq. (2.36) with no boundary conditions prescribed. The procedure to find an approximation of this particular solution is given by a collocation method in [55-57].

The accuracy of our approximate representation in Eqs. (2.30) and (2.31) is compared to detailed three-dimensional finite element simulations using the commercial software ABAQUS. A flat-ended circular punch with a fixed radius a is indented into the film-on-substrate system. The film thickness varies from 0 to $5a$ and frictionless condition is adopted. The fine mesh size is $0.0125a$ near the contact edge and the maximum indentation depth is $0.01a$. Because of crystallographic symmetry, 1/8 of the half-space is used for (001) indentation and 1/6 for (111) indentation. The calculation cell size is $500a$, so that the faraway boundary conditions have negligible contributions to the contact stiffness. The entire model includes 47,240 six- and eight-node elements (C3D6 and C3D8).

Figure 2.5 compares the theoretical prediction (solid lines) of the effective indentation modulus E^*, as normalized by the effective modulus of fused silica E^*_{II}, to the finite element results (discrete markers, only for the copper film on fused-silica system). It is found that E^* is a monotonic function of the ratio d/a. As $d/a \to 0$, the effective modulus approaches that of the substrate material, i.e., $E^* \to E^*_{\mathrm{II}}$. The asymptotic limit, E^*_{I}, can be calculated from Eq.(2.33), being $E^*_{Cu(001)}$=134GPa, $E^*_{Cu(111)}$=152GPa, $E^*_{Ni(001)}$=203GPa, and $E^*_{Ni(111)}$=223GPa. However, it is difficult to approach this asymptotic limit as $d/a \to \infty$. For copper on fused silica systems, this limit is practically reached when $d/a > 15$; for nickel on fused silica systems, $d/a > 20$. A larger d/a is needed if $\left|E^*_{\mathrm{I}} - E^*_{\mathrm{II}}\right| / E^*_{\mathrm{II}}$ increases. In addition, we note that the prediction and finite element results differ the most when $d/a \sim 1$, mainly due to the difference between the assumed pressure distribution, $\left[1-(r/a)^2\right]^{-1/2}$, and the exact solution at this d/a regime.

The use of load-displacement curves obtained from instrumented nanoindentation technique cannot accurately determine the film properties because of the difficulty of decoupling the film deformation behavior from substrate effects. In practice, the indentation

depth is often limited to less than 10% of the film thickness in order to minimize the effect of the substrate on the measurement. Our results in Fig. 2.5 suggest that this empirical rule is overestimated. When both film and substrate deform elastically, a large cutoff ratio, e.g., $d/a \sim 15$, is required for the effective indentation modulus to approach that of the film material. For Berkovich indenter, this cutoff corresponds to $d/\delta_n \sim 25$ with indentation depth δ_n. The effective indentation modulus for copper on fused silica at indentation depth being 10% of the film thickness is found to be about 10% less than the indentation modulus of copper. Consequently, an alternative and commonly used approach is to utilize the measurements at intermediate indentation depths, based on the elastic prediction of E^* as a function of d/a and the elastic constants of film and substrate effects. As shown in this work, the derivation of this relationship is highly simplified because the use of cumulative superposition method avoids determining the relationship between contact size and depth. However, one major difficulty of this approach is that the indentation modulus derived from the contact stiffness measurement may differ significantly from the theoretical prediction because of the strong dependence of contact stiffness on material pileup/sink-in, contact shape, friction, and modulus mismatch.

Even for elastic contact, a correction factor β_n needs to be introduced in the relationship between contact stiffness S_n and effective indentation modulus E^*, $S_n = 2aE^*\beta_n$ [40]. For an elastically isotropic half-space, $\beta_n = 1$ for frictionless circular contact, and will be off unity for frictional and non-circular contact. For elastic-plastic contact, the contact stiffness should be derived from the contact between the indenter and a deformed surface, since the analytical elastic-contact solution is only valid for half-space contact problems. The correction factor may vary considerably with respect to the material pileup or sink-in due to plastic deformation. Our preliminary finite element simulations have shown that β_n varies within 0.7~1.3 when using a range of cube-corner to Berkovich indenters, frictionless to infinite friction condition, and elastic to very soft material ($E/\sigma_Y \sim 1/1000$ with yield stress σ_Y). For elastic-plastic contact on film-on-substrate system, this correction factor also depends on additional parameters such as modulus and strength mismatch. Consequently, in order to compare the theoretically predicted indentation modulus to the nanoindentation measurements, we either need to conduct heady-duty finite element simulations to obtain an accurate relationship of $S_n = 2aE^*\beta_n$, or incorporate additional experimental information

such as the topography measurement or the use of multiple indenters with varying indenter angle or radius.

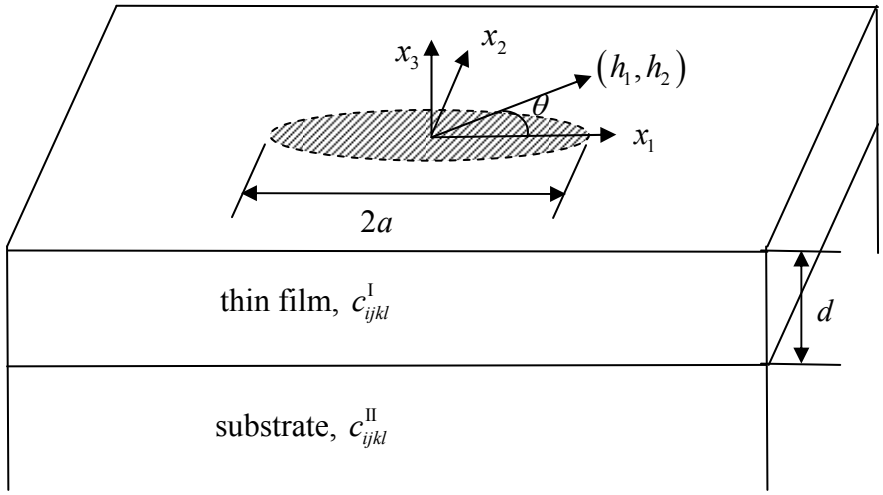

Figure 2.1 Schematic illustration of the film-on-substrate system under a circular contact. The unit vector (h_1, h_2), lying on the (x_1, x_2) plane, gives the direction cosines of the wavevector $\boldsymbol{\xi} = (h_1, h_2)\xi$.

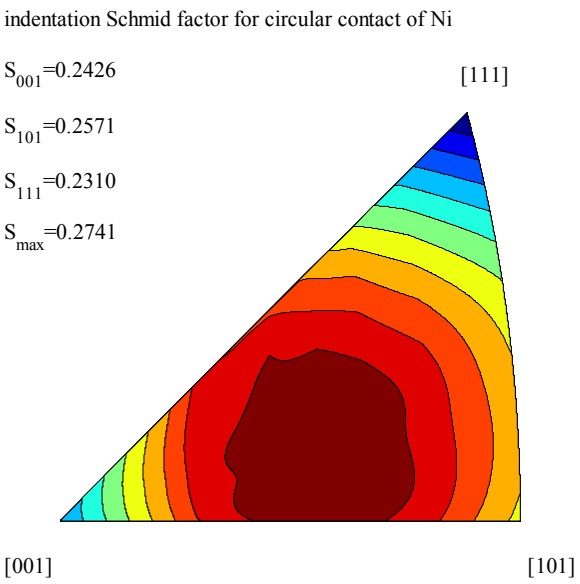

(a)

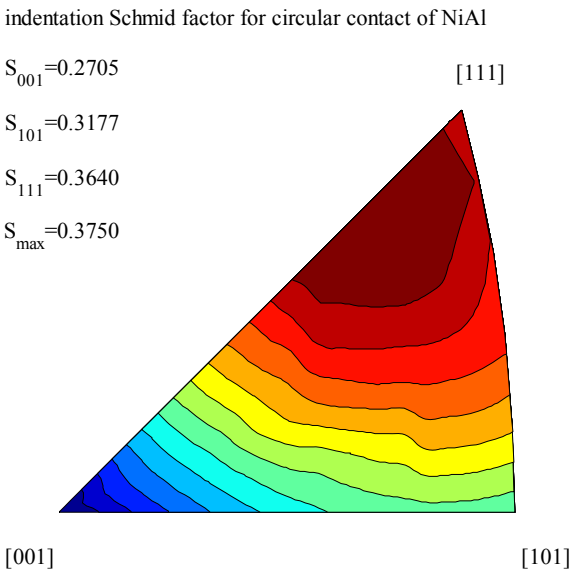

(b)

Figure 2.2 Contours of the indentation Schmid factor of elastically homogeneous anisotropic solids under spherical indentation, defined as the ratio of maximum resolved shear stress to the maximum contact pressure on a homogeneous substrate, plotted for (a) Ni single crystal with FCC structure and $\{111\}\langle 0\bar{1}1\rangle$ slip systems, and (b) NiAl single crystal with B2 structure and $\{110\}\langle 001\rangle$ slip systems.

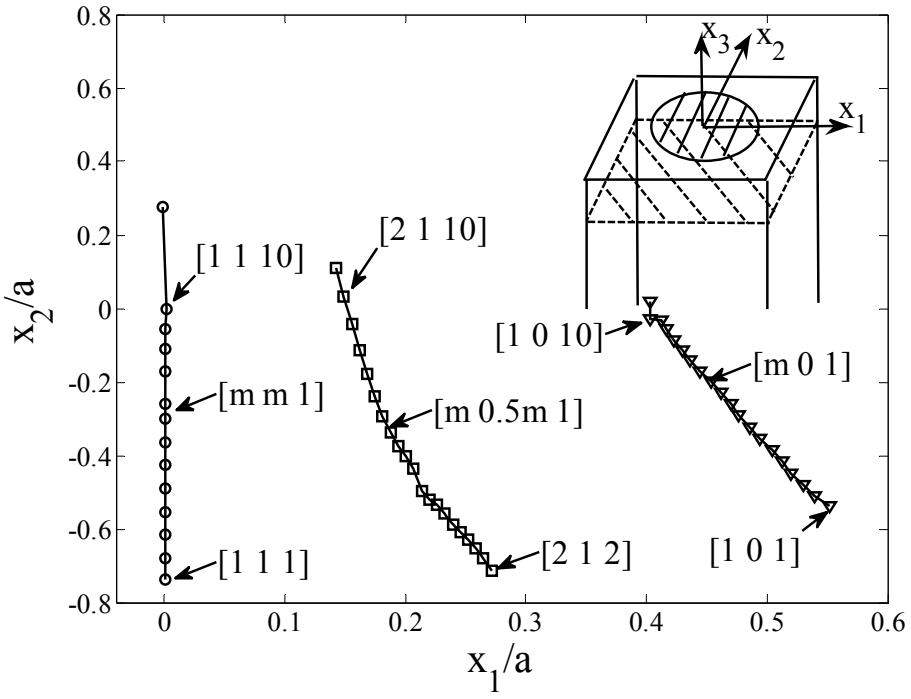

Figure 2.3 The location where the resolved shear stress fields of all possible slip systems reach maximum for NiAl single crystal under spherical indentation depends on the indentation orientation. Since these locations do not vary significantly along the depth direction, i.e., $x_3 = -(0.43 \pm 0.03)a$, we thus plot them on the (x_1, x_2) plane along $[mm1]$, $[m\frac{m}{2}1]$, and $[m01]$ with m varying from 0 to 1.

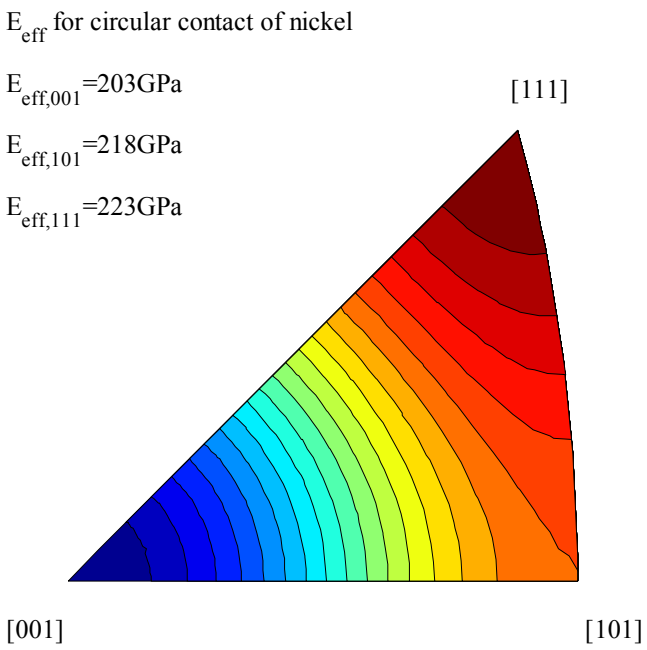

(a)

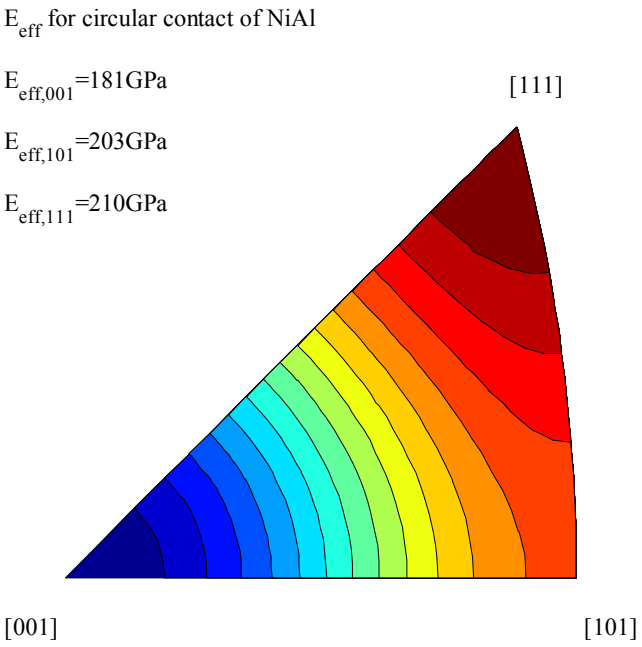

(b)

Figure 2.4 Contours of the effective indentation modulus of elastically homogeneous anisotropic solids under spherical indentation, plotted for (a) Ni and (b) NiAl single crystals.

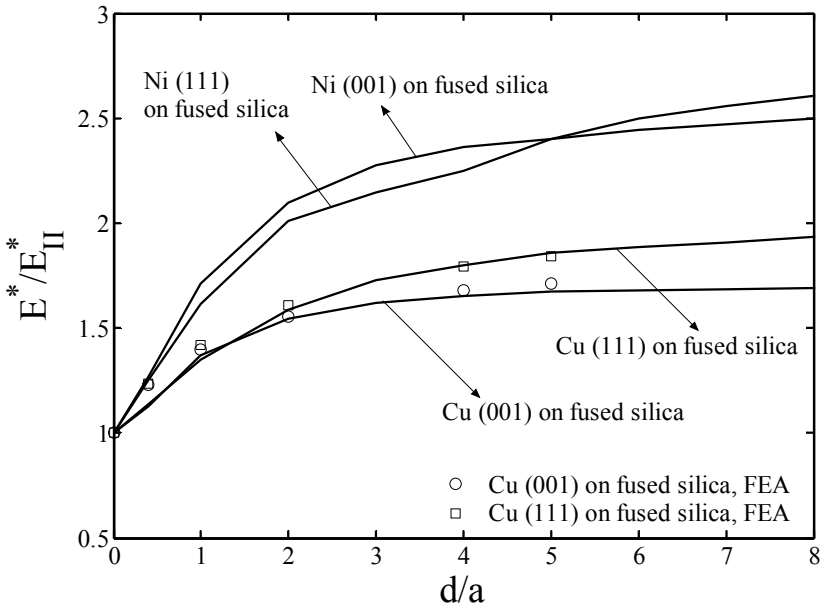

Figure 2.5 Effective modulus of the film-on-substrate system, as normalized by the effective modulus of the substrate, plotted against the ratio of film thickness d to contact radius a. Solid lines are predictions from Eq. (2.31), and discrete markers are results from finite element analysis (FEA). Film materials are copper and nickel with surface normal in the (001) and (111) directions, and substrate material is fused silica.

Chapter III

Activation Energy for Thermally Activated, Dislocation Nucleation Process

3.1 Introduction

As described in previous chapters, the nanoindentation pop-in event in defect-free single crystals is a result of homogeneous dislocation nucleation underneath the indenter. When the maximum resolved shear stress underneath the indenter reaches the theoretical strength of the material, dislocation will nucleate homogeneously, multiply and cause the indenter to suddenly jump into the specimen. The homogeneous dislocation nucleation process is a stress-assisted, thermally activated process. When the applied load is less than but close to the critical load for homogeneous dislocation nucleation, the thermal energy can activate the dislocation nucleation process. Therefore, the activation energy for dislocation nucleation is an important issue and needs to be quantitatively studied.

A dislocation is usually modeled either by the Volterra model, which treats the dislocation as a mathematical discontinuity, or by the Peierls-Nabarro model, which treats the dislocation core as a continuous slip field [58]. From the Volterra dislocation model, closed form solutions can be derived for various dislocation activities such as dislocation mutual interactions [58,59], interactions with other material defects [60-64], and interactions with other geometric features [22,23,65]. From the Peierls-Nabarro dislocation model, a number of numerical modeling methods have been developed to study dislocation activities in more complicated scenarios [65-73].

In this Chapter, we first briefly describe how to calculate the activation energy for homogeneous dislocation nucleation from the Volterra dislocation model. Then, we introduce a new method which implements the Rice-Peierls theory [74, 75] into finite element analysis to model dislocation activities. The advantage of using finite element method (FEM), compared to other numerical methods such as the variational boundary integral method, is that it can solve more complex problems, and it costs less computation time when compared to molecular simulations. In our method, a dissipative cohesive interface model which treats the dislocation core as a continuous, inhomogeneous lattice slip field is implemented into the slip plane. We find the relative slip field on the slip plane by balancing the force introduced from our cohesive interface model and the applied force. We then use our method to solve

problems of homogeneous dislocation nucleation, dislocation nucleation from a planar crack tip, and trailing partial dislocation nucleation after a leading partial dislocation has emitted from a crack tip. The activation energy for dislocation nucleation can be obtained from the stable and saddle-point solutions when the applied load is less than the athermal limit.

3.2 Activation Energy for Homogeneous Dislocation Nucleation by the Volterra Dislocation Model

Consider a Volterra dislocation loop with radius ρ under an applied shear stress τ in an infinite solid. The total potential energy is [58]

$$\Pi_{total} = \frac{\mu b^2 \rho}{4}\left(\frac{2-\nu}{1-\nu}\right)\ln\left(\frac{8\rho}{e^2 r_0}\right) - \pi\rho^2\tau b, \tag{3.1}$$

where r_0 is the dislocation core cut-off size, μ the shear modulus, b the magnitude of Burger vector, and ν Possion's ratio. The first term is the self-energy of the dislocation loop and the second term is the work done by the applied stress. The theoretical strength is achieved when $\partial\Pi_{total}/\partial\rho = 0$ and $\partial^2\Pi_{total}/\partial\rho^2 = 0$, leading to,

$$\tau_{crt} = \frac{\mu b}{\pi e^2 r_0}\left(\frac{2-\nu}{1-\nu}\right). \tag{3.2}$$

When $\tau < \tau_{crt}$, there are two solutions of ρ lead to the extrema of Π_{total}, denoted as $\rho_{\min}$ and ρ_{saddle} ($\rho_{\min} < \rho_{saddle}$). The activation energy is therefore,

$$\Delta\Pi = \Pi_{total}\left(\rho_{saddle}\right) - \Pi_{total}\left(\rho_{\min}\right) \tag{3.3}$$

The solution of the activation energy will be presented shortly.

3.3 Activation Energy for Homogeneous Dislocation Nucleation by the Rice-Peierls Dislocation Model

Consider an infinite solid under pure shear stress. The homogeneous dislocation nucleation will occur when the applied load reaches the theoretical strength of the material. Our three-dimensional finite element model is shown in Fig. 3.1 for this case. A half model is used because of symmetry about the *x*-*z* plane. In two dimensional analysis, the shear stress on the slip plane is taken to be a periodic function of the relative slip across the slip plane [74, 75], δ,

$$\tau = \tau_{\max} \sin\left(\frac{2\pi\Delta}{b}\right) \tag{3.4a}$$

$$\delta = \Delta - \frac{b}{2\pi}\sin\left(\frac{2\pi\Delta}{b}\right) \tag{3.4b}$$

where $\tau_{\max}$ the interface theoretical strength in shear, and Δ the relative atomic displacement across two adjacent atomic layer. The relationship of δ and Δ in Eq. (3.4b) is introduced so that the initial slope of $\tau \sim \Delta$ is infinite (Rice, 1992). The slip field on the slip plane is determined by balancing the force due to applied field and the force due to lattice disregistry. The interplanar potential on the slip plane is,

$$\Phi(\Delta) = \frac{\tau_{\max} b}{\pi}\sin^4\left(\frac{\pi\Delta}{b}\right) \tag{3.5}$$

A dislocation is considered to nucleate when $\Delta = b/2$, corresponding to the moment that the interplanar potential $\Phi(\Delta)$ on the slip plane reaches its maximum, i.e. $\frac{\tau_{\max} b}{\pi}$.

The total potential energy Π as a functional of the interface slip field, $\mathbf{\Delta}$ is [78],

$$\Pi = \Pi_0 + \int_S \Phi(\mathbf{\Delta}) dS + \frac{1}{2}\int_S \mathbf{n}\cdot\tilde{\boldsymbol{\sigma}}\cdot\mathbf{\Delta} dS - \int_S \mathbf{n}\cdot\boldsymbol{\sigma}^{elastic}\cdot\mathbf{\Delta} dS \tag{3.6}$$

where, $\mathbf{n}$ denotes the interface normal, $\tilde{\boldsymbol{\sigma}}$ is the self stress due to a non-uniform $\mathbf{\Delta}$ when the externally applied force is zero, and $\boldsymbol{\sigma}^{elastic}$ is the elastic stress fields when $\mathbf{\Delta} = 0$ (i.e., when there is no dislocation). In Eq. (3.6), Π_0 is the potential energy of the elastic system when there is no dislocation, the second term is the energy gained on the slip plane when dislocation slips, the third term is the energy change of the elastic solids outside the slip plane duce to the introduced dislocation, and the last term is the interaction energy between the elastic stress field and the relative slip on the slip plane. The equilibrium slip distribution corresponds to a stationary potential energy.

To calculate the relative slip fields of the slip plane, we implement the above formulation into a commercial finite element package, ABAQUS, via a User-defined ELement (UEL) subroutine. It should be noted that, in two dimensional analysis, the slip plane is prohibited to open in its normal direction, and Eq. (3.4) is used along the slip direction. In three dimensional analysis, the slip plane is constrained in the normal direction, and shear stresses along the slip direction and the direction normal to the slip on the slip plane, respectively, have the form of,

$$\tau_{zx} = \tau_{\max} \sin\left(\frac{2\pi\Delta_x}{b}\right) \tag{3.7a}$$

$$\tau_{zy} = \tau_{\max} \sin\left(\frac{2\pi\Delta_z}{b}\right) \tag{3.7b}$$

where Δ_x and Δ_z are atomic slip disregistry along x and z direction respectively. More realistic γ surface can be found from literature [76, 77], but we here just use a simple one to illustrate the efficiency of our method.

Because the interplanar potential is periodic, dislocation nucleation corresponds to an elastic snap-back instability that occurs after the total potential energy reaches its peak. When the total potential energy is less than its peak value, there are two solutions on the slip plane. One solution corresponds to the minimum potential energy state, denoted as the stable solution, and the other one is the saddle point solution. Each solution has its result of $\delta_{\min}(x,y)$ and $\delta_{sad}(x,y)$ on the slip plane ($\delta_{\min}(x,y) < \delta_{sad}(x,y)$), and the activation energy of dislocation nucleation can be evaluated from Eq. (3.6) by,

$$\Delta\Pi^{3D} = \Pi\left[\delta_{\text{sad}}(x,y)\right] - \Pi\left[\delta_{\min}(x,y)\right]. \tag{3.8}$$

The stable solution can be obtained straightforwardly from Newton-Raphson method used in the Abaqus solver. To obtain the saddle point solution, an initial trial function of $\delta^*_{sad}(x,y)$ is prescribed on the slip plane. If this guess is near the saddle point solution, the Newton-Raphson iteration, in this case, will quickly converge to the saddle point solution.

The saddle point solution of the slip disregistry field, δ_x, on the slip plane at $y = 0$ is given in Fig. 3.2(a), which is the same as Xu and Argon's results [67] from a variational boundary integral method. Fig. 3.2(b)-(c) show the saddle point dislocation loop configuration on the slip plane at different load levels. The dislocation loop at the applied shear stress level $\tau_{appl}/\tau_{\max} = 0.5$ in Fig. 3.2(b) has a larger size than the dislocation loop at $\tau_{appl}/\tau_{\max} = 0.9$ in Fig. 3.2 (c). That is, from Eq. (3.8), the smaller the applied stress is, the larger the activation energy of dislocation nucleation will be. Therefore, the dislocation nucleation is a stress assisted process. Fig. 3.3 shows the normalized activation energies with respect to various shear stress levels.

A comparison of various dislocation nucleation models, including Volterra model in Section 3.2, Rice-Peierls model in this section, and molecular simulations is given in Fig. 3.4 and Table 3.1. It is generally found that the activation energy can be fitted to

$\Delta\Pi = A\left(1-\tau_{appl}/\tau_{th}\right)^n$, where n and A are fitting parameters, τ_{appl} is the applied resolved shear stress on the dislocation, and τ_{th} is the theoretical strength of the material. Fitting results are shown in Table 3.1, where n is found to be about 1.5-4.5 and the pre-factor $A/Gb^3 \approx 5-15$. Temperature effects on elastic constants and pre-factor A are not considered in this work, while literature result suggested $A = 1-T/T_m$ with melting temperature T_m [71].

3.4 Heterogeneous Dislocation Nucleation from a Crack Tip

Consider a half infinite crack that emits an edge dislocation from the tip under a mode II k-field (Fig. 3.5a). The slip plane is assumed to be coplanar with the crack. The shear stress on the slip plane is taken to obey the same periodic function with respect to the relative slip field as in Eq. (3.4) in two dimensional analysis and as Eq. (3.7) in three dimensional analysis. According to Rice and Beltz [76, 77], the dislocation is considered to nucleate from the crack tip when the applied energy release rate G_{appl} reaches the maximum interplanar potential on the slip plane which is denote as G_{crt} (from Eq. (3.5), $G_{crt} = \frac{\tau_{\max} b}{\pi}$). In our finite element model in Fig. 3.5b, a half infinite planar crack lies on the x-z plane with a coplanar slip plane ahead of the crack tip. The model has a thickness of H. We assume the Burgers vector is along the x direction. Because of symmetry in x-y plane at $z = -H$, only half space in Fig. 3.5a is meshed. The outer surface of the model (i.e. the plane at $z = 0$) in Fig. 3.5b is fixed with the normal displacement to ensure the plane strain condition. Mode II displacement boundary conditions are applied on the outer boundary in Fig. 3.5b , which in cylindrical coordinates (r,θ), are given by

$$\begin{Bmatrix} u_x \\ u_y \end{Bmatrix} = \frac{K_{II}}{2E}\sqrt{\frac{r}{2\pi}} \begin{Bmatrix} (1+\nu)\left[(2\kappa-1)\cos\frac{\theta}{2} - \cos\frac{3\theta}{2}\right] \\ (1+\nu)\left[(2\kappa+1)\sin\frac{\theta}{2} - \sin\frac{3\theta}{2}\right] \end{Bmatrix} \tag{3.9}$$

where $\kappa = 3-4\nu$, K_{II} is the mode II stress intensity factor, E is Young's modulus, and ν is Poisson's ratio (equal to 0.3 in our analysis).

We first compare our results with Rice and Beltz's results [75] in two-dimensional analysis. In this case, the crack tip has the relative slip of,

$$\delta_{tip} = \Delta_{tip} - \left(\frac{b}{2\pi}\right)\sin\left(\frac{2\pi\Delta_{tip}}{b}\right) \tag{3.10}$$

where Δ_{tip} has the relationship with the applied energy release rate G_{appl},

$$G_{appl} / G_{crt} = \sin^4\left(\frac{\pi\Delta_{tip}}{b}\right) \tag{3.11}$$

where $G_{appl} = (1-\nu)(K_{II})^2 / 2\mu$. Solutions of $\delta_{\min}(x)$ and $\delta_{sad}(x)$ are shown in Fig. 3.6. They are exactly the same as Rice and Beltz's. It is expected because essentially we have solved the same equilibrium equation with same boundary conditions: one by solving the integral equation in Rice and Beltz, and the other by finite element method in our work. The 2D activation energy results of dislocation nucleation from crack tip are shown in Fig. 3.7. We also compare our results that use slanted model of Eq. (3.4) in the cohesive plane to those using the simple sinusoidal model [65]. It is seen that the simple sinusoidal model has larger activation energy than the slanted model at the same applied load level. This is because the slanted model gives an infinite slope at $\delta = 0$, which means it is harder for the slanted model to open at small relative slip of the slip plane than the simple sinusoidal model. However, G_{crt} for dislocation nucleation from the crack tip for both models are the same. The simple sinusoidal model causes much less convergence problem during computation than the slanted model. If one only needs to find the critical condition for dislocation nucleation, the simple sinusoidal model will be an ideal choice.

As an advantage of finite element analysis, we extend our model into three-dimensional computation. In Fig. 3.8, the dislocation loop from the planar crack tip is visualized by the relative slip field at $G_{appl} / G_{crit} = 0.9$ in Fig. 3.8 (a) and $G_{appl} / G_{crit} = 0.7$ in Fig. 3.8 (b). The dislocation loops are represented by the relative slip distribution in *x* direction on the slip plane. Similar to the homogeneous dislocation nucleation, a large applied load will facilitate dislocation nucleation from the crack tip because it corresponds to a reduced activation energy. Also, the maximum δ in our results does not exceed the magnitude of a Burgers vector. Therefore, the assumption used in the 3D asymptotic analysis (i.e. $\varepsilon / b > 0.2$, where ε is the perturbation value) in Ref. [75] will overestimate the relative slip on the slip plane. Admittedly, the maximum δ is also related to the angle between the slip plane and the crack tip [72], and the ratio between K_{II} and K_{III} [66, 70]. Future work is needed to see if there exists a saddle point solution on the slip plane when a full dislocation has already been

generated and moved away from the crack tip (i.e. the maximum δ on the slip plane is larger than a Burgers vector).

We also examine another prediction by Rice and Beltz in Ref. [75]. In their work, they use the asymptotic method to obtain an approximate saddle point solution, consisting of a local protrusion of a dislocation loop. They argued that the activation energy, $\Delta\Pi^{3D}$, for three-dimensional dislocation nucleation varies with the model thickness H in Fig. 3.5b and is close to the product of $\Delta\Pi^{2D}$ and H (i.e. $\Delta\Pi^{3D} \approx H\Delta\Pi^{2D}$) when H is small, because the small thickness does not allow the development of the local protrusion in the thickness direction and thus force the saddle-point solution to be a independent of z. And $\Delta\Pi^{3D}$ should reach a plateau as H increases. They calculated a case when the applied energy release rate is close to the critical value (i.e., $G_{appl} / G_{crit} = 0.9$) where their asymptotic approximation is most reliable, and found out that $H\Delta U^{2D}$ agrees with the actual $\Delta\Pi^{3D}$ up to H about 17b. We verify their prediction in Fig. 3.9. Three-dimensional activation energies at $G_{appl} / G_{crit} = 0.9$ (shown in circle mark solid line), and $G_{appl} / G_{crit} = 0.7$ (shown in square mark solid line) are given as a function of thickness H/b. $H\Delta\Pi^{2D}$ is plotted as solid lines to compare with the 3D results. Our results exhibit the same trend as that predicted by Rice and Beltz. In our simulations, $H\Delta\Pi^{2D}$ is close to $\Delta\Pi^{3D}$ until H reaches about 13b.

3.5 Trailing or Twinning Partial Dislocation Nucleation from a Crack Tip

After a leading partial dislocation has been emitted from a crack tip, if it is followed by a trailing partial dislocation on the same slip plane, a stacking fault will be created. On the other hand, if the leading partial dislocation is followed by a twinning partial dislocation of the same Burgers vector on the adjacent slip plane, deformation twinning (DT) occurs and the subsequent partial dislocation of the same character will follow in a similar behavior, thus widening and extending the twin region outwards. DT is usually assumed to heterogeneously nucleate at pre-existing defect sites in materials such as grain boundaries, dislocations and dislocation pile-ups, surfaces and crack tips. Warner et al. [73] studied the competition between trailing and twinning partial dislocation nucleation from a crack tip under mode I loading using multiscale simulation in two-dimensional analysis. They found the transition state that the activation energy for trailing partial dislocation emission becomes lower than that for twinning partial dislocation with respect to the decrease of applied load, thus leading

to longer times or slower strain rates for the twinning partial to occur in their study. Here we present our results of a trailing partial dislocation nucleation criterion from a crack tip under mode II loading after a leading partial dislocation has been emitted. The corresponding relative slip distributions of the slip plane under different load levels have been calculated. Twinning partial dislocation simulation will be left as a future work.

The slip potential Φ along the leading to trailing slip path is [79],

$$\Phi = a_1 \sin^2 \frac{\pi\delta}{2b} + a_2 \sin^2 \frac{\pi\delta}{b} \tag{3.12}$$

where $a_1 = \gamma_{ssf}$ and $a_2 = \dfrac{\gamma_{usf} - \dfrac{a_1}{2} + \sqrt{\gamma_{usf}^2 - a_1\gamma_{usf}}}{2}$. γ_{ssf} and are the extrema of Φ, given by 6.616 and 8.007 (meV/Å^2) for Al single crystals. Fig. 3.10 shows the γ potential on the slip plane, i.e. Eq. (3.12), normalized by the unstable stacking fault energy, γ_{usf}, along the leading-to-trailing partial dislocation slip path as a function of relative slip along the slip path. Here, for each G_{appl} between γ_{ssf} and γ_{usf}, there are four solutions denoted as "A", "B", "C" and "D". "A" and "C", respectively, are stationary solutions of the leading partial dislocation and the following trailing partial dislocation nucleation. "B" and "D", respectively are saddle point solutions for the leading partial dislocation nucleation and trailing partial dislocation nucleation. The total energy and activation energy equation can be obtained by substituting Eq. (3.12) into Eq. (3.6) and Eq. (3.8). "A" can be directly obtained from Newton-Raphson algorithm. "B", "C" and "D" are obtained with similar technique that has been introduced in the previous section. We prescribe trial relative slip distributions on the slip plane near the actual solution of "B", "C" and "D" and our Newton-Raphson iterations will converge to the actual solutions.

The relative slip fields of the slip plane corresponding to "A", "B", "C" and "D" points along the slip plane are shown in Fig. 3.11. As expected, when the applied load increases, these relative slip profiles will move closer to each other, corresponding to the athermal nucleation event.

Table 3.1 The activation energy $\Delta\Pi$ calculated from different dislocation models as fitted to the function $\Delta\Pi = A\left(1-\tau_{appl}/\tau_{th}\right)^n$ where n and A are fitting parameters, τ_{appl} is the applied resolved shear stress, and τ_{th} is the theoretical strength of the material.

Dislocation Model	A/Gb^3	n	Remarks
Volterra model [17]	5	2.8	Cutoff radius, $r_0 = 0.5b$
	5	2.3	Cutoff radius, $r_0 = 0.91b$
			Theoretical stress, $\tau_{th} = \frac{Gb}{\pi e^2 r_0}\left(\frac{2-\nu}{1-\nu}\right)$
Peierls model [67,77,80]	5	1.5	Frenkel-sinusoid-type γ surface [67,80]
	15	2.5	γ surface for closed-packed surface in FCC crystals; partial dislocation nucleation [77]
Molecular simulations [71]	4.44	4.2	Heterogeneous dislocation nucleation

.

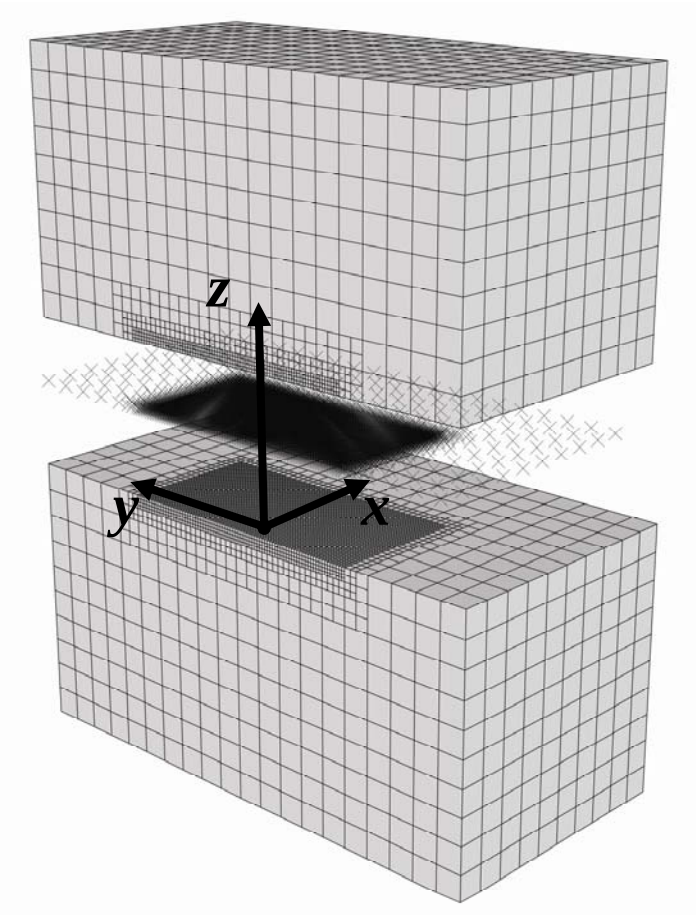

Figure 3.1 The three-dimensional finite element model for the study of homogeneous dislocation nucleation under pure shear stress. A half model is used because of symmetry about the *x*-*z* plane.

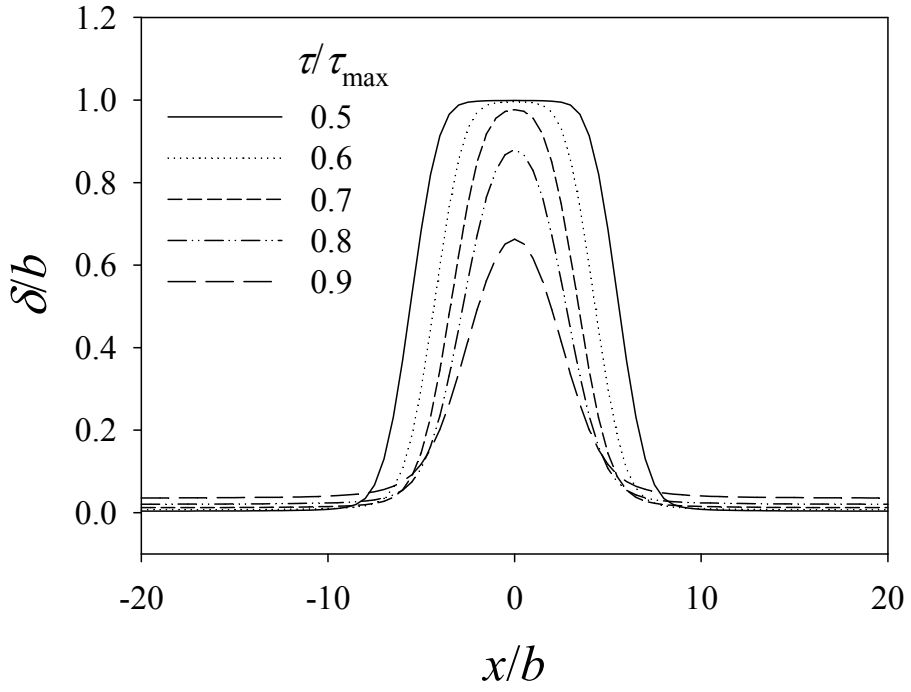

(a)

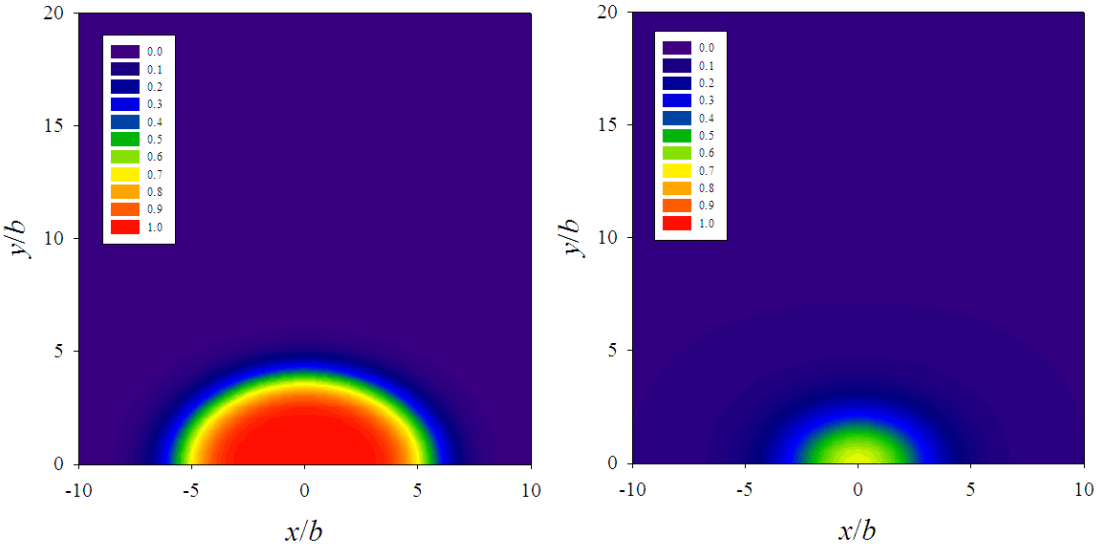

(b) $\tau_{appl} / \tau_{\max} = 0.5$ (c) $\tau_{appl} / \tau_{\max} = 0.9$

Figure 3.2 (a) The saddle point solution of the relative slip distribution, δ_x, along the *x*-direction on the slip plane at $y = 0$ with respect to various pure shear stress values. (b) The saddle point solution of δ_x on slip plane at stress level $\tau_{appl} / \tau_{\max} = 0.5$. (c) The saddle point solution of δ_x on slip plane at stress level $\tau_{appl} / \tau_{\max} = 0.9$.

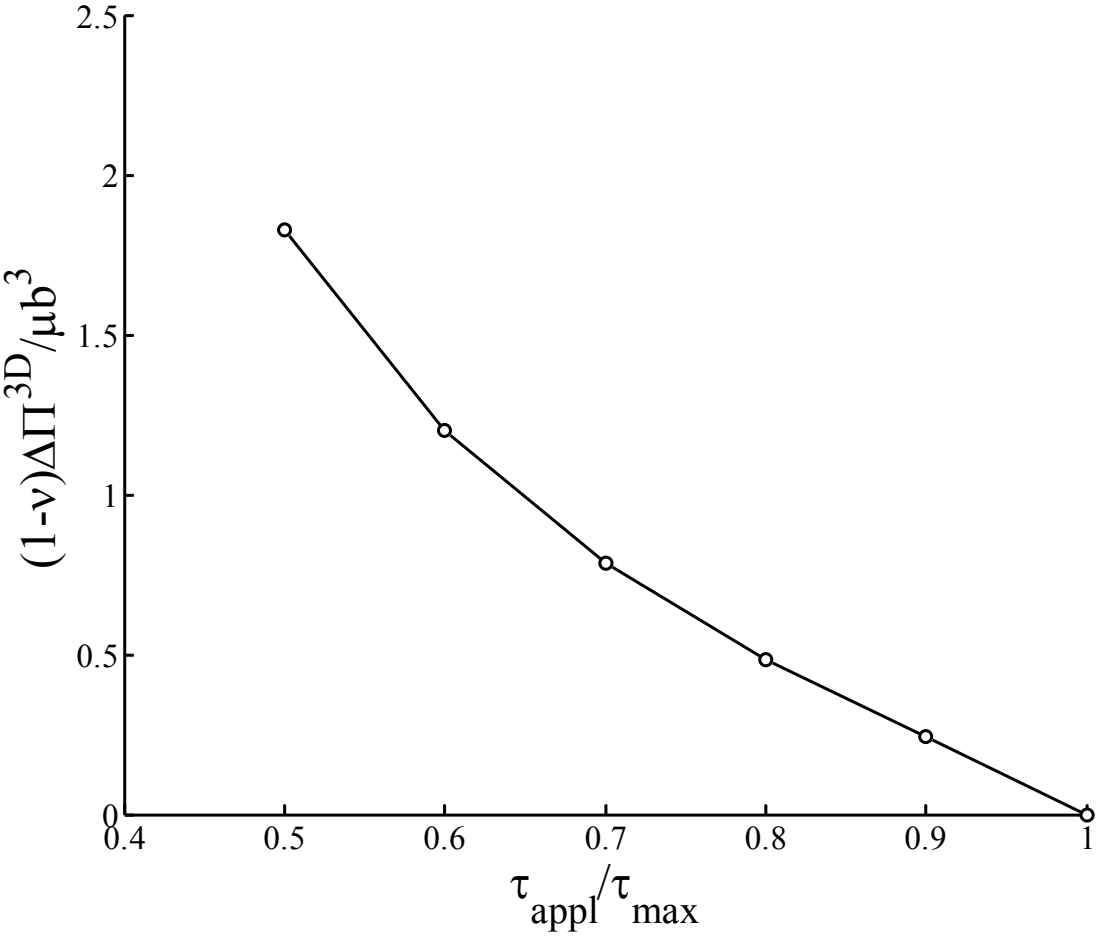

Figure 3.3 The activation energy for homogeneous dislocation nucleation, $\Delta\Pi^{3D}$, normalized by $\mu b^3/(1-\nu)$, as a function of various applied pure-shear stress levels.

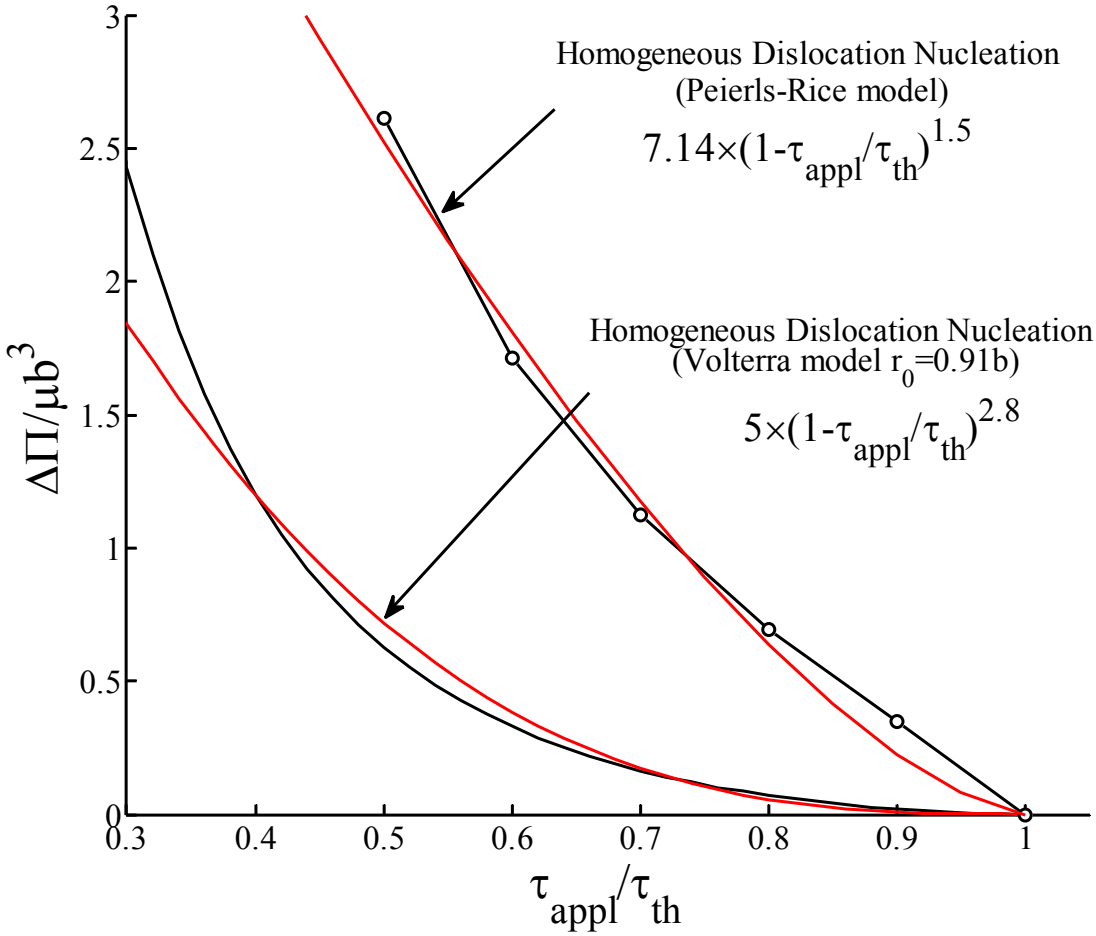

Figure 3.4 The activation energy of homogeneous dislocation is calculated using the Volterra dislocation analysis and the Rice-Peierls dislocation model. It is generally found that the activation energy can be fitted to the function $\Delta\Pi = A\left(1-\tau_{appl}/\tau_{th}\right)^{n}$ where n and A are fitting parameters, τ_{appl} is the applied resolved shear stress, and τ_{th} is the theoretical strength of the material.

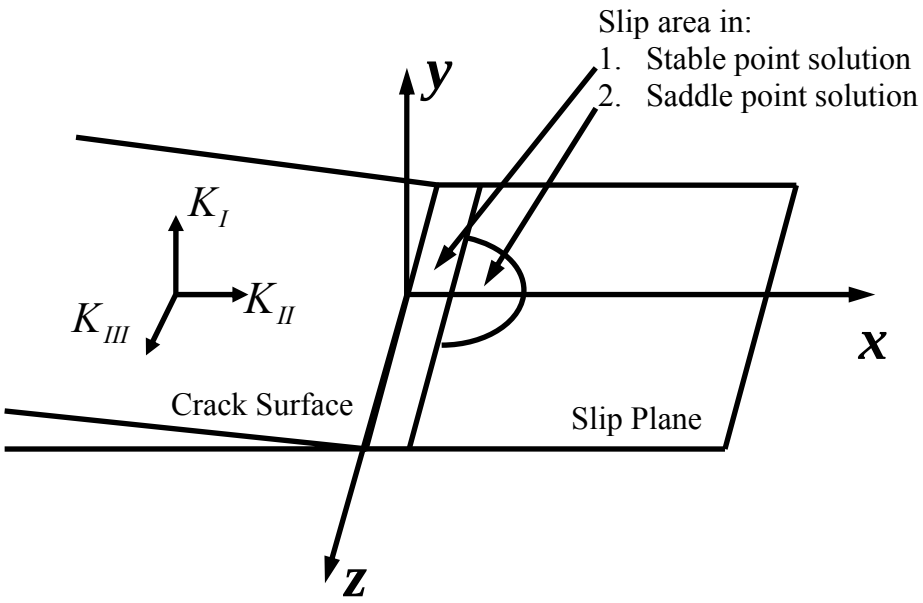

(a)

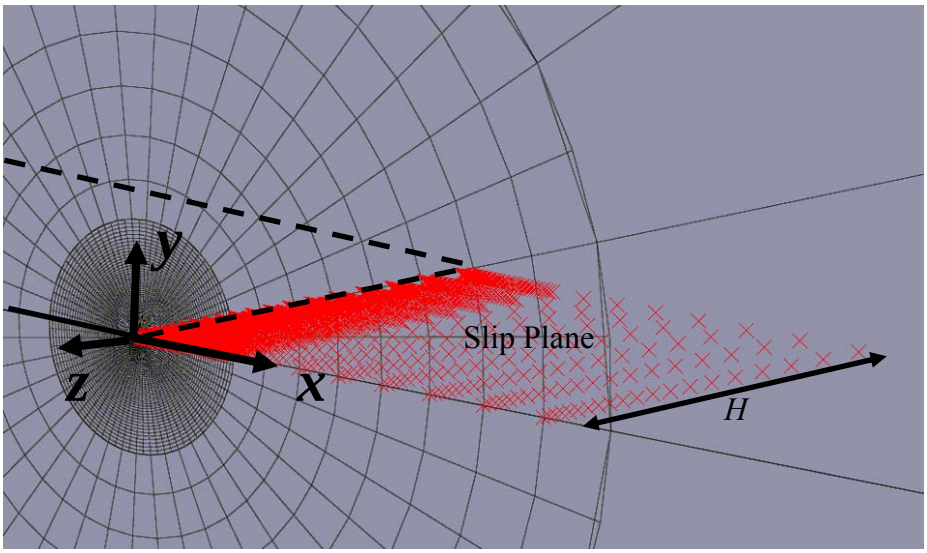

(b)

Figure 3.5 (a) A planar crack under the mixed-mode *k*-field. The relative slip occurs on the *x*-*z* plane, and there is no opening in the normal direction of the slip plane. (b) Dislocation nucleation from the planar crack tip under mode II load. On the slip plane, the opening in *y* direction is prohibited, and the relationship between the shear stress and the relative slip on the *x*-*z* plane is defined in Eq. (3.6).

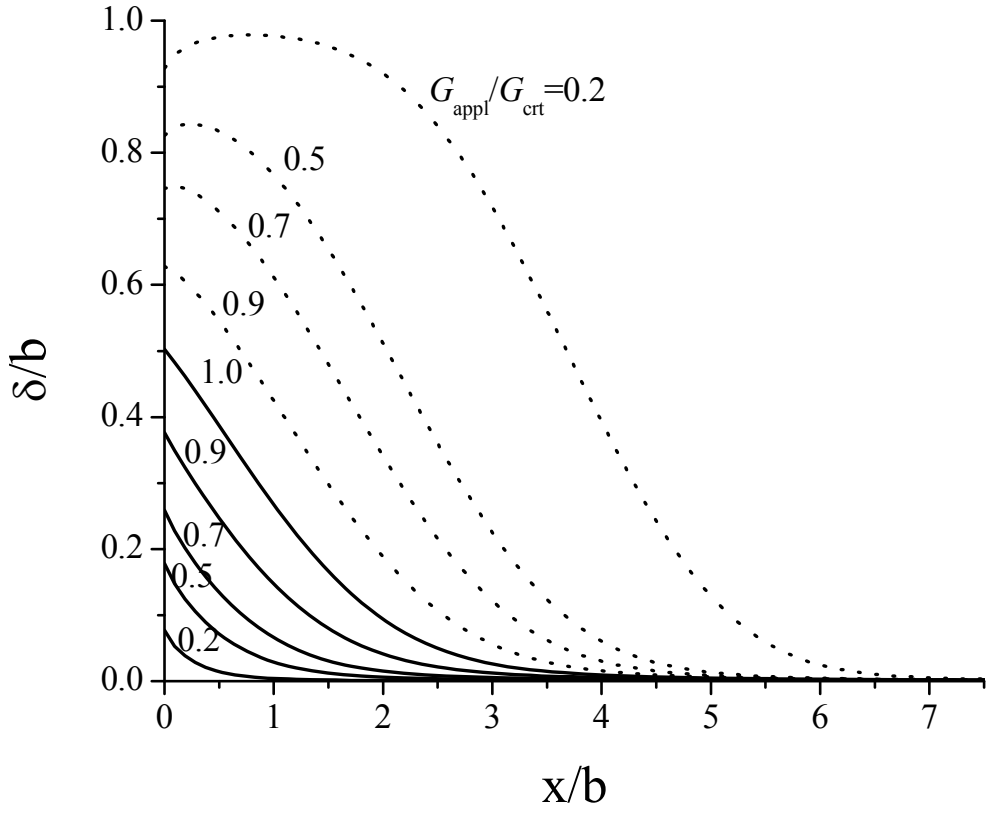

Figure 3.6 The relative slip field on the slip plane under various levels of applied energy release rate, G_{appl}. Solid lines are stationary point solutions and dashed lines are saddle point solutions.

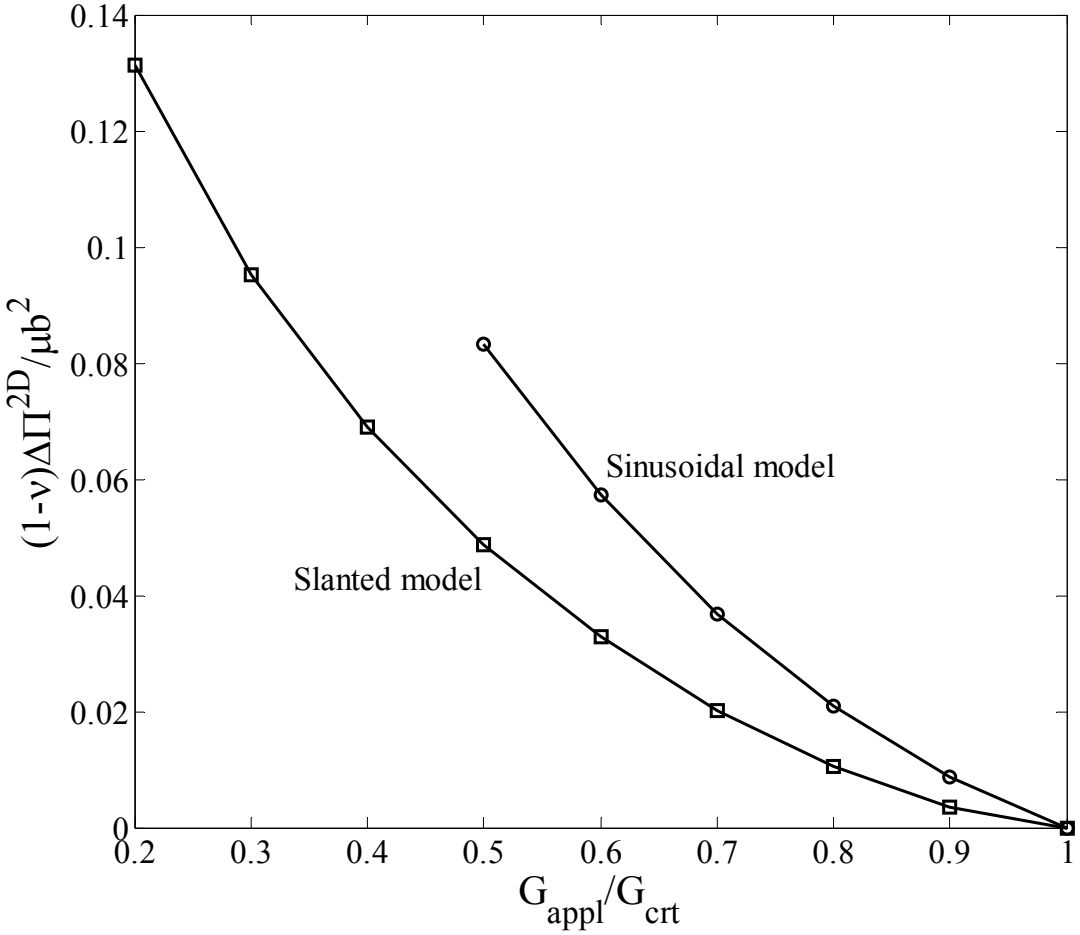

Figure 3.7 Activation energy $\Delta\Pi^{2D}$ per unit length obtained from the Rice-Peierls model using the slanted and simple sinusoidal models

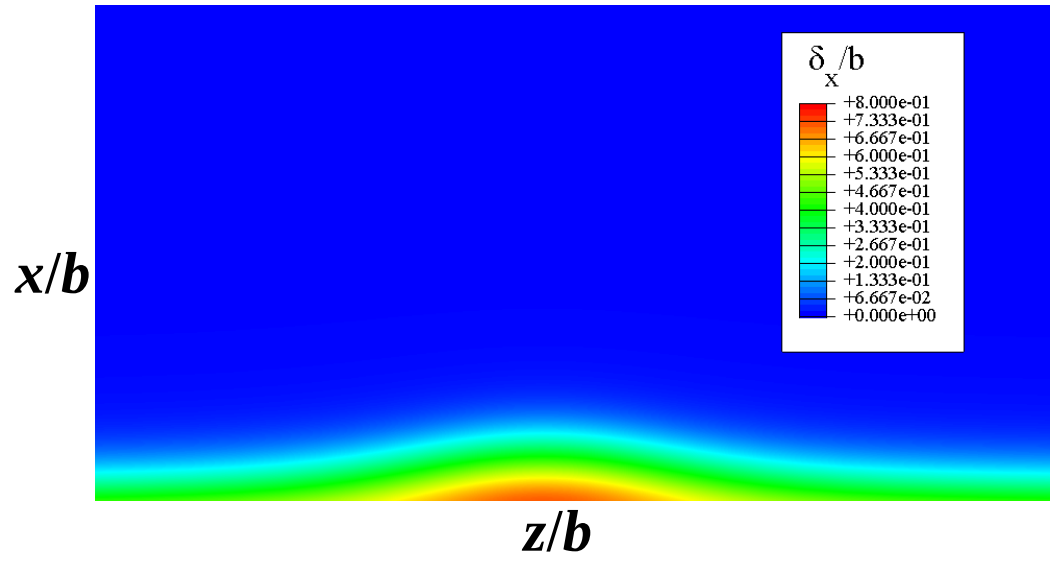

(a)

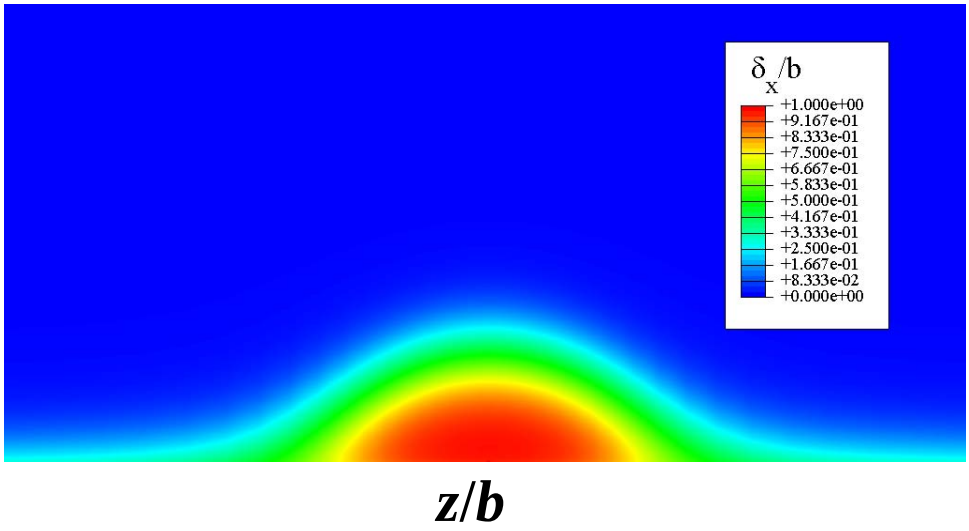

(b)

Figure 3.8 The dislocation loop from the planar crack tip is visualized by the relative slip field with two representative applied energy release rate: (a) $G_{appl} / G_{crt} = 0.9$ (b) $G_{appl} / G_{crt} = 0.7$.

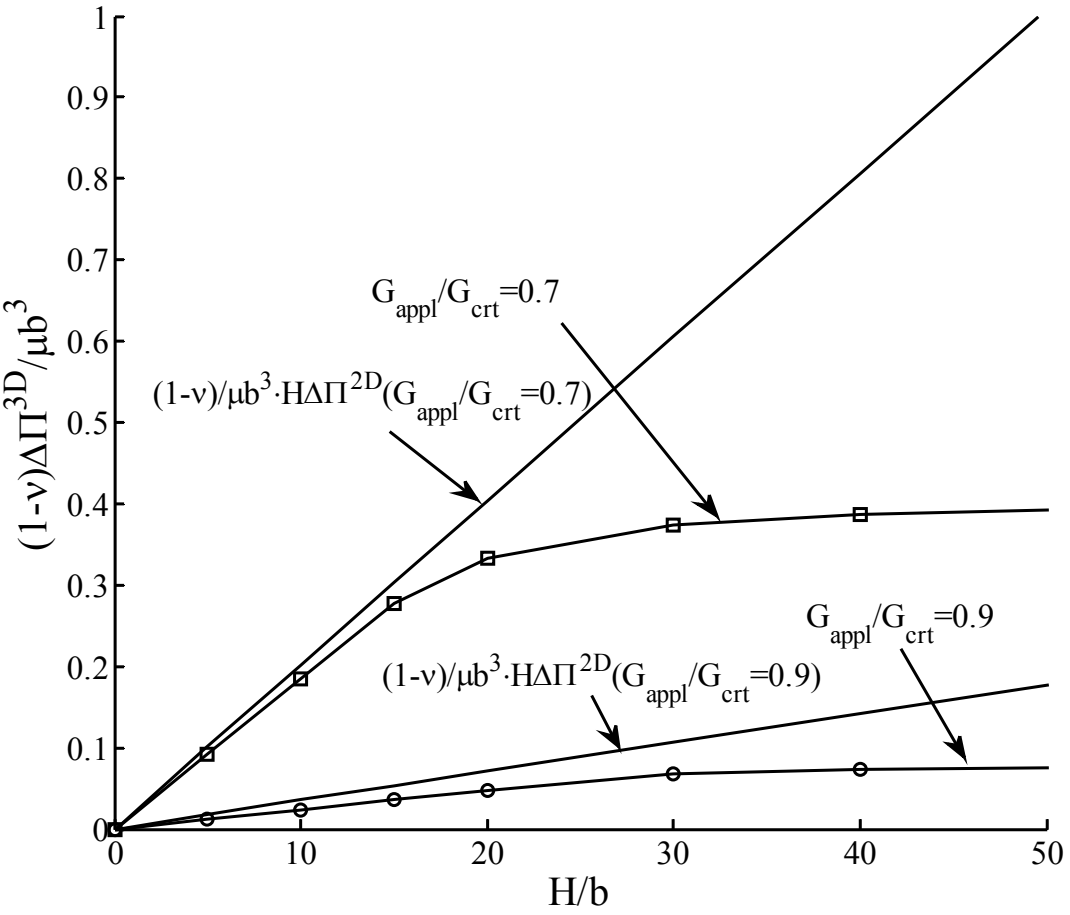

Figure 3.9 The activation energy $\Delta\Pi^{3D}$ normalized by $\frac{\mu b^3}{1-\nu}$ under applied stress levels $G_{applied}/G_{crt}=0.9$ (i.e. circle marked solid line) and $G_{applied}/G_{crt}=0.7$ (i.e. square marked solid line) as a function of the normalized *H/b*. The product of $\Delta\Pi^{2D}$ and thickness H normalized by $\frac{\mu b^3}{1-\nu}$ is also shown as a comparison.

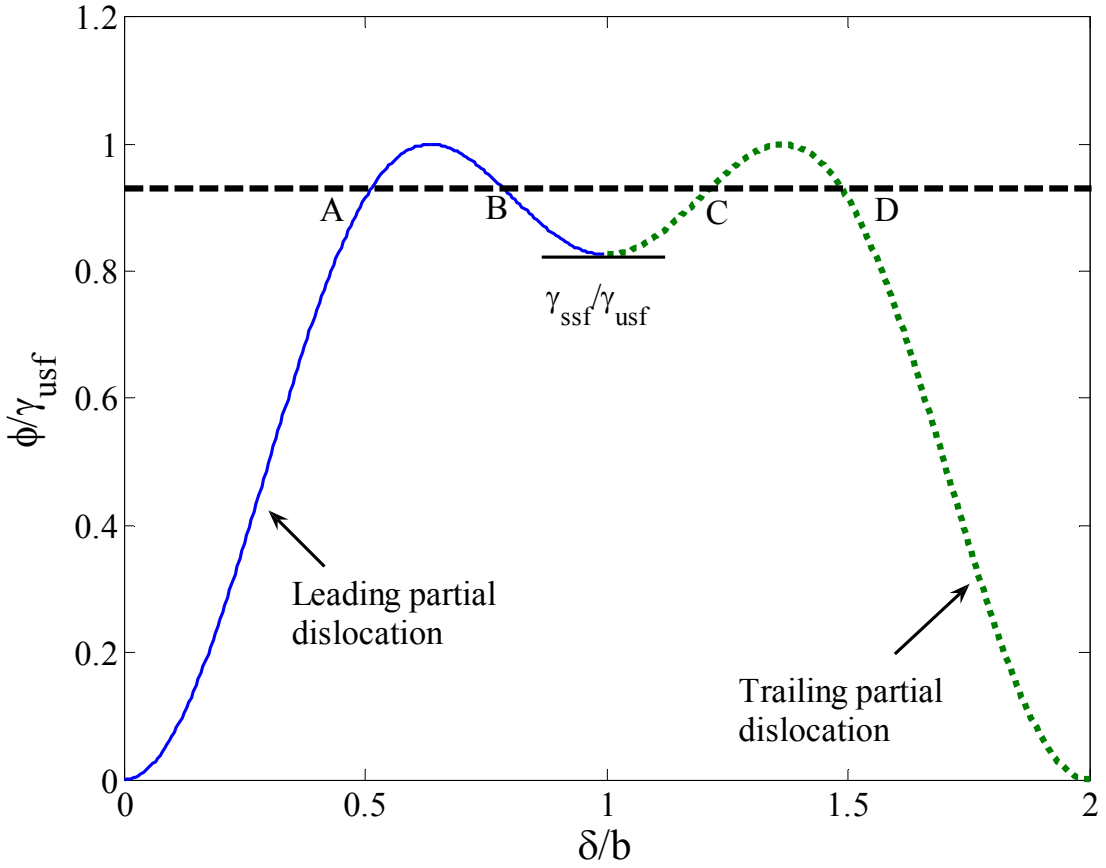

Figure 3.10 The γ potential on the slip plane for the leading-to-trailing partial dislocations as a function of relative slip along the slip direction.

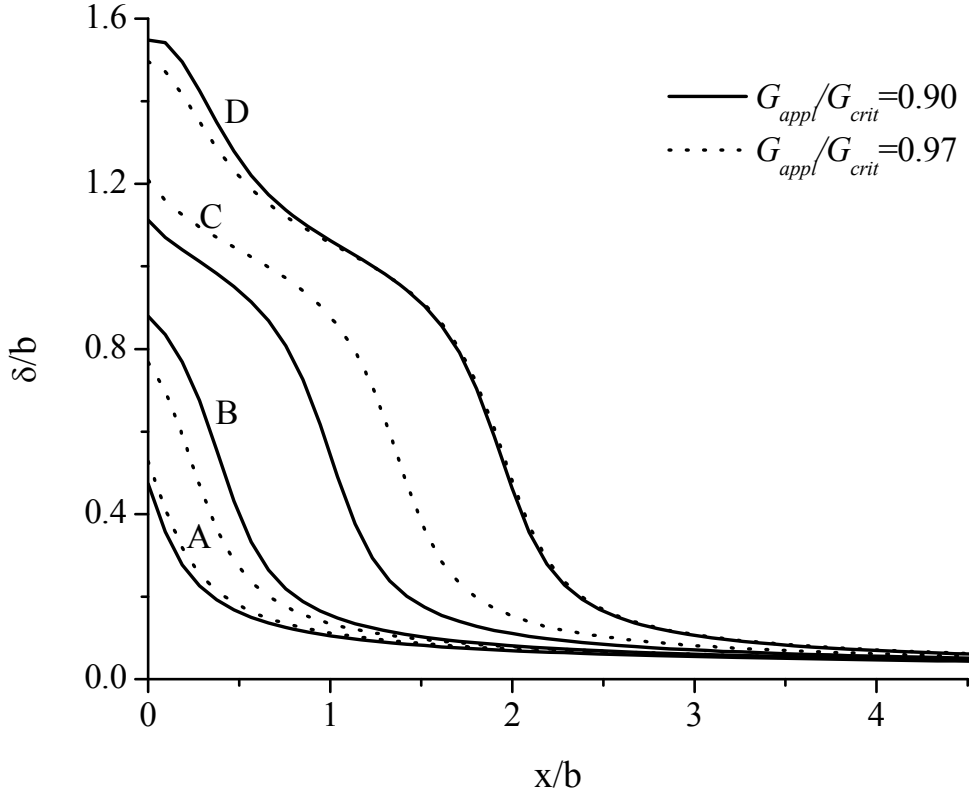

Figure 3.11 The relative slip fields on the slip plane for various load levels corresponding to points A, B, C and D in Fig. 3.10.

Chapter IV

Geometric Effects on Dislocation Nucleation

4.1 Introduction

In this chapter, we will use the nonlinear finite element method developed in Chapter III to study geometric effects on dislocation nucleation. For example, people have observed dramatic strength differences between homogeneous dislocation nucleation and dislocation nucleation from material surfaces [88]. Atomistic simulations also confirm that the force needed to break atomic bond near the surface is less than the force needed to break atomic bond insider the solids [90]. Dislocation nucleation from step corners is also important to microelectronic devices. Because in microelectronic devices, stresses arising from mismatches in lattice constants or thermal expansion coefficients or from processing and thin film growth may lead to failure by fracture, mass transfer, and/or configuration change [25,81]. On the other hand, integrated electronic structures may be deliberately strained to enhance the mobility of charge carriers and thus their functional performance [82, 83]. Stress concentrations near sharp geometric features such as edges and corners may lead to the nucleation of dislocations, which can act as electrical leakage paths and eventually lead to failure of the devices [22, 23, 24]. Mask-edge defects have been observed to form during processing steps such as the solid-phase epitaxy regrowth of amorphous silicon[84-90]. Consequently, the development of immortal, strained nano-electronics requires a knowledge of the defect nucleation process and its dependence on the layout structure, materials processing, and surface treatment, among many others. This paper elucidates the role of film geometric parameters on the critical external stress for dislocation nucleation near the film edge.

4.2 Dislocation Nucleation from Surface Edges

In the model problem (Fig. 4.1), we consider a stress-free silicon nitride (Si_3N_4) pad of size $L \times W \times h$ on an infinite silicon (Si) substrate. We choose a simple slip system with slip direction $\mathbf{s} = (\cos\psi, 0, -\sin\psi)$ and slip normal $\mathbf{m} = (\sin\psi, 0, \cos\psi)$ with $\psi = \tan^{-1}(\sqrt{2})$. When the external stress σ_{xx}^{appl} (applied only on the substrate) reaches a critical value

(denoted as σ_{crt}), a dislocation loop is nucleated from the edge/corner of the Si_3N_4 pad. Dimensional analysis gives

$$\frac{\sigma_{crt}}{\tau_{\max}} = \Pi\left(\frac{\tau_{\max}}{\mu}, \alpha, \beta, \mathbf{s}, \mathbf{m}, \frac{h}{b}, \frac{L}{h}, \frac{L}{W}\right), \tag{4.1}$$

where $\tau_{\max}$ and b are the theoretical strength and the Burgers vector of the silicon substrate, respectively. Two Dundurs parameters, $\alpha = \frac{\mu(1-\nu_p)-\mu_p(1-\nu)}{\mu(1-\nu_p)+\mu_p(1-\nu)}$, $\beta = \frac{\mu(1-2\nu_p)-\mu_p(1-2\nu)}{2\left[\mu(1-\nu_p)+\mu_p(1-\nu)\right]}$, describe the modulus mismatch, where μ and ν are the shear modulus and Poisson's ratio of the substrate, and μ_p and ν_p are those of the pad [22,23, 40]. It should be noted that our model problem may not be representative of some realistic situations. For example, the pad or mask may be stressed, or the entire pad/substrate is covered by a film with different lattice constant, or the pad/substrate is stressed during the solid-phase epitaxial recrystallization of amorphous silicon that is previously created by ion implantation[84-90]. Nevertheless, as will be shown shortly, the difference between our model problem and some other experimental setups is merely on the stress intensity factors (SIFs) which characterize the near-edge stress fields.

When $L/W \to 0$, the pad becomes infinite in the y direction. As previously analyzed by Suo et al. [22,23]. the elastic stress field near the root of the edge is singular,

$$\sigma_{ij}(r,\theta) = \frac{k_1}{(2\pi r)^{\lambda_1}}\Sigma_{ij}^1(\theta) + \frac{k_2}{(2\pi r)^{\lambda_2}}\Sigma_{ij}^2(\theta), \tag{4.2}$$

where $r = \sqrt{x^2+z^2}$ and $\theta = \tan^{-1}(x/z)$. The eigenvalues λ_α and eigenfunctions Σ_{ij}^α are determined by the Dundurs parameters and the dihedral angle at the edge root. The SIFs, k_α, can be calculated from the applied stress and geometric parameters. Thus the dislocation would be nucleated if the stress intensity factor reaches a critical value, which is similar to Griffith-Irwin fracture mechanics [91], and is essentially equivalent to the Rice-Thomson criterion [46, 47, 92, 93,94]. The SIF analysis does not provide an explicit treatment of the dislocation nucleation process, so that the relationship between the critical SIF and the mode mixity cannot be determined. It is also difficult to determine the three-dimensional asymptotic stress fields near the rectangular pad.

An explicit description of the dislocation nucleation process has been given in Chapter III. Here, a simple sinusoidal form is used for the interplanar potential. The interface shear stress, τ_s, is related to the shear separation, Δ_s, in the slip direction by

$$\frac{\tau_s}{\tau_{\max}} = \sin\left(2\pi\frac{\Delta_s}{b}\right) + \zeta\frac{d}{dt}\left(\frac{\Delta_s}{b}\right). \tag{4.3}$$

We use the same treatment in Chapter III to implement Eq. (4.3) to the slip plane. Because the interplanar potential is periodic, dislocation nucleation corresponds to an elastic snap-back instability that occurs after the total potential energy reaches an unstable equilibrium. The stiffness matrix becomes singular at the point of instability. The post-instability behavior can be accurately captured by the introduction of the fictitious viscosity, ζ, in Eq. (4.3) [95]. This methodology has also been used to coating delamination and indentation cracking problems [96,97].

Because of symmetry in x and y directions, only a quarter space in Fig. 4.1 must be meshed. The minimum mesh size near the edges and corners is chosen to be less than 1/3 of the dislocation core size. The theoretical stress $\tau_{\max}$ is about 1/5~1/30 of the shear modulus [17]. Its actual value is of no particular interest here, since our results are presented in normalized forms. We take the shear modulus and Poisson's ratio of Si_3N_4 to be 54.3 GPa and 0.27 and those of silicon to be 68.1 GPa and 0.22, respectively [23,83]. A more quantitative calculation should use anisotropic elastic constants of these materials[98] and an interplanar potential based on ab initio results [99], but our conclusions here should remain qualitatively unchanged. For finite element simulations with ζ =0, the eigenvalues of the stiffness matrix are monitored so that the onset of dislocation nucleation can be correctly determined. In Fig. 4.2, the normalized critical stress, $\sigma_{crt}/\tau_{\max}$, is plotted as a function of geometric parameters, L/h and L/W, with two representative values of $h\tau_{\max}/\mu b$. This particular combination of parameters ($h\tau_{\max}/\mu b$) is chosen to compare a characteristic geometric length in the problem, h, to the dislocation core size, $\sim \mu b/\tau_{\max}$ [95]. Similar combinations can be found in many other cohesive interface models [100]. From Fig. 4.2, we observe that, first, as $h\tau_{\max}/\mu b$ increases, the dislocation nucleation process zone becomes small when compared to the pad height; the limit at $h\tau_{\max}/\mu b \to \infty$ is equivalent to the SIF analysis [23, 83]. For a small $h\tau_{\max}/\mu b$ (as compared to unity), σ_{crt} will approach the theoretical strength. Second, σ_{crt} increases with a decrease of L/h because the stress concentration at the edge will be reduced as the two side surfaces that are parallel to *y-z* plane move together. Clearly, σ_{crt} will approach a plateau as $L/h \to \infty$ since the two side surfaces will not feel the presence of each other. Third, σ_{crt} increases with an increase of L/W for a

similar reason. This three-dimensional effect is, however, not significant since the results in Fig. 4.2 show that an increase of L/W from 1 to 20 merely leads to about 10-20% increase of σ_{crt}.

Recently, Kammler *et al.* [24] patterned two square Si_3N_4 pads on a silicon substrate with $h = 500nm$ and lateral sizes of 10μm and 1μm, respectively. When subjected to a residual stress, the large pad exhibited dislocation nucleation, while the small pad did not, implying that a "blanket-like" pad is more susceptible to dislocation nucleation than a "pole-like" pad. This observation agrees with our analysis in Fig. 4.2, which suggests that σ_{crt} for the large pad should be about a half of that for the small pad.

In the results shown in Fig. 4.3, the dislocation loop is visualized by the concentration of the resolved shear stress (RSS), $\sigma_{ij}s_i m_j$, as normalized by $\sigma_{xx}^{appl} s_x m_x$. These results are made available by using the viscous model in Eq. (4.3). We choose the viscosity $\zeta\tau_{\max}/\dot{\sigma}_{xx}^{appl}$ =0.0014, and other parameters are L/h =10, L/W =1, h/b =20, and $\tau_{\max}/\mu$ =0.21. As shown by the snapshot in Fig. 4.3(a), the first dislocation is nucleated at the corner of the Si_3N_4 pad where the elastic RSS maximizes. Subsequently, a second dislocation is nucleated at the center of the edge, as shown in Fig. 4.3(b). The shift of nucleation site is due to the back stress generated by the first dislocation, which modifies the stress fields along the edge line. Dislocation shapes are similar to the transmission electron microscope images by Kammler *et al* [24]. The first dislocation nucleation can also conceivably occur at the edge center because (i) dislocation nucleation is a thermally activated process, (ii) the RSS near the corner and that near the edge center do not differ significantly, and (iii) corners are usually rounded. Finally, note that the nucleated dislocations do not travel too far from the edge because the stress concentration is localized only near the pad. This is particularly true for materials with high lattice resistance.

4.3 Discussions on Geometric Effects

The dislocation nucleation process near sharp features in strained electronics has been investigated by a dissipative cohesive interface approach. The critical stress decreases with an increase of $h\tau_{\max}/\mu b$ or L/h, or with a decrease of L/W. As multiple dislocations inject into the substrate, the dislocation nucleation site shifts from the corner to the center of the edge.

Geometric effects on dislocation nucleation can also explain the observation in recent experiment [17]. The critical resolved shear stress for dislocation nucleation is found to be $\mu/8$ for both Mo-3Nb and Mo-10Al-4Ni single crystals under nanoindentation, while compression tests on Mo-10Al-4Ni micropillars reveal a critical shear stress of $\mu/26$. The stress required for half or quarter heterogeneous dislocation nucleation at the free surface and edges of micropillars is expected to be lower than the stress needed to homogeneously nucleate a full dislocation loop inside the bulk during nanoindentation. It can be seen from Table 3.1 that the heterogeneous dislocation nucleation has lower activation energy than the homogeneous dislocation nucleation at the same load level. Therefore, during micropillar compression test, where the stress fields are uniform in the solid, the heterogeneous dislocation is easier to be thermally activated than the homogeneous dislocation nucleation. This may be responsible for the difference in the critical resolved shear stress between nanoindentation test and micropillar compression test.

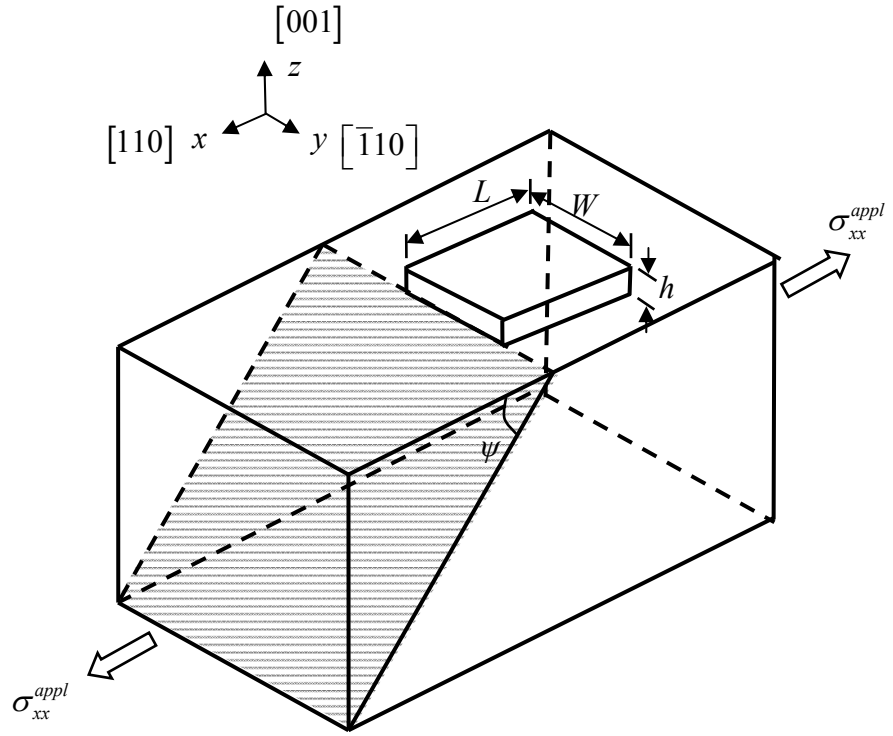

Figure 4.1 Schematic illustration of a rectangular silicon nitride pad with length L, width W, and height h on an infinite silicon substrate. The slip plane (shaded) makes an angle ψ from the *x*-*y* plane, and the slip direction is taken to be $(\cos\psi, 0, -\sin\psi)$.

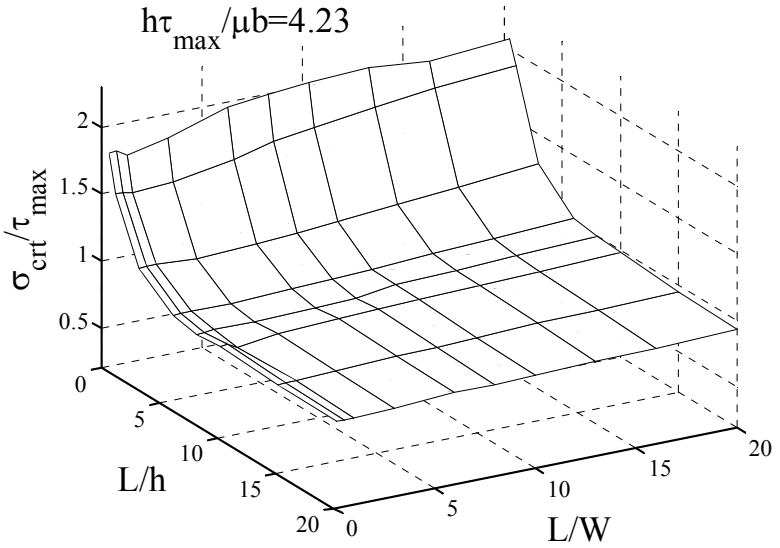

(a)

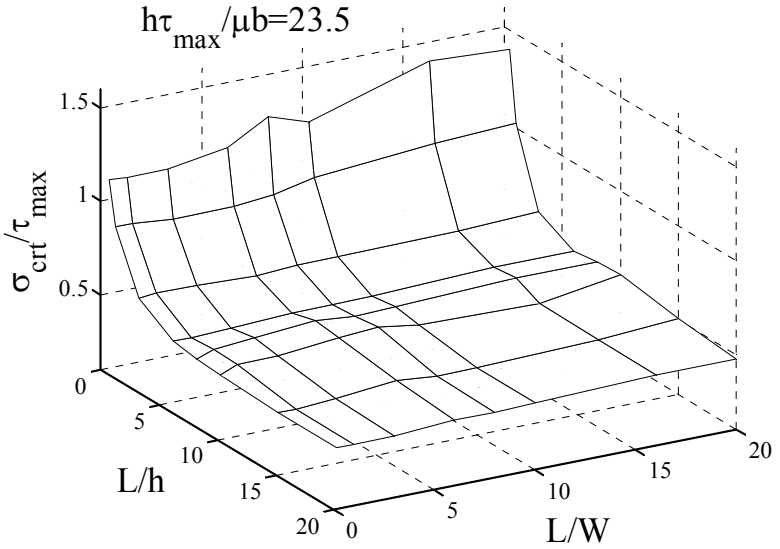

(b)

Figure 4.2 The critical stress for dislocation nucleation σ_{crt} (as normalized by the theoretical strength $\tau_{\max}$) plotted against two geometric parameters, L/h and L/W, with $h\tau_{\max}/\mu b$=4.23 in (a) and 23.5 in (b).

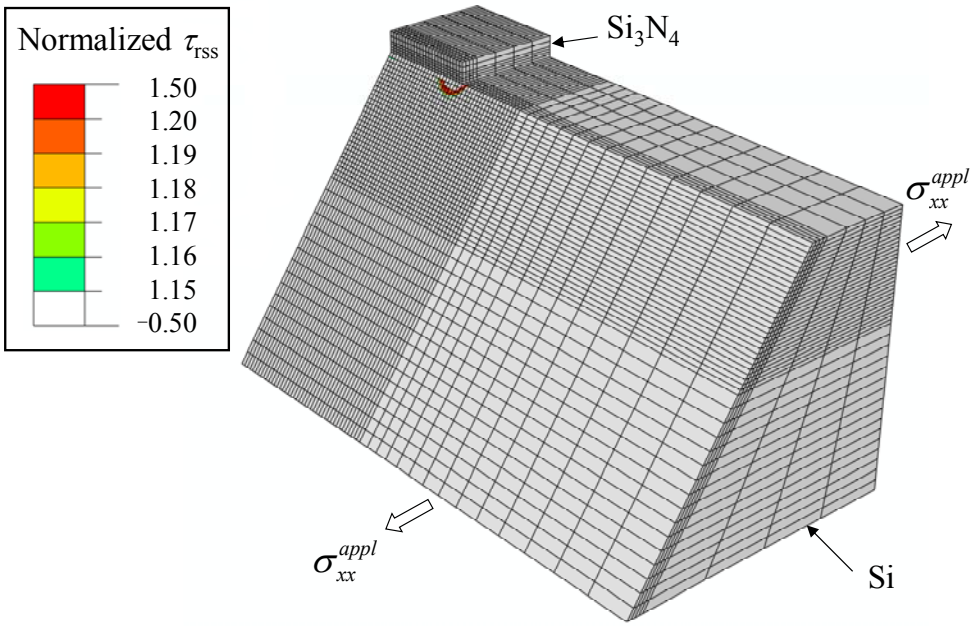

(a)

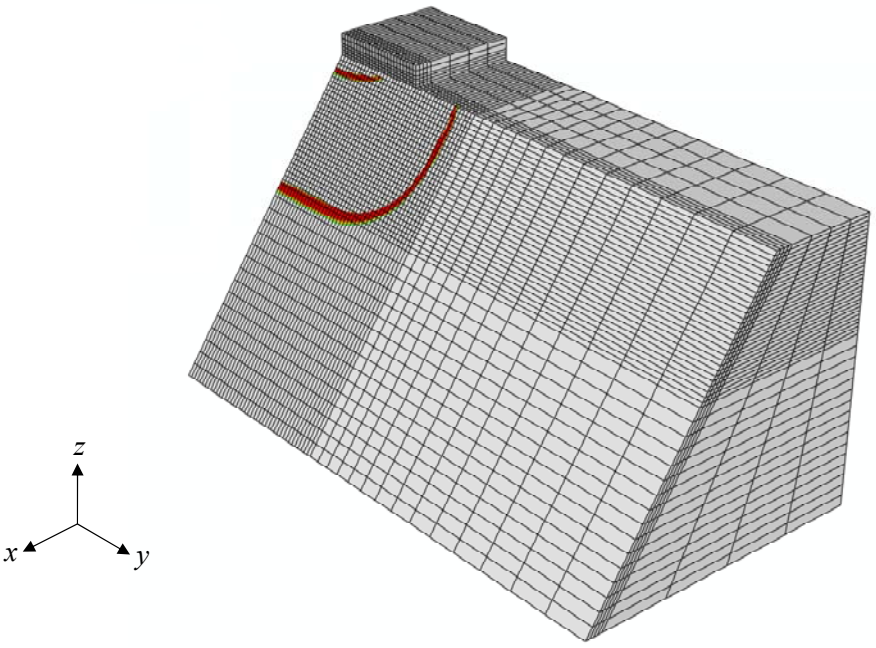

(b)

Figure 4.3 Representative results showing the first dislocation nucleation from the corner in (a), and subsequently the second dislocation nucleation from the center of the edge in (b). The resolved shear stress (RSS) contours are plotted on the slip plane.

Chapter V

Indentation Schmid Factor and Orientation Dependence of Nanoindentation Pop-In Behavior of NiAl Single Crystals

5.1 Introduction

Instrumented nanoindentation techniques, which provide accurate measurements of the indentation load, *P*, and the indenter penetration depth, *h*, at nanometer resolution, have been widely used to characterize small scale mechanical behavior [1-3]. Methodologies have been established on how to extract material properties such as modulus and hardness from the measured *P*~*h* curves. Besides the measurement of the hardness and modulus, the *P*~*h* curves can be used to examine the onset of elastic-plastic transition in various crystalline and amorphous materials [4-17]. The onset of plasticity is often associated with a displacement discontinuity on the otherwise continuous load-displacement curve, or denoted as "pop-in", as the indenter tip suddenly jumps into the specimen with negligible load increase. While the pop-in event may be associated with fracture of surface oxide layer for some materials [18], it is believed that for a defect-free crystalline material, the first displacement burst is a result of homogeneous dislocation nucleation underneath the indenter [6,7,9-17,19-21]. This conclusion is supported by the following observations. *First*, the load-displacement curve before pop-in occurs is fully reversible, and can be fit to the Hertzian contact theory,

$$P = \frac{4}{3} E_r \sqrt{Rh^3}\ , \tag{5.1}$$

where R is the indenter tip radius and E_r is the reduced indentation modulus. Thus the deformation is purely elastic prior to the pop-in event. *Second*, after unloading before the first strain burst, the Atomic Force Microscope image shows no measurable permanent shape change on the specimen surface, while a residual shape change occurs if unloading is started after pop-in occurs [6,9]. *Third*, when the first pop-in event occurs, the maximum shear stress in the specimen is in the range of *G*/30~*G*/5 with shear modulus *G* for a variety of materials, and is very close to the theoretical strength calculated by *ab initio* method [99]. *Fourth*, pop-in loads vary in a wide range, and the statistical measurements confirm the dependence on indentation strain rate and environmental temperature. Theoretical predictions based on the

stress-assisted, thermally-activated, homogeneous-dislocation-nucleation model agree well with these statistical measurements [7-10,14,17]. Consequently, nanoindentation pop-in tests can be used as a powerful tool to study the homogeneous dislocation nucleation.

Most of previous theoretical studies assume that the homogeneous dislocation nucleation occurs when the resolved shear stress reaches the theoretical strength, which is similar to the Schmid law that describes the plastic flow in single crystals. At atomic length scales, stress components other than the resolved shear stress will also affect the dislocation nucleation process [101,102]. For uniaxial loading conditions, Tschopp *et al* [101,102] conducted extensive molecular simulations on copper single crystals and concluded that for loading directions close to <101> (or equivalently, at lower right regime on the standard <001> triangle on the inverse pole figure), the compressive stress on the slip plane dominates the dislocation nucleation process, while the Schmid law generally works well for loading directions at upper left regime in the standard <001> triangle. On the other hand, the indentation stress fields are far more complex than uniaxial tests, and the ratio of compression to shear stress on a given slip system depends on crystallography and elastic anisotropy. As another comparison, the single-slip-system dislocation nucleation can be realized in single crystals under uniaxial tension with loading directions lying in the standard <001> triangle. However, it remains unclear if the same orientation under indentation will be still leading to dislocation nucleation on a single slip system.

In this study, the load required for homogeneous dislocations nucleation in nanoindentation test on single crystals is investigated as a function of crystallographic orientation and elastic anisotropy. By adopting indentation Schmid factor derived in Chapter II and assuming that dislocation nucleates when maximum resolved shear stress reaches the theoretical strength, the pop-in load is predicted to be a function of indenter radius, effective indentation modulus, indentation Schmid factor, and the theoretical strength. Comparisons to experimental measurements will test the validity of the above relationship and fit the theoretical strength of the specimen. By systematically varying the indentation direction, we can investigate the pressure effects as well as the possibility of simultaneously activating dislocation nucleation on multiple slip systems. NiAl single crystals are chosen, because the slip systems $\{110\}\langle 001\rangle$ in this B2 structure are simpler than other crystal structures so that we will not encounter complex dislocation behavior such as partial dislocation nucleation.

The homogeneous dislocation nucleation process is a stress-assisted, thermally activated process, so that statistical measurements with respect to different indentation directions can

be used to further validate which stress components are playing key roles in nucleation process, if the pop-in corresponds to homogeneous dislocation nucleation, and whether single- versus multiple-slip-system dislocation nucleation really occurs.

5.2 Experiment

Single crystal NiAl sample was grown in an optical floating zone furnace, which is used previously to grow other intermetallic single crystals or eutectic composites [103]. Briefly, 99.99 % pure Ni and Al metal pieces were arc melted to produce buttons, which were flipped and remelted five times to ensure homogenization before drop casting into a copper mold and ultimately producing an alloy with a composition of 50at % Ni - 50 at% Al. These drop-cast ingots (10 mm in diameter and 120 mm in length) were then used as feed rods for single crystal growth in the optical floating zone furnace. During growth of the first crystal, the diameter of the molten zone was carefully reduced to produce a neck that prevented the slower growing grains from propagating. This technique produced a single crystal with a growth direction near [100] as determined by Laue back scattered X-ray diffraction. Specimens with different crystallographic orientation were cut from this single crystal. Before performing nanoindentation, the specimen was mounted in epoxy, ground and polished using standard metallographic procedures. The final polishing was performed in a water solution with colloidal silica suspension.

Nanoindentation was conducted with a MTS XP nanoindenter using a 90° conical diamond indenter with a spherical tip at the end whose radius was ~580 nm. All tests were performed in the continuous stiffness mode with a constant rate of $\dot{P}/P = 0.05s^{-1}$. About 100 indents were made in each specimen, and the indents were placed far enough apart to avoid interference. As shown in Fig. 5.1(a), clear pop-ins were observed for all the tests, and the loads corresponding to the first pop-in were recorded as the pop-in loads, P_{pop-in}. The tested indentation directions are shown by the open markers in the standard [001] triangle in Fig. 5.1(b). Four lines are denoted in Fig. 5.1(b) with parameter *m* varying from 0 to 1.

5.3 Nanoindentation pop-in load for homogeneous dislocation nucleation

We assume that the homogeneous dislocation nucleation occurs when the maximum resolved shear stress reached the theoretical strength τ_{th} of the material, i.e., $\tau_{rss}^{\max} = \tau_{th}$. The

stress fields of elastically anisotropic solids under indentation and the indentation Schmid factor are already given in Chapter II. Using Eqs. (2.18) and (2.24) gives the predicted pop-in load under Hertzian contact,

$$P_{crt} = \left(\frac{\tau_{th}}{S}\right)^3 \frac{\pi^3 R^2}{6E_r^2}. \tag{5.2}$$

The reduced modulus E_r is given by Chapter II, and because our analysis is on single crystals, it has the form,

$$E_r = \left[\frac{1}{E_{eff}} + \frac{\left(1-\nu_i^2\right)}{E_i}\right]^{-1} \tag{5.3}$$

where the effective indentation modulus E_{eff} is given by Eq. (2.25), and depends on elastic anisotropy and indentation direction.

Contours of the predicted P_{crt} for NiAl single crystals under Hertzian contact are plotted in Fig. 5.3. As we move from $[001]$ to $[111]$, the effective modulus E_{eff} increases by about 16%, and the indentation Schmid factor increases by about 35%. Consequently, the predicted pop-in load will be $P_{crt}^{001} : P_{crt}^{101} : P_{crt}^{111} \approx 1 : \frac{1}{2} : \frac{1}{3}$. Such a significant variation is ideal for experimental validation.

To examine more closely the crystallographic dependence of the pop-in load, we now define an effective Schmid factor by

$$S_{eff} = \frac{1}{p_0} \max_{(\alpha)} \left\{ \left| \sigma_{ij} s_i^{*(\alpha)} m_j^{*(\alpha)} \right| + k \sigma_{ij} m_i^{*(\alpha)} m_j^{*(\alpha)} \right\}, \tag{5.4}$$

where the second term in the braces is the stress normal to the slip plane, and *k* is the normal-shear coupling coefficient. The pop-in criterion in Eq. (5.2) will be modified by substituting S_{eff} for S. With several representative *k* values, Fig. 5.4 plots S_{eff} for spherical indentation on NiAl with indentation directions along $[mm1]$, $[m\,\frac{m}{2}1]$, and $[m01]$ with *m* varying from 0 to 1. The location that reaches S_{eff} differs slightly from that of S. The small difference between S_{eff} and S arises from the fact that normal stress and resolved shear stress are generally comparable under the Hertzian stress fields.

Prior to the first pop-in, the load-displacement relationship can be fitted to the Hertzian contact solution in Eq. (5.1). The fitted indentation modulus agrees well with our prediction in Fig. 2.4 within 10% deviation for all the indentation directions. For NiAl, the major

contribution to the dependence of P_{crt} on indentation direction arises from S, because the variation of S is larger and the power exponent associated with S in Eq. (5.2) is larger than those of E_r.

The nanoindentation tests were repeated over one hundred times to produce the cumulative probability, f, versus pop-in load, P_{pop-in}, curves in Fig. 5.5(a). Indeed the pop-in load is at maximum for $\langle 001 \rangle$ indentation direction and at minimum for $\langle 111 \rangle$ indentation direction, which agree well with the prediction in Fig. 5.3. The analysis of the entire $f \sim P_{pop-in}$ curves will be conducted from the thermal activation model in the next subsection. Here the measured pop-in loads at 90% and 80% cumulative probability are shown by the open markers in Fig. 5.6 with indentation direction varying along $[mm1]$, $[m\frac{m}{2}1]$, and $[m01]$. As shown in Eq. (5.2), the only unknown parameter is the theoretical strength τ_{th}, which is obtained by fitting the pop-in loads at 90% cumulative probability for all the tested indentation directions (open markers in Fig. 5.1(b)). Using the indentation Schmid factor gives τ_{th}=8.57 GPa, which is about $G/13.5$ with shear modulus on the slip system G=116 GPa. Using the effective indentation Schmid factor with k=0.1 gives τ_{th}=9.56 GPa or $G/12.1$. These values are in the typical range of theoretical strength, i.e., $G/30 \sim G/5$. Comparisons in Fig. 5.6 indicate that the normal-shear coupling does not give significant variation of the fitted theoretical strength, because for any indentation direction, the shear and normal stresses on any slip systems are comparable, so that S and S_{eff} have similar dependence on indentation direction. Consequently, the pressure effects cannot be determined from pop-in tests under the Hertzian contact.

Discrepancies are larger for indentation directions of <001>, <214>, and <207>. Particularly, the slope of $f \sim P_{pop-in}$ for <001> is dubiously smaller than others in Fig. 5.5(a). One may suspect this is due to the possibility of heterogeneous dislocation nucleation, which will be discussed shortly in our thermal activation model. Another possible source of this discrepancy may arise from the tip shape. We use a radius of R=580 nm for all the indentation directions instead of calibrating it for every indentation direction [16]. Nonetheless, in general the Schmid-type dislocation criterion seems to work well for all the indentation direction except for some small deviations for indentation directions near <001> orientation. As a comparison, using molecular simulations to study copper single crystals under uniaxial tension, Tschopp et al. [101,102] found the Schmid-type dislocation criterion

works well for indentation directions close to the [001]-[111] boundary in the standard [001] triangle, but not for those directions close to the [101] vertex.

5.4 Pop-in kinetics and thermally activated dislocation nucleation process

The dislocation nucleation process is a stress-assisted, thermally activated process. When the applied resolved shear stress is lower than but close to the theoretical shear stress, an energy barrier for dislocation nucleation exists. At finite temperatures, this activation energy barrier can be overcome by thermal energy, thus leading to a wide range of pop-in loads as shown in Fig. 5.5. Assuming that the activation energy $\Delta\Pi^{(\alpha)}$ for homogeneous dislocation nucleation is only a function of the resolved shear stress $\tau_{rss}^{(\alpha)}$ on a given slip system, we aim to see whether the dependence of the statistical data in Fig. 5.5 on indentation direction can also be predicted from the analysis based on the indentation Schmid factor.

With a given indentation direction, when the applied load is lower than the athermal limit, the rate of dislocation nucleation on the α-th slip system is assumed to obey the Arrhenium law,

$$\dot{n}^{(\alpha)} = \dot{n}_0 \exp\left[-\frac{\Delta\Pi^{(\alpha)}}{k_B T}\right], \tag{5.5}$$

where $\dot{n}_0$ is an attempt frequency per material volume, k_B is the Boltzmann constant, and T is the absolute temperature. The activation energy for the homogeneous dislocation nucleation can be calculated using the Volterra dislocation analysis, or using the Peierls dislocation model, or by molecular simulations. As summarized in Chapter III, we use the following approximation,

$$\Delta\Pi = A\left(1-\tau_{appl}/\tau_{th}\right)^n, \tag{5.6}$$

where τ_{appl} is the applied shear stress. As in Table 3.1, the power exponent n is found to be about 1.5-4.2 and the normalized pre-factor is $A/Gb^3 \approx 5-15$.

When the indentation direction lies on the vertices and boundaries of the standard triangle, at least two slip systems have the same maximum resolved shear stress. Clearly for those directions close to the triangle boundary, several slip systems may have very close values of the maximum resolved shear stress. Consequently, we need to consider possibilities of dislocation nucleation on all the slip systems. We relate the maximum resolved shear stress

on the α-th slip system to the maximum contact pressure by the indentation Schmid factor of the α-th slip system,

$$S^{(\alpha)} = \frac{1}{p_0} \max \left\{ \sigma_{ij}\left(x_k\right) p_i^{(\alpha)} q_j^{(\alpha)} \right\}. \tag{5.7}$$

Thus we can write down the maximum applied shear stress on the α-th slip system as $\tau_{appl}^{(\alpha)} = \beta^{(\alpha)} P^{1/3}$ with $\beta^{(\alpha)} = S^{(\alpha)} \left(\frac{6E_r^2}{\pi^3 R^2} \right)^{1/3}$.

Denote $q^{(\alpha)}$ as the survivability, i.e., probability of no pop-in, on the α-th slip system. For a first order system, it relates to the nucleation rate by $\dot{n}^{(\alpha)} V = -\dot{q}^{(\alpha)} / q^{(\alpha)}$ where V is the material volume in which dislocation nucleation may occur. Using Eq. (5.5) gives

$$\ln q^{(\alpha)} = -\dot{n}_0 V \int_0^{P_{pop-in}} \exp\left[-\frac{\Delta\Pi^{(\alpha)}\left(\beta^{(\alpha)} P^{1/3}\right)}{k_B T} \right] \frac{dP}{\dot{P}}. \tag{5.8}$$

The cumulative probability for pop-in, f, is now a function of P_{pop-in}, given by

$$\begin{aligned} f &= 1 - \prod_{\alpha} q^{(\alpha)} \\ &= 1 - \exp\left\{ -\dot{N}_0 \sum_{\alpha} \int_0^{P_{pop-in}} \exp\left[-\frac{A\left(1 - \beta^{(\alpha)} P^{1/3} / \tau_{th}\right)^n}{k_B T} \right] \frac{dP}{P} \right\} \end{aligned} \tag{5.9}$$

where the dimensionless parameter $\dot{N}_0 = \dot{n}_0 V P / \dot{P}$ will be obtained by fitting to experimental data. In deriving the above equation, we note that the experiments were conducted at constant $\dot{P}/P$. The cumulative probability relates to the pop-in probability, p, by $f = \int_0^{P_{pop-in}} p(P) dP$ or $p\left(P_{pop-in}\right) = df / dP_{pop-in}$, so that

$$\begin{aligned} p = \frac{\dot{N}_0}{P_{pop-in}} &\exp\left\{ -\dot{N}_0 \sum_{\alpha} \int_0^{P_{pop-in}} \exp\left[-\frac{A\left(1 - \beta^{(\alpha)} P^{1/3} / \tau_{th}\right)^n}{k_B T} \right] \frac{dP}{P} \right\} \times \\ &\sum_{\alpha} \exp\left[-\frac{A\left(1 - \beta^{(\alpha)} P_{pop-in}^{1/3} / \tau_{th}\right)^n}{k_B T} \right] \end{aligned} \tag{5.10}$$

Eq. (5.10) can be integrated to produce the solid lines in Fig. 5.5(a). For all the indentation directions, we use the same activation energy form in Eq. (5.6), and fit τ_{th} and $\dot{N}_0$ for each indentation direction. Results for this Method (I) are given in Table 5.1. We

found that $n = 5.2$ and $A = 73eV \approx 5Gb^3$. The fitted theoretical stress for each indentation direction deviates slightly from the fitted value based on pop-in loads at 90% cumulative probability in a reasonable range. However, the fitted *n* value is higher than the typical values in Table 3.1.

One hindsight arises for those with surface normal close to [001] direction. The long tail at low pop-in loads suggests that the pop-in be resulted from sudden motion of pre-existing dislocation or other heterogeneous dislocation nucleation mechanisms. In the cumulative probability fitting process, the cumulative probability at applied load near the theoretical strength has to carry all the information from lower pop-in loads including the tail area. Therefore, the fitting parameters will tend to lower the activation energy at applied loads in the tail region to fit the slope of the cumulative probability vs pop-in load curve, which will consequently increase n value if we fixed $A/Gb^3 = 5$ in our fitting. This results into a higher n value than the typical values in Table 3.1. Consequently, we perform out fitting to the $p \sim P_{pop-in}$ curves as shown by a representative fitting result in Fig. 5.7(a) for [2 1 2] direction.

Rewriting Eq. (5.10) as,

$$t\left(P_{pop-in}\right) = \ln\left(\dot{N}_0\right) - \dot{N}_0 s\left(P_{pop-in}\right), \tag{5.11}$$

where the two functions $t\left(P_{pop-in}\right)$ and $s\left(P_{pop-in}\right)$ are given by

$$s\left(P_{pop-in}\right) = \sum_{\alpha} \int_0^{P_{pop-in}} \exp\left[-\frac{A\left(1-\beta^{(\alpha)}P^{1/3}/\tau_{th}\right)^n}{k_B T}\right]\frac{dP}{P}, \tag{5.12}$$

$$t\left(P_{pop-in}\right) = \ln\left(pP_{pop-in}\right) - \ln\left(\sum_{\alpha}\exp\left[-\frac{A\left(1-\beta^{(\alpha)}P_{pop-in}^{1/3}/\tau_{th}\right)^n}{k_B T}\right]\right). \tag{5.13}$$

Therefore we can fit $\dot{N}_0$ from the slope of $t \sim s$ curve.

The fitting procedure is specified as follows. With a given indentation direction, we first generate the $p \sim P_{pop-in}$ histogram from the $f \sim P_{pop-in}$ curve. Then, we estimate τ_{th} for each direction and fix $A/Gb^3 = 5$. Input all above parameters into Eq. (5.11), we can find n for all directions. A given example is shown in Fig. 5.7(a). Normally, from Eq. (5.11), the s and t should have a linear relationship. However, data at the left tail in Fig. 5.5(a) will not obey this linear relationship. Fig. 5.7(b) shows typical results of probability vs pop-in load curve. After removing the left tail, it is found that n is about 4.2 which is a reasonable value as

shown in Table 3.1. From the fitted $\dot{N}_0$ and n, we can generate dashed line in Fig. 5.7(b) which differs significantly from the solid line as fitted from $f \sim P_{pop-in}$.

Results for the Method (II) are also given in Table 5.1. The fitted τ_{th} is closer to the value from pop-in loads at 90% cumulative probability than fitted from cumulative probability curve. Most importantly, the fitted n is found to be 4.2, which is in the appropriate range in Table 3.1. From these two fitting Methods, it can be concluded that the kinetic analysis of pop-in data also prove the anisotropy analysis based on the indentation Schmid factor, suggesting that the Schmid-type criterion for homogeneous dislocation nucleation is generally appropriate.

5.5 Discussions

The dependence of nanoindentation pop-in tests on the indentation crystallographic direction is studied theoretically and experimentally. An indentation Schmid factor, S, is defined as the ratio of the maximum resolved shear stress from all possible slip systems to the maximum contact pressure. Based on the anisotropic elasticity analysis, we have derived in closed form the stress fields under Hertzian contact, and have computed the indentation Schmid factor for Ni and NiAl single crystals. The pop-in event, as a consequence of homogeneous dislocation nucleation, will occur when the maximum resolved shear stress reaches the theoretical strength τ_{th}, so that the pop-in load P_{crt} is given by $P_{crt} = \left(\frac{\tau_{th}}{S}\right)^3 \frac{\pi^3 R^2}{6E_r^2}$ with indenter radius *R* and reduced indentation modulus E_r.

Nanoindentation tests were tested on NiAl single crystals, which have B2 structure and $\{110\}\langle 001\rangle$ simple slip systems. A number of representative crystallographic orientations on the standard <001> triangle of the inverse pole figure were selected as indentation directions. Comparisons between the pop-in statistical data and our theoretical predictions lead to the following conclusions.

- The crystallographic dependence of the pop-in loads agrees reasonable well with the predictions based on the indentation Schmid factor, which further supports that nanoindentation pop-in corresponds to the homogeneous dislocation nucleation in defect-free crystals.

- The location where the maximum resolved shear stress is reached can be substantially away from the contact center. It is primarily governed by indenter shape, elastic anisotropy, and slip systems.
- The normal-shear coupling effects cannot be distinguished from the relationship between measured pop-in loads and indentation direction, because the normal stress to the slip plane and resolve shear stress under Hertzian contacts (even for anisotropic crystals) are generally comparable and thus S in Eq. (2.24) and S_{eff} in Eq. (5.4) vary similarly with respect to the indentation direction.
- A thermal activation model is developed to study the crystallographic dependence of the pop-in statistics. Except for small deviations in indentation directions close to <001>, predictions based on the Schmid-type dislocation-nucleation criterion again agree well with the experimental measurements.

Table 5.1 The indentation Schmid factor of the α-th slip system, $S^{(\alpha)}$, as defined in Eq. (5.7), and the fitting parameter $\dot{N}_0 = \dot{n}_0 VP/\dot{P}$ and τ_{th} in Eq. (5.9) are given with respect to a number of indentation directions. The unit of τ_{th} is GPa. Method (I) is based on fitting $f \sim P_{pop-in}$ as in Fig. 5.5(a). Method (II) is based on fitting $p \sim P_{pop-in}$ and removing the left tail as in Figs. 5.5(b) and 5.8.

Indentation direction	$s^{(1)}$ $(011)[100]$	$s^{(2)}$ $(0\bar{1}1)[100]$	$s^{(3)}$ $(101)[010]$	$s^{(4)}$ $(\bar{1}01)[010]$	$s^{(5)}$ $(110)[001]$	$s^{(6)}$ $(\bar{1}10)[001]$	Method (I)		Method (II)	
							τ_{th} (fitted)	$\dot{N}_0$ (fitted)	τ_{th} (fitted)	$\dot{N}_0$ (fitted)
<111>	0.347	0.132	0.346	0.132	0.364	0.155	8.5	6.56	8.5	3.96
<221>	0.325	0.293	0.323	0.199	0.361	0.213	8.0	6.92	8..0	6.21
<421>	0.316	0.246	0.291	0.241	0.351	0.196	8.6	9.22	8.6	22.64
<110>	0.318	0.317	0.248	0.012	0.318	0.097	8.6	12.90	8.6	11.75
<441>	0.345	0.274	0.281	0.080	0.346	0.106	10.2	12.00	10.2	19.99
<521>	0.301	0.245	0.282	0.323	0.337	0.212	11.2	65.90	11.2.	241.67
<411>	0.258	0.278	0.258	0.257	0.331	0.250	12.5	150.00	13.0	2.7×10^3
<720>	0.262	0.262	0.244	0.228	0.301	0.219	9.75	28.86	9.75	252.97

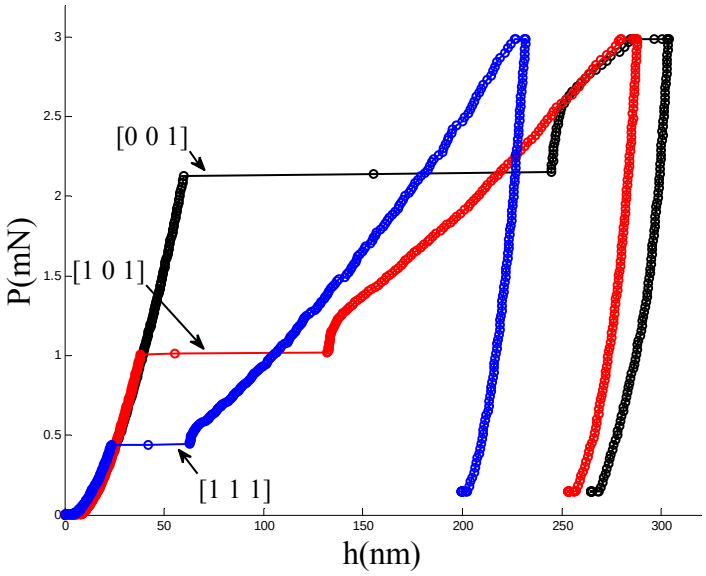

(a)

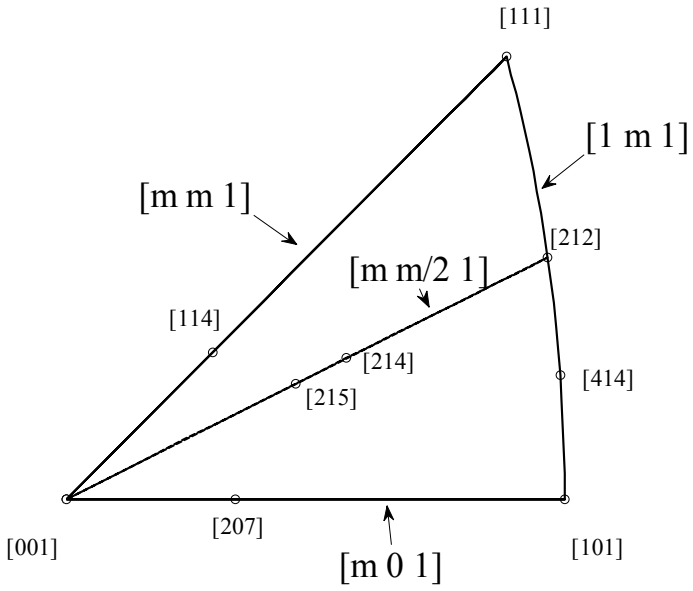

(b)

Figure 5.1 (a) Representative load-displacement curves for NiAl single crystals under spherical indentation with a tip radius of R=580nm. (b) Indentation directions used in the tests are marked on the standard [001] triangle in the inverse pole figure.

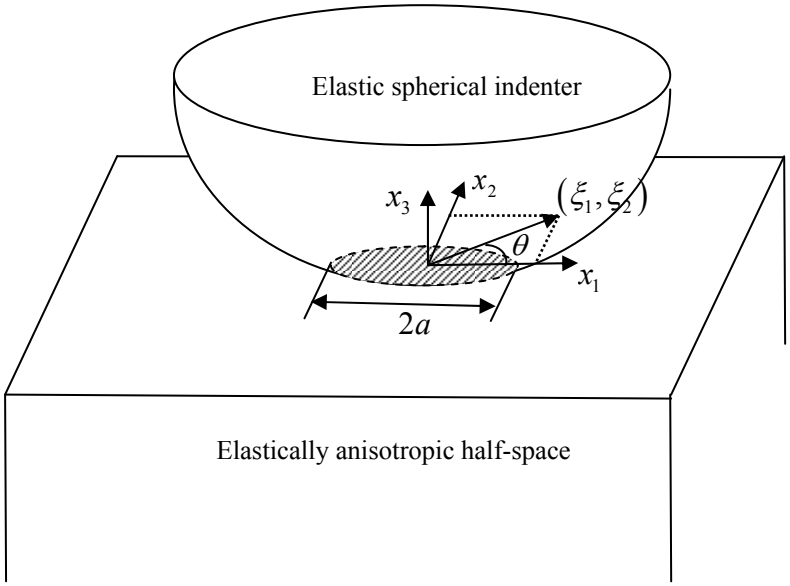

Figure 5.2 Schematic illustration of an elastically anisotropic specimen under a spherical indenter with a radius of R. The contact area is assumed to be circular with a radius of a.

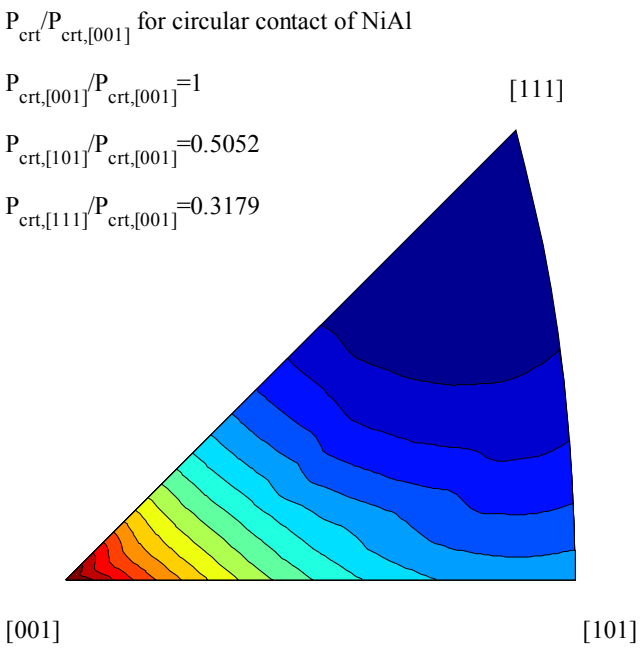

Figure 5.3 Contours of the critical pop-in load, P_{crt}, normalized by $P_{crt,[001]}$ plotted for NiAl single crystals under spherical indentation.

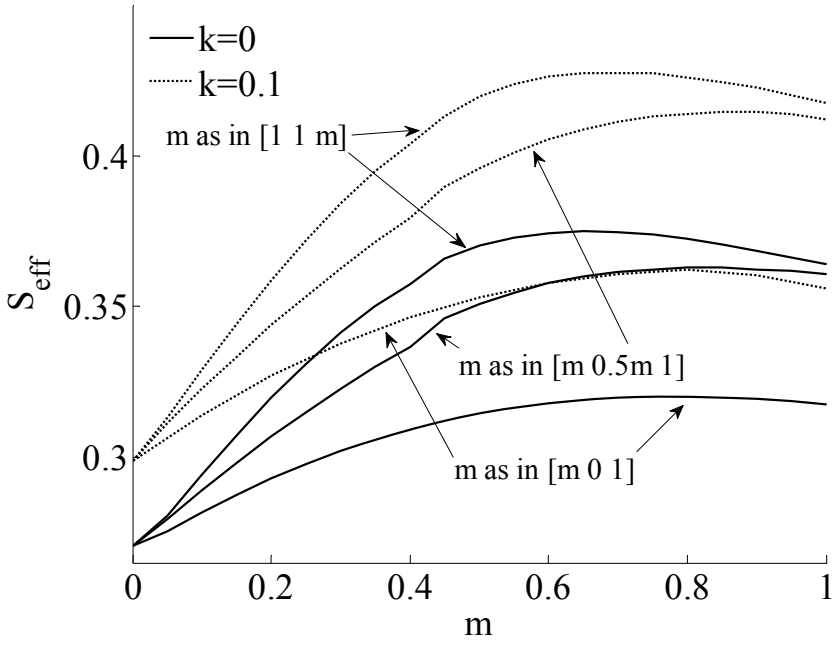

Figure 5.4 The pressure effect on the slip system is modeled by the effective Schmid factor, S_{eff} . With several representative values of normal-shear coupling coefficient *k*, we plot S_{eff} for spherical indentation on NiAl with indentation directions along $[mm1]$, $[m\,\frac{m}{2}1]$, and $[m01]$ with *m* varying from 0 to 1.

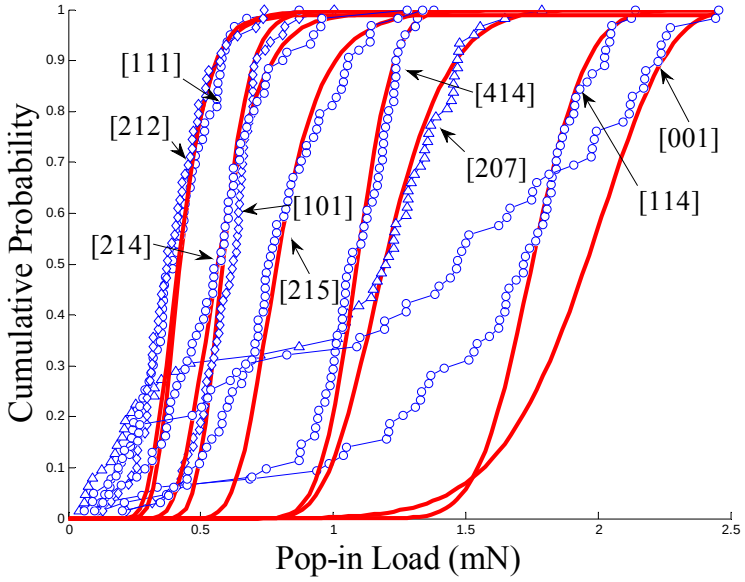

(a)

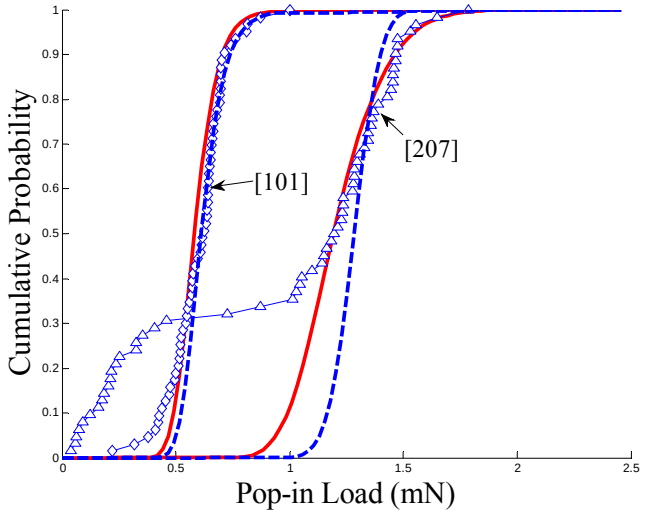

(b)

Figure 5.5 (a) The cumulative pop-in probability, f, as a function of pop-in load for spherical indentation on NiAl single crystals with a number of indentation directions. Solid lines are predictions from the stress-assisted, thermally activated model of homogeneous dislocation nucleation. (b) The comparison of two fitting methods for $[101]$ and $[207]$ directions. The solid lines are based on fitting $f \sim P_{pop-in}$, while the dashed lines on fitting $p \sim P_{pop-in}$ and removing the left tail (see Fig. 5.7 for details), where $p = df / dP_{pop-in}$.

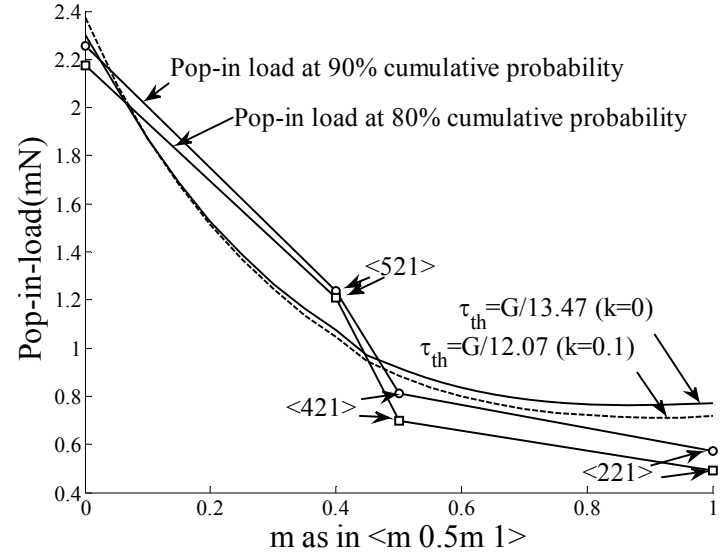

(a)

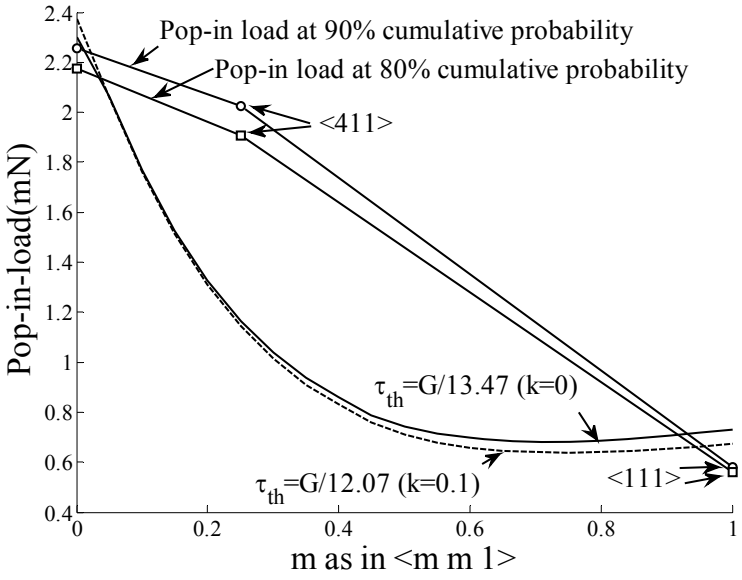

(b)

Figure 5.6 Comparisons between predicted and measured pop-in loads for spherical indentation on NiAl with indentation directions along $[mm1]$, $[m\frac{m}{2}1]$, and $[m01]$. The experimental data of measured pop-in loads of 90% and 80% cumulative probabilities for each direction are shown by the solid lines with open markers. The theoretical strength is fit from all the indentation directions.

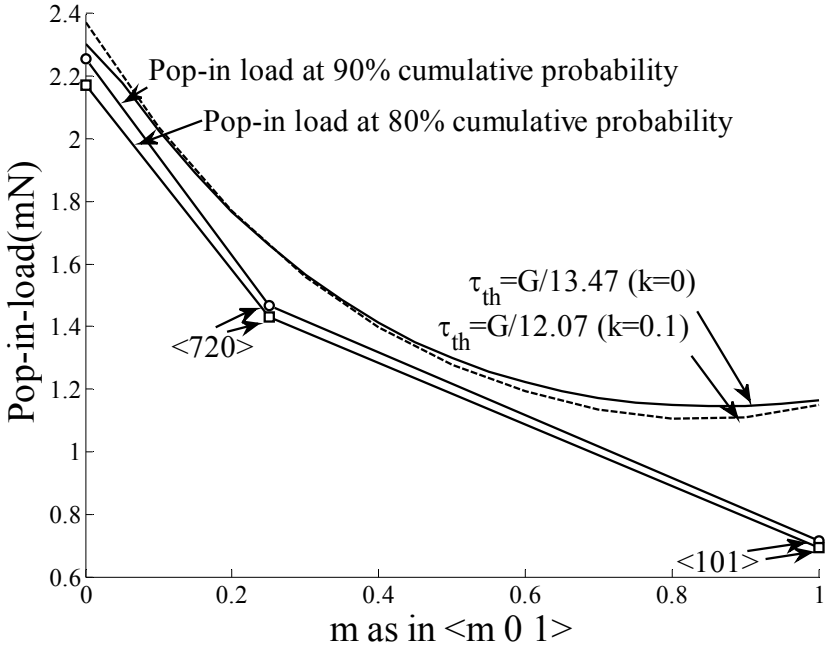

(c)

Figure 5.6 (cont'd) Comparisons between predicted and measured pop-in loads for spherical indentation on NiAl with indentation directions along $[mm1]$, $[m\frac{m}{2}1]$, and $[m01]$. The experimental data of measured pop-in loads of 90% and 80% cumulative probabilities for each direction are shown by the solid lines with open markers. The theoretical strength is fit from all the indentation directions.

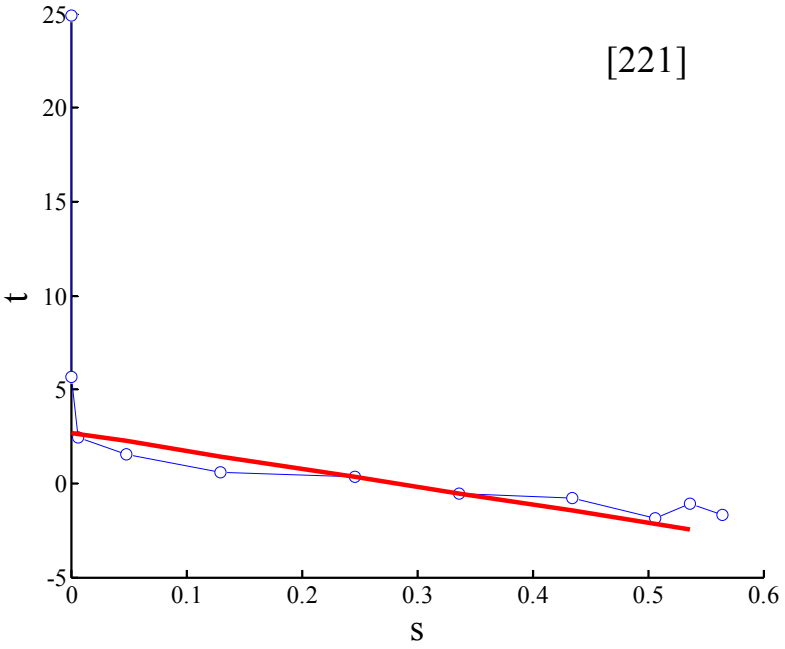

(a)

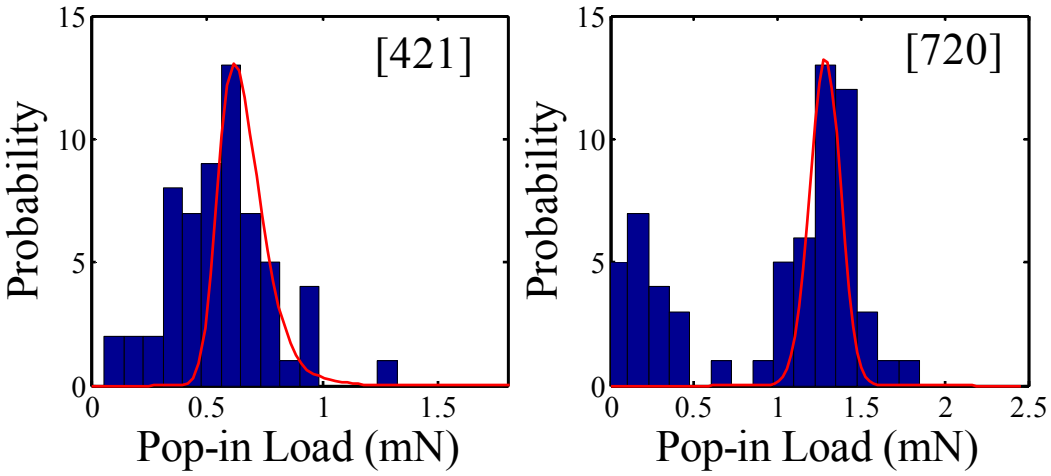

(b)

Figure 5.7 (a) Fitted s and t in Eq. (5.11) for [2 1 2] direction. (b) Typical results of probability vs pop-in load curve.

Chapter VI

Scale Effects in Pop-In Strength due to Pre-Existing Defects

6.1 Introduction

In Chapter V, we have systematically studied nanoindentation pop-in behavior when the governing mechanism is homogeneous dislocation nucleation in defect-free single crystals. In this case, a dislocation will nucleate when the maximum resolved shear stress in the solid reaches the theoretical strength of the material. When the maximum resolved shear stress is less than but close to this athermal limit, the thermal energy can kinetically activate the dislocation nucleation process. The predicted crystallographic dependence of the pop-in statistics agrees well with the experimental results of B2-type NiAl single crystals. However, a large deviation from our theoretical prediction is observed when the indentation directions are close to <001>. As shown in Fig. 5.5(a), the cumulative probability curve exhibits a long tail at low pop-in loads for those with surface normal close to <001> direction (which also corresponds to large stressed-volume sizes), which suggests that the pop-in result from the sudden motion of pre-existing dislocations or heterogeneous dislocation nucleation (e.g., Frank-Read dislocation nucleation).

A similar effect can be observed by using different indenter radii, as denoted as a different type of indentation size effect (ISE) [104-106]. Experimentally, the maximum shear stresses as determined at the measured pop-in loads exhibit a monotonic decrease with respect to the increase of the indenter radius. A representative result is shown in Fig. 6.1 for Mo <001> single crystals with respect to the indenter radius. In Fig. 6.1, the mean maximum shear stresses values are measured from Fig. 2 of Ref. [105], and the error bars are generated from 90% and 10% cumulative probability of the maximum shear stresses for each indenter radius. When the indenter size is small (e.g., 115nm in our case), the stress needed for pop-in is found to be on the order of the theoretical strength (~G/7 in this case). As the indenter radius increases, the maximum shear stress first decreases, and data scatter increases. If the indenter size is large enough (larger than 64 μm, in our case), the strength approaches a plateau value and its scatter becomes negligible. When the indenter size is in the intermediate

range (between 178nm and 64 μm in Fig. 6.1), the measured pop-in loads exhibit a variety range of scatter. This may be explained qualitatively as follows. When the indenter radius is sufficiently small, the highly stressed zone in the material is so small that it is likely to be defect free. Thus the pop-in results from the homogeneous dislocation nucleation at the theoretical stress. At the limit of a large indenter, where a sufficiently large volume of material is stressed, pop-in would tend to be caused by the sudden configurational change of the pre-existing defect networks rather than by the homogeneous dislocation nucleation. And the critical stress required for such defect-assisted events is supposed to be about one or two orders of magnitudes lower than the theoretical strength of the material. For indenters with intermediate radii, pop-in would result from the competition between these two mechanisms.

Yet another similar behavior is observed from nanoindentation tests. If the sample is prestrained before nanoindentation test, a monotonic decrease of the measured pop-in loads with respect to the increase of prestrain on Ni and Mo single crystals is observed [104,106]. Because a large prestrain gives a large defect density, it is more likely for the pop-in to occur by a defect-assisted mechanism rather than by the homogeneous dislocation nucleation mechanism.

Clearly, the critical stress for the defect-assisted pop-in mechanism is related to the dislocation density and the indenter radius. This mechanism has been successfully demonstrated from a stochastic model developed by Morris et al. [105], where the data scatter in Fig. 6.1 are accurately predicted but only for the indenter size larger than 1.5μm. Inspired by this work, in this Chapter we will unify the homogeneous dislocation nucleation model in Chapter V and the defect-assisted stochastic model to investigate the effects of indenter radius and prestrain. The cumulative pop-in probability contains convoluted information from the homogenous dislocation nucleation and the possible heterogeneous dislocation nucleation due to the unstable change of existing defect network. As will be shown shortly, this unified model accurately describes the tail effect for indentation directions close to [001] in NiAl single crystals in Chapter V. And the predicted statistical pop-in loads from the unified model agrees quantitatively well with the indenter radius effects and the indentation prestrain effects.

6.2 Pre-Existing Defect-Assisted, Stochastic Model (Morris *et al.* [105])

For a crystalline solid with pre-existing and randomly distributed defects, a pop-in event corresponds to a sudden and unstable change of dislocation network, such as bowing out

dislocation segment as in the Frank-Read model, breaking dislocation pinning points or junctions, to name a few. Following Morris et al. [105], we avoid differentiating the actual physical processes that lead to the nanoindentation pop-in behavior, but simply assume that the pop-in will occur when the stressed volume under the indenter contains a pre-existing defect and the shear stress is larger than τ_{defect} - a material constant assumed in this work. This assumption is supported from the indenter radius effect. If the indenter radius is small, the highly stressed volume in the solid is small, and thus is more likely to be defect free. Therefore, a large pop-in load is needed. In contrast, a large indenter radius probes a large volume in the solid, and the possibility to encounter a pre-existing defect is high, which results in a low pop-in load.

Suppose that the crystalline solid has a pre-existingdefect density ρ_{defect} and the highly stressed region, where the maximum shear stress is larger than τ_{defect}, has a volume V_d. The probability, $l_0\left(\rho_{defect}, V_d\right)$, for finding no defect in the volume V_d, obeys a Poisson distribution, as given by [105],

$$l_0\left(\rho_{defect}, V_d\right) = \exp\left(-\rho_{defect} V_d\right). \tag{6.1}$$

The highly stressed volume under nanoindentation scales with the indenter radius (as a loading parameter), material anisotropy, and crystallography. Assuming isotropic elastic contact and using the maximum shear stress (rather than the resolved shear stress), $\tau^*_{\max}$, under a given load *P*, Morris et al. has given a dimensional relationship of

$$V_d / a^3 = f\left(\tau_{defect} / \tau^*_{\max}\right). \tag{6.3}$$

where $a = \left(3PR / 4E_r\right)^{1/3}$ is the contact radius [107], and $\tau^*_{\max}$ can be derived from (2.18) and (2.24).

The cumulative probability of pop-in is therefore,

$$\begin{aligned} f &= 1 - l_0\left(\rho_{defect}, V_d\right) \\ &= 1 - \exp\left(-\rho_{defect} V_d\right) \end{aligned}. \tag{6.2}$$

Eq. (6.2) has been used to successfully explain the cumulative pop-in probability curves in Fig. 6.1 but only for indenter radius larger than 1.5μm. For small indenter radii, predictions based on Eq. (6.2) will significantly overestimate the pop-in loads because the chance of

finding a pre-existing dislocation in this case is negligibly small so that the pop-in probability will be extremely small.

6.3 A Unified Pop-In Model Accounting for Homogenous and Heterogeneous Dislocation Nucleation

While Eq. (6.2) has successfully predicted nanoindentation pop-ins for indenter radii larger than 1.5 μm, for indenter radii less than 1.5 μm, Eq. (6.2) will underestimate the pop-in probability. In this case, it is the homogeneous dislocation nucleation that is responsible for the observed pop-in behavior because of the high stress in this case. In retrospect, in Chapter V, Eq. (5.9) only successfully predicts the cumulative pop-in probability for the homogenous dislocation nucleation, but deviates at low loads where long tails were observed in the cumulative pop-in probability curves for NiAl single crystals. Consequently, the cumulative probability contains convoluted information from the homogeneous dislocation nucleation model in Eq. (5.9) and the stochastic model in Eq. (6.2).

For a crystalline solid with a pre-existing defect density ρ_{defect} under nanoindentation, the total survivability, w (i.e. neither homogenous dislocation nor heterogeneous dislocation nucleates), is given by the product of Eq. (5.8) and Eq. (6.2):

$$\begin{aligned} w &= l \cdot \prod_{\alpha} q^{(\alpha)} \\ &= \exp\left(-\rho_{defect} V_d\right) \cdot \exp\left(-\dot{N}_0 \sum_{\alpha} \int_0^{P_{pop-in}} \exp\left[-\frac{A\left(1-\beta^{(\alpha)} P^{1/3} / \tau_{th}\right)^n}{k_B T} \right] \frac{dP}{P} \right). \\ &= \exp\left(-\rho_{defect} V_d - \dot{N}_0 \sum_{\alpha} \int_0^{P_{pop-in}} \exp\left[-\frac{A\left(1-\beta^{(\alpha)} P^{1/3} / \tau_{th}\right)^n}{k_B T} \right] \frac{dP}{P} \right) \end{aligned} \tag{6.4}$$

Thus the cumulative pop-in probability is

$$\begin{aligned} f_{unified} &= 1 - w \\ &= 1 - \exp\left(-\rho_{defect} V_d - \dot{N}_0 \sum_{\alpha} \int_0^{P_{pop-in}} \exp\left[-\frac{A\left(1-\beta^{(\alpha)} P^{1/3} / \tau_{th}\right)^n}{k_B T} \right] \frac{dP}{P} \right). \end{aligned} \tag{6.5}$$

Eq. (6.5) is used to generate solid lines in Fig. 6.2 based on NiAl experimental results in Fig. 5.5(a). For all indentation directions, we fix $A / Gb^3 = 5$ and use the same activation energy

form in Eq. (5.6). τ_{th} and n are fitted for each indentation direction from the right part of the cumulative pop-in probability curve. Then, we fit ρ_{defect} and τ_{defect} from the left tail of each direction. Fitted parameters are given in Table 6.1. The fitted n value is 4 for all directions, which is a reasonable value as compared to Table 3.1.

It is evident that Eq. (6.5) successfully predicts both the stochastic (due to pre-existing defects) and statistical (due to thermal effects) behavior of the nanoindentation pop-in events. The long tails that appear for indentations directions close to <100> direction are quantitatively reproduced. From Eq. (2.18) and Eq. (2.24), the contact radius has a relationship with the effective indentation modulus and the indentation Schmid factor as $a = \pi R\tau^*_{\max} / 2E_r S$. And from Fig. 2.2(b) and 2.4(b), directions near <100> have smaller values of $E_r S$ than other directions at the right part of the standard [001] triangle in the inverse pole figure. Thus, if the same level of resolved shear stress is attained in every indentation direction, those directions near <100> will probe larger volumes than the rest, and thus are more susceptible to pre-existing defects. Consequently, the large material anisotropy in NiAl leads to longer tails due to the stochastic effects for indentation directions close to <100>. Our fitting results give τ_{defect} approximately 1/50 of τ_{th}, which is close to the strength of typical Frank-Read dislocation source [108]. And ρ_{defect} is on the same order of magnitude as the experiment observation [105].

The unified model can also predict the indenter radius effect. As has been mentioned earlier in this Chapter, Eq. (6.2) only works well for indenters with sizes larger than 1.5μm in Fig. 6.1, where the maximum shear stress at pop-in loads is much less than the theoretical strength. We use Eq. (6.5) to fit experimental data of Mo <100> single crystals of indenter size 115nm, 178nm, and 580nm in Fig. 6.1. Results are plotted in Fig. 6.3. We first fit the data with indenter size 115nm using Eq. (5.8) as shown by the solid line. Because the indenter radius is very small, the highly stressed region underneath the indenter is so small that there is hardly any chance for a defect to pre-exist. Therefore, all measured pop-in loads result from homogeneous dislocation nucleation. The fact that no tail is observed in Fig. 6.3 can aid this statement. The fitted value of A/Gb^3 is 5, and n is found to be 2.5, which are very reasonable values as suggested in Table 3.1. After we fit 115nm indenter, we use the fitted A and n to generate solid lines for measurements using indenters with radius of 178nm and 580nm. Details on fitting procedure and sensitivity of the fitting parameters

(ρ_{defect} and τ_{defect}) will be given in the next section. As can be seen from Fig. 6.3, when the indenter size is small, e.g. 115nm, the pop-in probability is governed by the homogenous dislocation nucleation behavior. For intermediate sized indenters (e.g., 178nm and 580nm here), the cumulative probability contains information from both thermally activated homogeneous dislocation nucleation and defect-assisted, stochastic pop-in behavior. The resulting scatter depends on the competition and convolution of these two mechanisms.

Our unified model can also predict the prestrain effects observed in the nanoindentation pop-in tests. Experimentally, a set of Mo single crystals samples are prestrained by engineering compressive strains of 0%, 1.5%, 5%, and 13%. Then, nanoindentation tests are conducted on <100> surfaces of these pre-strained samples using an indenter with tip radius of 115nm. Cumulative probability curves with respect to measured pop-in loads are shown in Fig. 6.4. As the prestrain increases, pop-in loads will drop, and a long tail at low pop-in loads emerges which can be clearly seen for 5% and 13% prestrained samples. The unified model in Eq. (6.5) is used to generate solid lines in Fig. 6.4. We first use Eq. (5.8) to fit the data of 0% sample, and find that fitting parameters in Eq. (5.6) are $A/Gb^3 = 5$ and $n = 2.5$. Then we assume that all samples have the same τ_{defect}, and fit ρ_{defect} for each sample. Because the indenter size is very small, τ_{defect} is very high, i.e. $\tau_{defect}/\tau_{th} = 0.8$. As expected, we observe an increase of the defect density with respect to the increase prestrain. However, the fitted τ_{defect} is larger than that in Fig. 6.3 and Morris et al. [105], which will be further discussed in the next section.

6.4 Discussions on Fitting Process and Sensitivity

One major problem of our analysis is the uniqueness of the fitting parameters. For example, when we fit Eq. (6.5) to the R=178nm pop-in data in Fig. 6.3, $\tau_{defect}/\tau_{th} = 0.3$ and $\rho_{defect} = 5\times10^{18}/m^3$ give a reasonably good fitting, and, however, so do $\tau_{defect}/\tau_{th} = 0.7$ and $\rho_{defect} = 5\times10^{19}/m^3$. Moreover, these fitted values of τ_{defect} and ρ_{defect} are much larger than the values in Ref [105], as well as than the values for NiAl data in Fig. 6.2. A question that naturally arises will be whether τ_{defect} should be a material property or depend on stressed volume size.

We further investigate the effects of τ_{defect} and ρ_{defect} in Eq. (6.5) on the resulting cumulative pop-in probability curves. In Fig. 6.5(a), τ_{defect} is taken as 35% of τ_{th}, and different values ρ_{defect} are used to generate the solid lines from Eq. (6.5). A large ρ_{defect} will increase the probability of pop-in, but it does not affect the extent of the tail on the abscissa. That is, the minimum pop-in load in Eq. (6.5) is independent of ρ_{defect}. In Fig. 6.5(b), ρ_{defect} is fixed as $6\times10^{18}/m^3$, and the solid lines are generated from Eq. (6.5) with different values of τ_{defect}. In this case, decreasing τ_{defect} will both increase the probability of pop-in and widen the scatter of the pop-in load. Two sets of τ_{defect} and ρ_{defect} are used in Eq. (6.5) to generate the fitting curves in Fig. 6.6. If we choose parameters that are similar to those used in Ref. [105] (i.e. $\rho_{defect}=1\times10^{17}/m^3$ and $\tau_{defect}=0.1$), the fitting result does not capture the tail shape as well as the fitting result using $\rho_{defect}=5\times10^{18}/m^3$ and $\tau_{defect}=0.7$. Because the indenter radius effect shows that the minimum pop-in load is also correlated to the indenter size, τ_{defect} may display an indentation size effect. Further studies are needed to investigate such an effect, and to improve the model developed in Eq. (6.5).

Table 6.1 Fitted τ_{th}, n, τ_{defect}, and ρ_{defect} in Eq. (6.5) with respect to a number of indentation directions for NiAl single crystals. The unit of τ_{th} and τ_{defect} are GPa. We use the same indentation Schmid factors as those listed in Table 5.1.

Indentation direction	τ_{th} (GPa)	n	τ_{defect} (GPa)	ρ_{defect} ($1/\mu m^3$)
111>	8.2	4	0.19	0.8
<221>	7.3	4	0.19	0.3
<421>	8.3	4	0.19	0.5
<110>	8.0	4	0.19	0.2
<441>	9.5	4	0.19	0.3
<521>	9.8	4	0.19	0.1
<411>	11.7	4	0.19	0.15
<100>	10	4	0.19	0.5
<720>	9.5	4	0.19	0.5

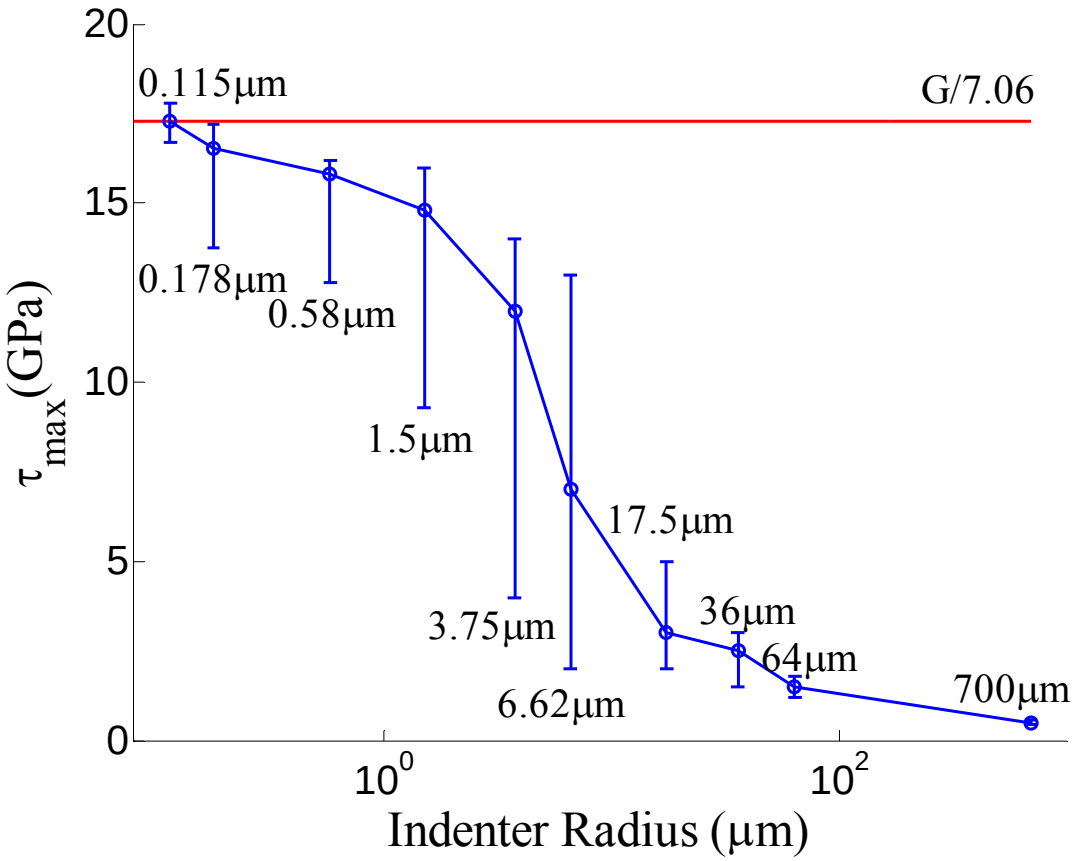

Figure 6.1 The maximum shear stresses under the indenter when pop-in occurs plotted against the indenter radius. For these tests on Mo <001> single crystals, a monotonic decrease of the maximum shear stress is observed with respect to the increase of indenter radii.

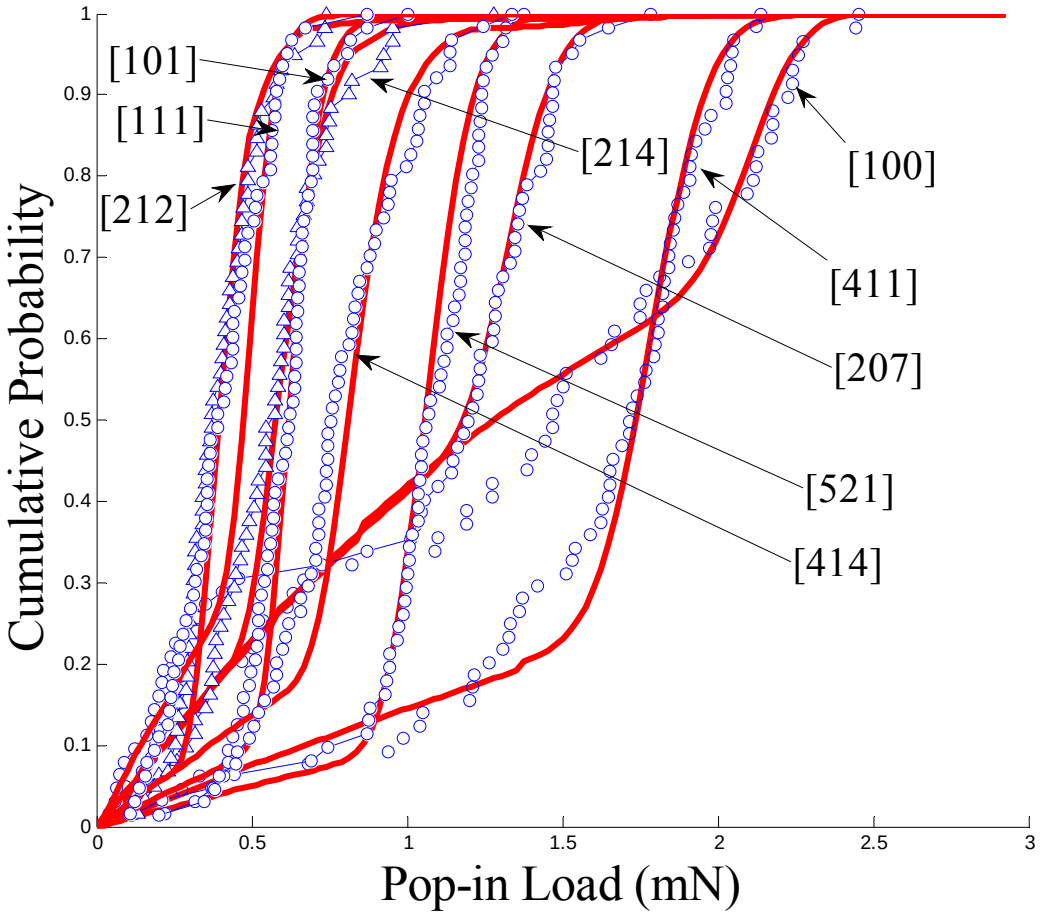

Figure 6.2 The cumulative pop-in probability, *f*, as a function of pop-in load for spherical indentation on NiAl single crystals with a number of indentation directions. Indenter radius is 580 nm. Solid lines are predictions from the unified homogeneous and heterogeneous dislocation model with fitting parameters given in Table 6.1. Refer to Fig. 5.5 for a comparison.

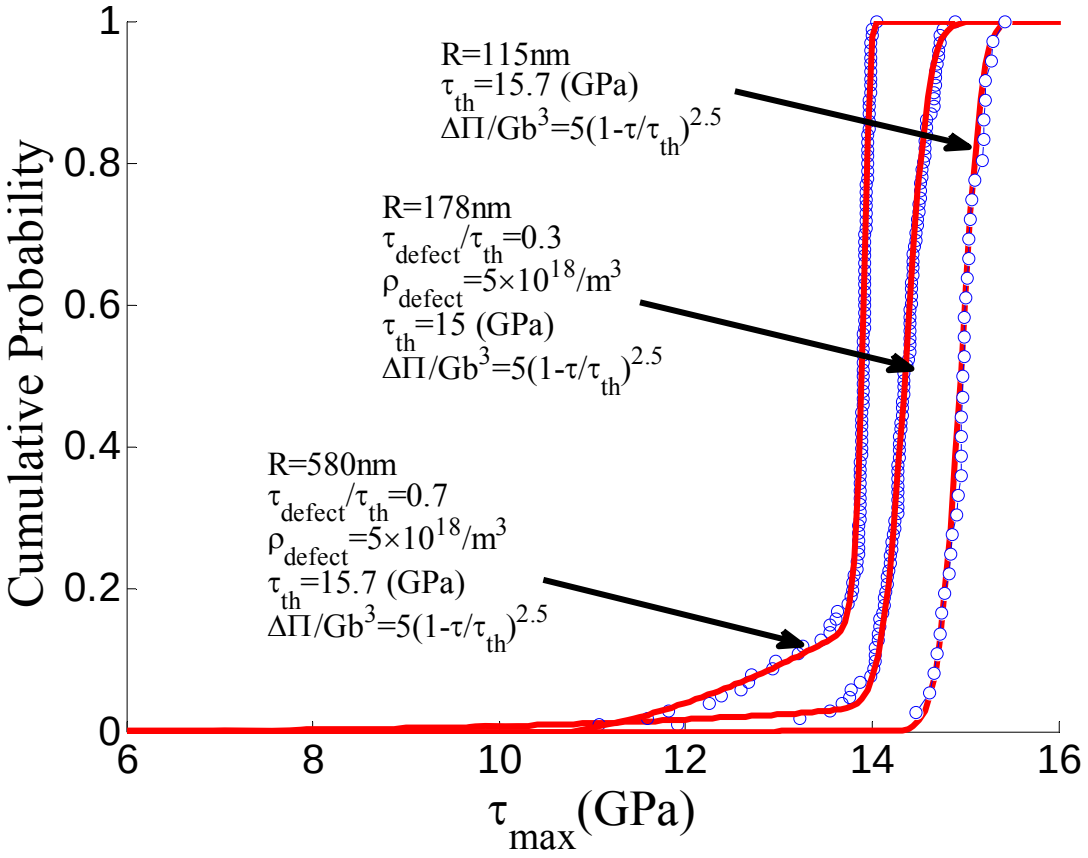

Figure 6.3 Cumulative probability of pop-in, as a function of maximum stress under the indenter, for a series of indenter radii (discete markers). Sold lines show the predictions produced by Eq. (6.5). There are same data used to plot Fig. 6.1.

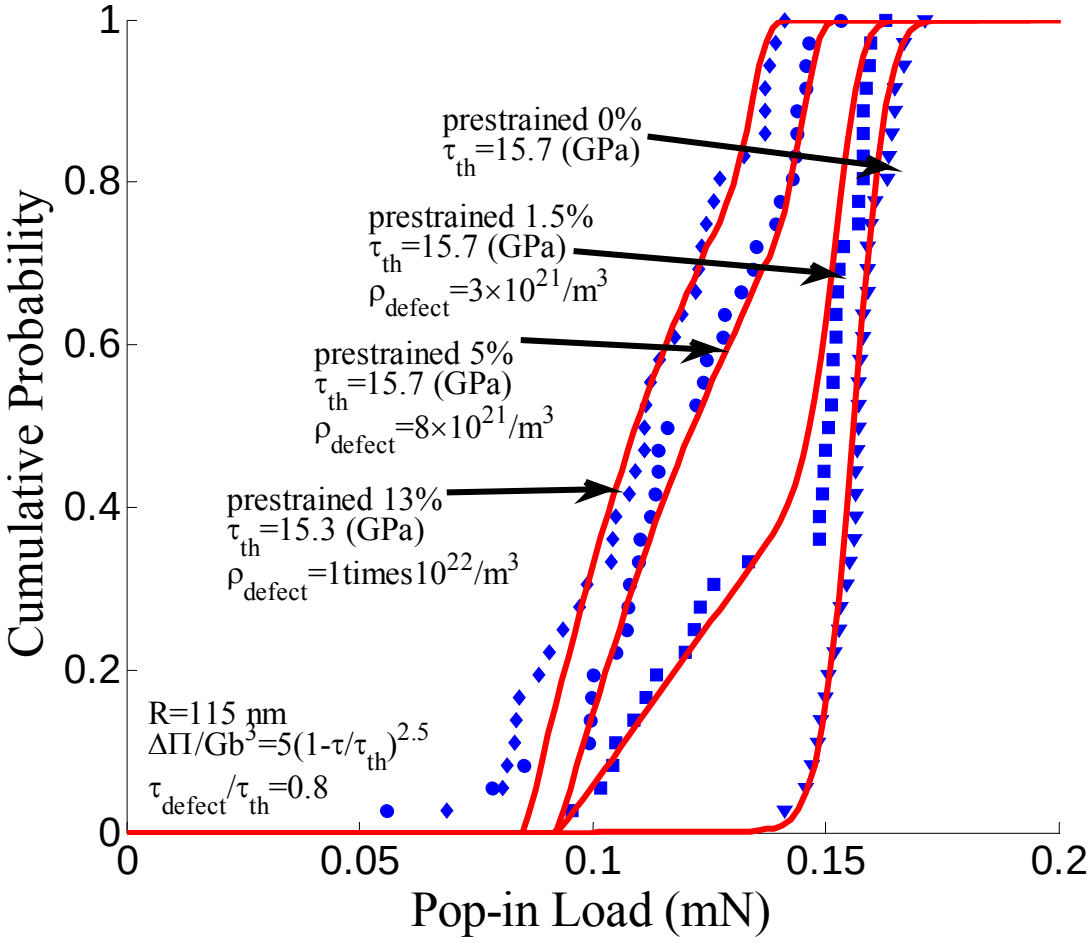

Figure 6.4 Cumulative probability of pop-in, as a function of pop-in loads, for a number of prestrain levels on Mo <001> single crystals. Solid lines show the predictions produced by Eq. (6.5).

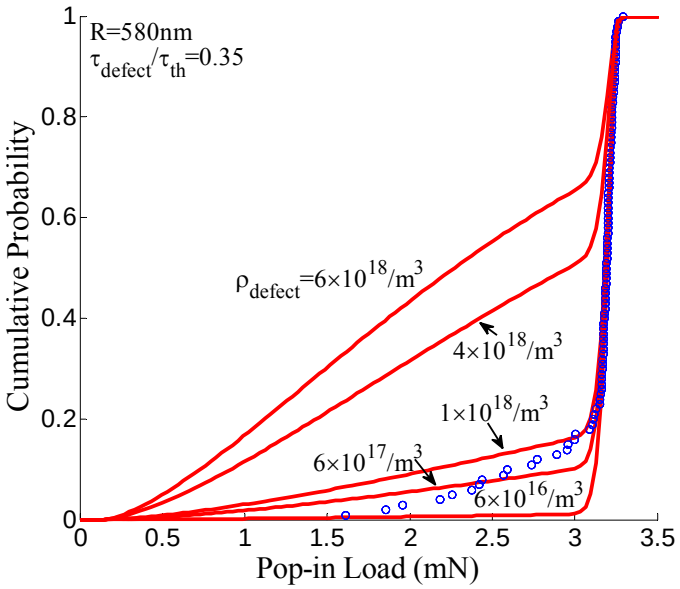

(a)

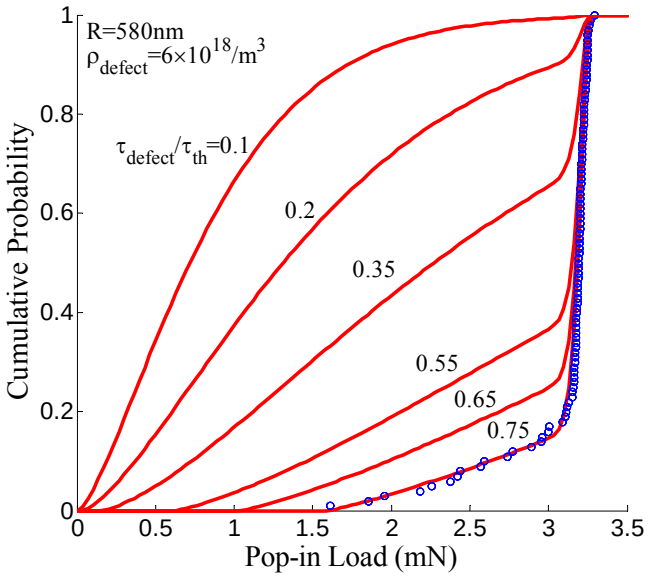

(b)

Figure 6.5 Effects of τ_{defect} and ρ_{defect} in Eq. (6.5) on the cumulative probability of Mo <001> single crystals. The indenter radius is 580nm. In (a), τ_{defect} is fixed to be 35% of the τ_{th}, and the increase of ρ_{defect} will increase the probability of pop-in. However, ρ_{defect} does not affect the range of the pop-in load. In (b), ρ_{defect} is fixed to be $6\times10^{18}/m^3$, and the decrease of τ_{defect} will both increase the probability of pop-in and widen the variety of range of the pop-in load.

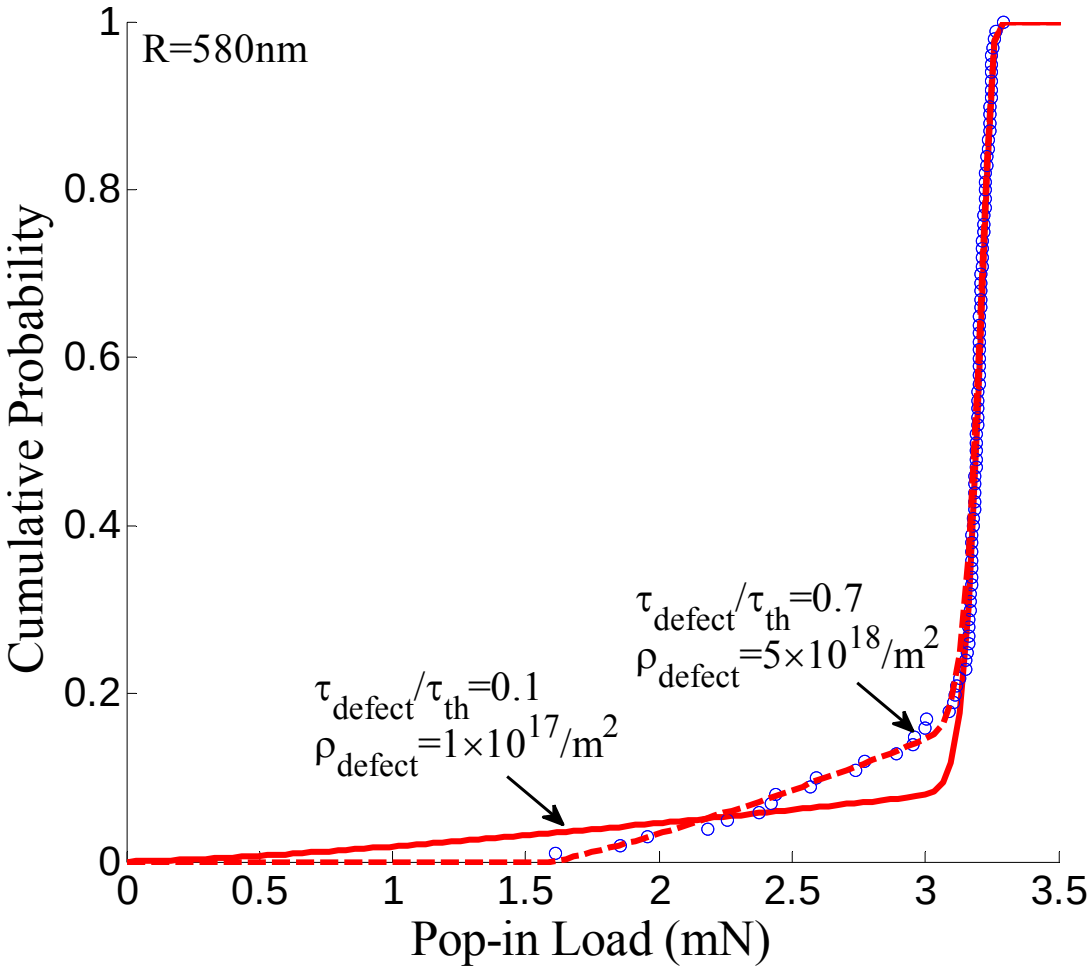

Figure 6.6 Cumulative probability versus pop-in loads for Mo <001> single crystals. The indenter radius is 580nm. Solid lines show the predictions produced by Eq. (6.5) with two different combinations of τ_{defect} and ρ_{defect}.

Chapter VII

Summary and Future Work

It is shown in this thesis that dislocation nucleation behavior in the stressed volume of single crystals at small scales, as illustrated by the nanoindentation pop-in tests, is critically dependent on material type (i.e., their slip systems and crystal structure), resolved shear stress, crystallographic orientation, indenter shape, indenter radius, pre-existing defect type and density, loading rate, and temperature. Our results indicate that a schematic summary of most important parameters can be shown in Fig. 7.1 as discussed below.

Theoretical strength is reached for indentation on defect-free single crystal with tiny indenter tip radius, which has been confirmed by a large number of tests (e.g., Mo, NiAl, Ni in this thesis). The fluctuation of pop-in loads results from the stress assisted, thermally activated process for homogeneous dislocation nucleation. With the increase of indenter radius, the stressed volume size increases, and it is more likely to activate a defect-assisted pop-in process. Eventually the pop-in strength approaches the flow stress of the material which depends on the pre-existing dislocation density. Clearly the effects of dislocation density and indenter radius will be similar. A less explicit dependence is the Schmid factor. As can be seen from Chapter V, for indentations on NiAl single crystal surfaces with surface normal close to <001>, the pop-in loads are larger essentially because of a smaller indentation Schmid factor for these indentation directions. As the increase of indenter radius, or the increase of pre-existing dislocation density, or the decrease of Schmid factor, one can see the transition from behavior (A) – as shown in Fig. 6.3 (R=115nm), to behavior (B) – as shown in Fig. 6.6 (where a tail begins to emerge), to behavior (C) – as shown in Fig. 6.2 (<001> indentation case where the tail dominates the entire regime), and eventually to behavior (D) which corresponds to a steep curve in the cumulative probability versus pop-in load plot. Future work is needed to see if the above plot is also applicable for other small scale tests.

Our theory is, however, not consistent with the observation of the orientation effects for pop-in tests on Ni single crystals. From Eq. (5.2), the pop-in load is proportional to $1/S^3E_r^2$, and Fig. 2.2(a) and Fig.2.4(a) give that the <100> indentation needs the largest pop-in load while the <101> one needs the least among these three directions. However, experiments on

Ni single crystals show that <111> indentation requires the largest pop-in load, while <110> requires the lowest [109]. Further studies are needed to see if these tests are already influenced by the defect-assisted mechanism, or if such defect-assisted pop-in events depend on indentation directions.

The homogeneous dislocation nucleation is a rate and temperature dependent process [10,11]. If one decreases the loading rate or increase the environmental temperature of the experiment, it should facilitate the thermally activated dislocation nucleation process because a decreasing loading rate will allow the solid more time to response to each incremental load and an increasing environmental temperature will give the solid more thermal energy. While this rate and temperature effects have been successfully observed from Pt [11], other materials such as Ta [109], Mo, and Ni do not exhibit a clear sensitivity on the loading rate and the temperature. It seems that the rate and temperature effects may depend on material structures, material slip systems, and indenter tip radius, which need further efforts to distinguish those factors. Moreover, the above discussion is under the assumption that the heterogeneous dislocation nucleation is independent of the rate and temperature effects, which is also amenable to further investigation.

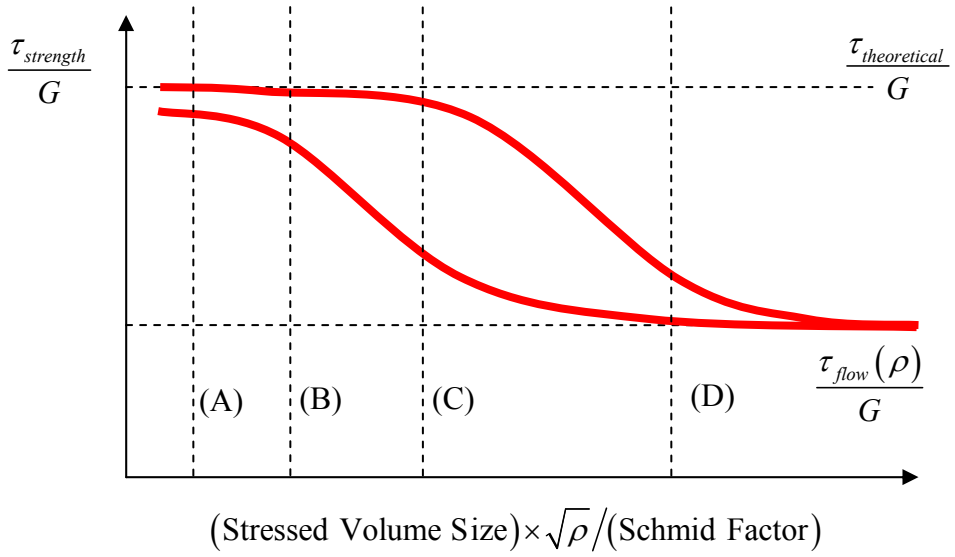

Figure 7.1 Schematic illustration of the dependence of nanoindentation pop-in strength (as bounded within the two curves) as a function of the stressed volume size, pre-existing dislocation density, and Schmid factor. The combination of these three parameters indicates their respective effects rather than a rigorous relationship.

LIST OF REFERENCES

1. Doerner M F and Nix W D. J Mater Res 1986; 1:601
2. Oliver W C and Pharr G M. J Mater Res 1992; 7:1564
3. Oliver W C and Pharr G M. J Mater Res 2004; 19:3
4. Page T F, Oliver W C and McHargue C. J Mater Res 1992; 7: 450
5. Corcoran S G, Colton R J, Lilleodden E T and Gerberich W W. Phys Rev B 1997; 55: 16057
6. Suresh, S, Nieh T-G and Choi B W. Scripta Mater 1999; 41: 951
7. Chiu Y L and Ngan A H W. Acta Mater 2002; 50: 1599
8. Lorenz D, Zeckzer A, Hilpert U, Grau P, Johansen H and Leipner H S. Phys Rev B 2003; 67: 172101
9. Van Vliet K J, Li J, Zhu T, Yip S., and Suresh S. Phys Rev B 2003. 67:104105
10. Schuh C A and Lund A C. J Mater Res 2004; 19: 2152
11. Schuh C A, Mason J K and Lund A C. Nature Mater 2005; 4: 617
12. Mason J K, Lund A C and Schuh C A. Phys Rev B 2006; 73: 054102
13. Wo P C, Zuo L and Ngan A H W. J Mater Res 2005; 20: 489
14. Ngan A H W, Zuo L and Wo P C. Proc R Soc A 2006; 462: 1661
15. Zuo L and Ngan A H W. Phil Mag Lett 2006; 86: 355
16. Bei H, George E P, Hay J L, Pharr G M. Phys Rev Lett 2005; 95: 045501
17. Bei H, Gao Y F, Shim S, George E P and Pharr G M. Phys Rev B 2008; 77: 060103
18. Venkataraman S K, Kohlstedt D L and Gerberich W W. J Mater Res 1993; 8: 685
19. Kelchner C L, Plimpton S J and Hamilton J C. Phys Rev B 1998; 58: 11085
20. Zimmerman J A, Kelchner C L, Klein P A, Hamilton J C and Foiles S M. Phys Rev Lett 2001; 87: 165507
21. Zhu T, Li J, Van Vliet K J, Ogata S, Yip S and Suresh S. J Mech Phys Solids 2004; 52: 691
22. Zhang Z, Yoon J, and Suo Z. Appl. Phys. Lett 2006; 89: 261912
23. Feron M, Zhang Z, and Suo Z. J Appl Phys 2007; 102: 023502
24. Kammler M, Chidambarrao D, Schwarz K W, Black C T and Ross F M. Appl Phys Lett 2005; 87: 133116
25. Freund L B and Suresh S, Thin Film Materials, Cambridge University Press 2003
26. Gao Y F, Lucas B N, Hay J C, Oliver W C and Pharr G M. Scr Mater 2006; 55: 653
27. Lee H, Lee J H and Pharr G M. J Mech Phys Solids 2005; 53: 2037

28. Chen X, Ogasawara N, Zhao M and Chiba N. J Mech Phys Solids 2007; 55: 1618
29. Gao H, Chiu C H and Lee J Int J Solids Struct 1992; 29: 2471
30. Saha R and Nix W D. Acta Mater 2002; 50: 23
31. Chen S, Liu L and Wang T. Surf Coat Tech 2005; 191: 25
32. Xu H and Pharr G M. Scr Mater 2006; 55: 315
33. Han S M, Saha R and Nix W D. Acta Mater 2006; 54: 1571
34. Cao G and Chen X. J Appl Phys 2007; 102: 123513
35. Pharr G M, Oliver W C and Brotzen F R. J Mater Res 1992; 7: 613
36. Vlassak J J and Nix W D. Philos Mag A 1993; 67: 1045
37. Gao Y F and Pharr G M. Scr Mater 2007; 57: 13
38. Xu Z H and Li X D. Acta Mater 2008; 56: 1399
39. Yu H Y, Sandy S C and Rath B B. J Mech Phys Solids 1990; 38: 745
40. Gao Y F, Xu H T, Oliver W C and Pharr G M. J Mech Phys Solids 2008; 56: 402
41. Hill R and Storåkers B, in: Eason, G., Odgen, R.W. (eds), Elasticity: Mathematical Methods and Applications. Ellis Horwood Limited, Chichester, England 1990; pp. 199-209
42. Stroh A N. Philos Mag 1958; 7: 625
43. Suo Z. Proc R Soc Lond A 1990; 427: 331
44. Gao Y F and Suo Z. J Mech Phys Solids 2003; 51: 147
45. Gao Y F. Int J Solids Struct 2003; 40: 6429
46. Yu H H, Shrotriya P, Gao Y F and Kim K –S. J Mech Phys Solids 2007; 55: 489
47. Gao Y F, Yu H H and Kim K –S. J Mech Phys Solids 2008; 56: 2759
48. England A H. Complex Variable Methods in Elasticity, Wiley Interscience 1971
49. Li T L and Li Z. Int J Fract 2007; 144: 45
50. Li T L, Li Z and Sun J. Scr Mater 2006; 55: 703
51. Willis J R. J Mech Phys Solids 1996; 14: 163
52. Li T L, Lee J H and Gao Y F. Int J of Appl Mech 2009; 1: 515
53. Nelder J A and Mead R. Comp J 1965; 7: 308
54. Sneddon I N, Int J Eng Sci 1965; 3: 47
55. Levin D. J Comput Appl Math 1996; 67: 95
56. Levin D. J Comput Appl Math 1997; 78: 131
57. Xiang S and Wang H. J Comput Appl Math 2009; 217: 28

58. Hirth J P, Lothe J. Theory of Dislocations, 2nd ed. John Wiley, New York, 1982
59. Weertman J, Dislocation Based Fracture Mechanics; Word Scientific, 1996
60. Majumdar B S, Burns S J. Acta Metall 1981; 29: 570
61. Zhang T Y, Li J C M. Mater. Sci Eng 1991; A142: 35
62. Lakshmanan V, Li J C M. Mater Sci Eng A 1988; 104: 95
63. Zhang T Y, Tong T. J Appl Phys 1995; 78: 4873
64. Thomson R, J Mater. Sci. 1978; 13: 128
65. Li T L, Lee J H, Gao Y F, Pharr G M, Huang M and Tsui T Y. Appl Phys Lett 2009; 94: 171905
66. Liu G and Xu G. J Mech Phys Solids 2009; 57: 1078
67. Xu G and Argon A S. Mater Sci Eng 2001; A319: 144
68. Xu G, Argon A S and Ortiz M. Philos Mag A 1995; 72: 415
69. Xu G, Ortiz M. Int J Num Meth Eng 1993; 36: 3675
70. Xu G, Zhang C. J Mech Phys Solids 2003; 51: 1371
71. Zhu T, Li J, Samanta A, Leach A and Gall G. Phys Rev Lett 2008; 100: 025502
72. Zhu T, Li J and Yip S. Phys Rev Lett 2004; 93: 025503
73. Warner D H, Curtin W A and Qu S. Nat Mater 2007; 6: 876
74. Rice J R. J Mech Phys Solids 1992; 40: 239
75. Rice J R and Beltz G E. J Mech Phys Solids 1994; 42: 333
76. Vitek V. Philos Mag 1968;18:773
77. Xiang Y, Wei H, Ming P and E W. Acta Mater 2008; 56: 1447
78. Gao Y F. J Mech Phys Solids 2010; 58: 2023
79. Tadmor E B and Hai S. J Mech Phys Solids 2002; 51: 765
80. Li T L, Lee J H and Gao Y F. *in preparation*.
81. Hu S M. J Appl Phys 1991; 70: R53
82. Lee M L, Fitzgerald E A, Bulsara M T, Currie M T and Lochtefeld A. J Appl Phys 2005; 97: 011101
83. Murray C E, Saenger K L, Kalenci O, Polvino S M, Noyan I C, Lai B and Cai Z. J Appl Phys 2008; 104: 013530
84. Olson C R, Kuryliw E, Jones B E and Jones K S. J Vac Sci Technol B 2004; 24: 446 (2006)
85. Rudawski N G, Siebein K N and Jones K S. Appl Phys Lett 2006; 89: 082107

86. Shin Y G, Lee J Y, Park M H and Kang H K. J Cryst Growth 2001; 233: 673
87. Rudawski N G, Jones K S, and Gwilliam R. Appl Phys Lett 2007; 91: 172103
88. Rudawski N G, Jones K S, and R.G. Elliman. J Vac Sci Technol B 2008; 26: 435
89. Rudawski N G, Jones K S, and Gwilliam R. Mater Sci Eng R 2008; 61: 40
90. Rudawski N G, Jones K S, Morarka S, Law M E and Elliman R G. J Appl Phys 2009; 105: 053701
91. Lawn B. Fracture of Brittle Solids, 2nd ed., Cambridge University Press 1993
92. Rice J R and Thomson R. Phil Mag 1973; 29: 73
93. Gao Y F and Lou J. J Nanomaterials 2008; art no. 380961
94. Rice J R. J Mech Phys Solids 1992; 40: 239
95. Gao Y F and Bower A F. Modelling Simul Mater Sci Eng 2004; 12: 453
96. Xia S M, Gao Y F, Bower A F, Lev L C and Cheng Y T. Int J Solids Struc 2007; 44: 3685
97. Johanns K E, Lee J H, Gao Y F and Pharr G M. 2009; unpublished work
98. Wortman J J and Evans R A. J Appl Phys 1965; 36: 153
99. Ogata S, Li J, Hirosaki N, Shibutani Y and Yip S. Phys Rev B 2004; 70: 104104
100. Bao G and Suo Z. Appl Mech Rev 1992; 45: 355
101. Tschopp M A, Spearot D E and McDowell D L. Modelling Simul Mater Sci Eng 2007; 15: 693
102. Tschopp M A and McDowell D L. J Mech Phys Solids 2008; 56: 1806
103. Bei H and George E P. Acta Mater 2005; 53: 69
104. Shim S, Bei H, George E P and Pharr G M. Scripta Mater 2008; 59: 1095
105. Morris J R, Bei H, Pharr G M and George E P. *in preparation*.
106. Li T L, Morris J R, Bei H, George E P, Pharr G M and Gao Y F, *in preparation*.
107. Johnson K L. Contact Mechanics, Cambridge University, Cambridge, 1985
108. Estrin Y, Kim H S, Nabarro F R N. Acta Mater 2007; 55: 6401
109. Shim S, Bei H, George E P and Pharr G M, *unpublished work*
110. Rajulapatiay K V, Biener M M, Bienerb J and Hodge A M, Phil Mag Lett 2010; 90: 35

Vita

Tianlei Li was born on February 10, 1983 in Shenyang, Liaoning, China. He got his Bachelor's degree in 2005, majoring in Engineering Mechanics, from Shanghai Jiaotong University (SJTU), Shanghai, China. Then he continued his graduate study at Shanghai Jiaotong University for another two years, and got his Master's degree in 2007, majoring Solid Mechanics.

He enrolled in the doctoral program in the Department of Materials Science and Engineering at the University of Tennessee, Knoxville in 2007. The Doctor of Philosophy degree was received in December 2010.